Norwegian University of Life Sciences
Faculty of Environmental Science & Technology
Dept. of Mathematical Science & Technology

Master Thesis 2015
30 credits

Mobile Mapping System positioning in GNSS denied environments

Posisjonering med Mobile Mapping Systemer i områder uten GNSS dekning

Ingrid Johnsbråten

Norwegian University of Life Sciences

Faculty of Environmental Science and Technology

Department of Mathematical Sciences and Technology (IMT)

Mobile Mapping System positioning in GNSS denied environments

Author:
Ingrid Johnsbråten

Supervisors:
Narve Schipper Kjørsvik
Jon Glenn Gjevestad

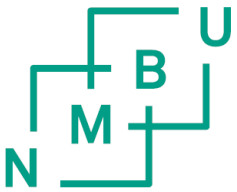

May 15, 2015

Abstract

The use of Mobile Mapping Systems (MMS) have increased over the last years, with integrated GNSS/INS solution as the common approach to preserving the quality of measurement. For environments where satellite signals become unavailable, such as in tunnels, additional sources of aiding need to be considered. Land-surveyed features, known as adjustment points, are typically utilized to preserve the requested accuracy in most projects. However, as this is a costly and less efficient procedure, alternatives to this approach would be preferred.

This thesis is concerned with the use of relative tie points (RTP), representing one such alternative to the position aiding. Two distinct tunnels have been object to research, in terms of the field work and data collection. The quality and errors in terms of the navigation solution have been treated in separate section. The research results is analysed and presented in three parts herein.

An additional higher grade IMU, lent out by The Norwegian Defence Research Establishment (FFI) for this purpose, has been added to the original mounting of positioning providing sensors. This enables the comparison of navigation solutions, based on performance. The available reference trajectory for the tunnels of research further provide comparison of true errors in the measurement.

The results show that the RTP aiding adds a useful constraint in the dataset resulting in a more consistent trajectory. Including an amount of 10–20 RTPs seem sufficient for the purpose of the position aiding, as shown in Part I. The speed throughout the tunnel is confirmed important in terms of the overall accuracy of position. Part II conclude that the original underlying model in TerraPos is inadequate in terms of external error effects. Part III further investigates the systematic behaviour uncovered in Part II, by means of the gravitational attraction of masses surrounding the surveying vehicle while inside a tunnel. Approximation to the largest resulting error in position and corresponding processing of the dataset return affirmative results. Neglecting the masses by free-air reduction results in a significant error that cannot be ignored.

Sammendrag

Bruk av Mobile Mapping Systems (MMS) har økt de siste årene, med integrert GNSS/INS løsning som den mest vanlige kombinasjonen for å bevare kvaliteten på navigasjonsløsningen. For miljøer der satellittsignaler plutselig blir utilgjengelige, som for eksempel i tunneler, er behovet for mer informasjon til systemet nødvendig, for å oppnå den ønskede nøyaktigheten. Landmålte punkter, kjent som *justerings*punkter, gir den mest nøyaktige referansen. Dette er en kostbar og mindre effektiv prosess, og alternativer vil være å foretrekke, forutsatt at den nødvendige nøyaktigheten kan oppnås.

Denne oppgaven fokuserer på bruken av relative *sammenbindings*punkter. To forskjellige tunneler har vært gjenstand for forskning i oppgaven. Resultatene presentert i tre deler.

En høyere grads IMU er blitt lånt ut av Forsvarets Forsknings Institutt (FFI) for denne oppgaven, som representerer en ellers utilgjengelig grad av nøyaktighet og presisjon, og muliggjør en videre sammenligning av resulterende navigasjonsløsninger. En tilgjengelig referanse for tunnelene returnerer sanne feil som mål på kvaliteten.

Resultatene viser at justeringspunkt tilfører datasettet informasjon som resulterer i en mer konsistent løsning. En mengde på 10–20 punkter kan være tilstrekkelig, som vist i Del I. Hastighet gjennom tunnelen blir bekreftet viktig for den totale nøyaktigheten. Del II konkludere med at den opprinnelige underliggende modellen er utilstrekkelig, da feil forårsaket av umodellerte utenforliggende effekter finnes i dataene. Del III undersøker videre den systematiske oppførsel avdekket i Del II. En analytisk tilnærming og en tilsvarende prossesert analyse gir samsvarende konklusjon av denne feilen. Neglisjering av omkringliggende masser ved å anta en fri-lufts reduksjon utgjør en betydelig feil når inne i tunnellen. Denne feilen kan ikke ignoreres.

Acknowledgement

I would like to express my sincere gratitude towards my dedicated supervisor, Narve Schipper Kjørsvik, at TerraTec AS. His support and guidance has been invaluable throughout this final process towards the completion of my grade. Without his unshaken patience and understanding, it is doubtful if I would have come this far, and I owe it all to his belief in my potential and in finishing my thesis.
A great thanks is also handed to my second supervisor, Jon Glenn Gjevestad.

Appreciations is extended to Leif Erik Blankenberg and to the people at TerraTec AS in general, for providing me with the data collections and the topic of research. Their available expertise and support have been of a great help to my research.

The Norwegian Defence Research Establishment (FFI) deserves additional thanks for the loan of the HG9900 IMU, for the purpose of this thesis.

Special thanks goes to my dear friends and family, for all their support and attempts to understand my priorities towards my thesis, and for their uncompromising love for me.
And to my parents especially, I owe to you both a great share of my success.

Contents

List of Figures

List of Tables

Chapter 1

Introduction

1.1 Background

Mobile Mapping Systems (MMS) have been object for research and development since the early 1990s. MMS surveying is one of the focus areas of TerraTec AS, as one out of the few companies[1] performing road and rail surveys with MMS among the countries in the Northern region.

The technology of satellite positioning by GNSS have truly revolutionised the field of surveying in terms of the Mobile Mapping systems (MMS) [Bossler and Toth, 1996].

Combining GNSS and INS in sensor integration are the most common approach in outdoor mapping applications, for the problem of signal loss or degradation in problem areas [Hofmann-Wellenhof and Wasle, 2008, p.467] such as urban canyons or in kinematic surveying in tunnels [Hofmann-Wellenhof and Wasle, 2008, p.467].

The concept is also known by the term *GPS-denied environments*.

In tunnels, land-surveyed adjustment points, is utilized to obtain the required accuracy in survey applications. This approach, combined with available GNSS observations outside of the tunnel, provides the most information and hence constitutes the best possible reference trajectory. The quality of the reference by utilizing adjustment points are at a few centimetre typically.

[1] According to their own website: *http //www.terratec.no/bilbaaren_laserskanning/cms/82* [Downloaded: 2015-05-11]

1.2 Historical backdrop

Navigation by inertial technology for surveying applications may be dated all the way back to the 1970s. The methods where originally developed with autonomous navigation in aviation and missile guidance in mind, and later in terms of a wider application to space and marine navigation [Torge and Müller, 2012, pp.212–213].

Classical survey techniques typically provide point-wise information only [El-Sheimy, 1996]. Today, applications generally require a higher sampling rate and greater efficiency by means of the data collection procedures. The method of direct georeferencing are one such example. Methods derived for kinematic-mode applications are characterized by faster and more economically efficient data collection [El-Sheimy, 1996]. The quality of kinematic systems in earlier years have been unsatisfying in terms of the higher accuracy demands by some applications.

The direct surveying method of MMS is preferred over the more classical surveying methods. The MMS is much more efficient than other activities,

Initially, classical static surveying methods was necessary to obtain the necessary accuracy. Development in the field of kinematic-mode acquisition methods have been significant, and are today just as competitive when it comes to the required quality of observation data at sub-decimetre and centimetre level. Combination of static GNSS base station observations by differential methods GNSS aiding of inertial navigation systems by differential techniques have hence been the dominating combination approach for a long time, especially for applications where direct georeferencing are preferred [Kjorsvik et al., 2010].

History of Vehicle Navigation Systems

According to [El-Sheimy, 1996], land vehicle navigation systems has advanced in the last years, mainly due to the advancement in navigation methods and computation technology. The different systems are usually classified by their design and application area. [El-Sheimy, 1996] provides several examples of land vehicle navigation systems, such as Automatic Vehicle Location and Navigation (AVLN), Intelligent Vehicle Highway Systems (IVHS), Intelligent Transportation Systems (ITS) and Mobile Mapping Systems (MMS). The last mentioned MMS represents the recent and most prominent development in this field, and in the recent years, the number, type and diversity of such systems has exploded. Some examples of developed MM systems follow in this section.

As stated, surveying using a moving van has become increasingly more sophisticated in the last couple of years. In 1983, development of a type of Mobile

Highway Inventory System (MHIS) started in Canada and in some US states, yet today there are several systems and designs in use for mobile mapping.
Compared to classical surveying methods, mobile mapping systems are far more efficient in terms of economical as well as time aspects. Due to the development of technology, mobile mapping are competitive in terms of accuracy requirements as well. [El-Sheimy, 1996] describes a *classical* approach, where discrete measurements are acquired separately and used in post-processing to "fix the position of the individual points". In a more *kinematic* approach, a combination of other sensor measurements will be utilized to minimize the number of tie points, or preferably make tie points totally redundant in some applications.

In 1988, satellite positioning methods, as for instance Differential GNSS (DGNSS), where being employed into the systems, which largely improved both the positioning accuracy. Inertial strap-down systems where also introduced, in combination with the GPS. Development in this field have roots, among others, in Canada.

Surveying and navigation

The modes of surveying and navigation are related [Hofmann-Wellenhof and Wasle, 2008, p.12], but different in terms of desired solutions. The circumstances in development today however, implies that the distinctions are increasingly being reduced.

The goal of surveying is mainly positioning. Navigation on the other hand, has traditionally been concerned about determination of position, velocity and attitude of moving objects [Hofmann-Wellenhof and Wasle, 2008].

Consequently, requirements for obtained accuracy have also differed. While the surveying in the past have been characterized by high positioning accuracies, navigation have required real-time or near real time processing of kinematic observations and hence the accuracy requirements have been lower. Surveying methods have in the past been reckoned as static or post-processing techniques. The former differences concerning accuracy requirements and final aim are, as [Hofmann-Wellenhof and Wasle, 2008] states, less distinct when considering classic definitions of the two modes, in terms of the techniques used today.

1.2.1 Examples of early Mobile Mapping Systems (MMS)

The following $GPSVan^{TM}$ and VISAT are early examples of mobile mapping vehicle systems, developed by the State Universities of Ohio and Calgary respectively.

The VISAT system The mobile mapper $VISAT^{TM}$ system developed at the Calgary University, in the early 1990s. VISAT is the abbreviation for Video Inertial and SATelite GPS. The system was among the first terrestrial MM systems. [El-Sheimy and Hassan, 2007]

The system consists of: a strapdown INS, dual-frequency receiver, 8 digital cameras providing RGB images, and a odometer attached to the speed sensor. The odometer output provide update for the INS when the solution is missing GNSS data due to e.g. a blockage of the signal.
The obtained mapping accuracy of the VIASAT system is about 0.1–0.3 m, for objects of range ∼50 m from the van to either side. Operational speed vary up to 30 m/s. [El-Sheimy and Hassan, 2007]

The VIASAT system utilize a dedicated software for viewing, analyzing, measuring and transferring of data, named "VISAT Station" [El-Sheimy and Hassan, 2007].

Figure 1.1: *The mobile mapper $VISAT^{TM}$ system developed at the Calgary University.*

The GPSVan system The $GPSVan^{TM}$ system is described in [Bossler and Toth, 1996]. It was developed in the 1990s at the Centre for Mapping at Ohio State University, for the main task of determining feature coordinates to sub-meter accuracy from a moving platform.

This was done by integrating a combined GPS and dead reckoning navigation solution with extracted imaging sensors measurements derived by photogrammetry techniques of stereo images. The system was designed for corridor mapping along transportation lines, e.g paved roads or rail-roads.

The system utilize integration of GPS, dead reckoning (DR) observations, and derived image feature tracking [Bossler and Toth, 1996]. [El-Sheimy, 1996, p.7] lists the following positioning and imaging sensor set-up for the $GPSVan^{TM}$:

GPS, DR, Gyros, CCD cameras and VHS video recording. The accuracy is further obtained at $\pm 1m$ in [x,y] and $\pm 2m$ in height.

Figure 1.2: *The Ohio state University third generation $GPSVan^{TM}$ on sight.*

1.3 System and software

1.3.1 Lynx Mobile Mapper vehicle

The surveying vehicle are custom built and owned by TerraTec AS[2].

The vehicle is a mobile mapping surveying system, designed for sampling of lidar and image data. The scanner system corresponds to the Lynx MG1 The system include two lidar scanners, mounted in different directions for an optimal coverage of point cloud matching and density. Each scanner have a 360 degrees visual field and sample rate of 200 kHz. Two adjustable cameras pointing backwards are mounted at the rear, sampling images for RGB colouring of the resulting point cloud. Additional cameras from ViaTech, together with a video recorder, are mounted on the inside of the front window. These videos and images are used for visualisation purposes in the final product of TerraView.

The external sensors on the vehicle's roof are mounted on a liftable platform, as shown in Figure 1.4. The elevated position are utilized to cover steeper roadsides.

The georeferenced solution are provided by the incorporated positioning system POS LV 420, utilizing the GNSS measurements, integrated IMU navigation states

[2]URL: *http //www.terratec.no/bilbaaren_laserskanning/cms/82* [Download 2015-05-02]

Figure 1.3: *TerraTec Lynx Mobile Mapper vehicle as seen in profile. URL: http //www.apiroter.com/products/optech/lynx_mg1.html [2015-05-02]*

Figure 1.4: *TerraTec Lynx Mobile Mapper exterior mounting of sensor instruments. The elevated ramp is about 4 m above ground. URL: http : //www.terratec.no/ [2015-05-02]*

Figure 1.5: *Optech Lynx MG1 Mobile Mapper.*

and odometer output. The positioning system optimizes the final solution by combining the individual advantages of GPS with those of inertial technology. An optimal trajectory are generated by post-processing in TerraPos when in office.

The Applanix POS LV 420 system[3] consists of the following positioning components:

- Inertial Measurement Unit (IMU)
- POS Computer System (PCS)
- Distance Measurement Indicator (DMI)
- 1 GPS Receiver
- 2 GPS Antennas

IMU specifications: LN200 and HG9900

The original mounting include the LN200 sensor, manufactured by Northrup Grumman. This is reckoned as a middle class performance IMU. The gyro and the accelerometer technology of the LN-200 equal fibre optics and MEMS respectively [Kjorsvik et al., 2010]. The LN200 inhabits a medium-accuracy performance.

[3]URL: http://www.applanix.com/products/land/pos-lv.html [download 2015-05-02]

Figure 1.6: *Applanix POS LV 420*

Figure 1.7: *Illustrations of the HG9900.*

Figure 1.8: *Illustrations of the LN200.*

The HG9900 IMU by Honeywell are lent out by the Norwegian Defence Research Establishment for comparison of measurement performance for the purpose of the research derived in Part II and III. Specifications for the sensors includes a Ring Laser Gyro (RLG) and no MEMS technology in terms of the accelerometer. The HG9900 are reckoned as a high-end sensor [Kjorsvik et al., 2010].

Further specifications in terms of performance will be provided later, in Part II.

MM applications of the Lynx system

Surveys utilizing the Lynx MMS are multi-purposed, and applied to both road, off-road, rail or marine projects.The sampling is performed at velocities ranging up to 20 m/s.

Tunnel surveying Problems in georeferencing of data arise for surveys inside tunnels, due to unavailability of integrated GNSS/INS positioning support. Satellite signals are blocked by the topographic masses, hence GNSS data are missing for the duration of time while the vehicle is inside the tunnel.

GNSS aided solutions re-occurs once the vehicle exits the tunnel on the other side. More advanced post-processing is used later to derive the accurate trajectory from the estimated navigation states

Resulting products for tunnel MM surveys are typically TIN[4]-models, drawing tunnel profiles or computing ceiling heights.

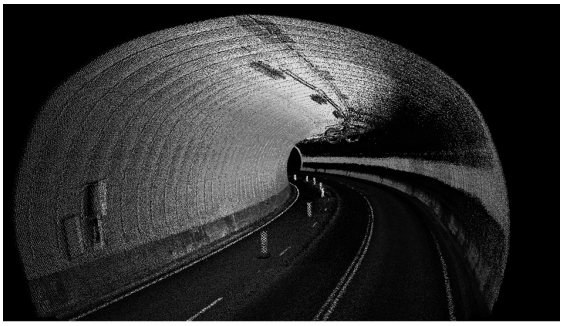

Figure 1.9: *Sampled lidar point-cloud data of tunnel environment by Lynx MMS.*

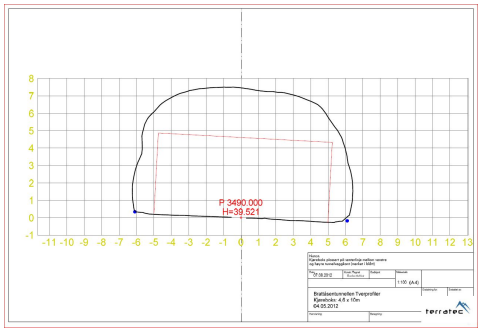

Figure 1.10: *Height and width of a tunnel's cross-section.*

[4]Triangular Irregular Networks. As used in geographic information systems.

1.3.2 TerraPos

TerraPos is used for the purpose of post-processing of datasets in this research. TerraPos is developed by TerraTec AS. More information can be located on the website[5], or in the accompanying manual and quick guide.

By utilizing precise point positioning (PPP) and tightly coupled (TC) for an integrated GNSS and inertial navigation solution, TerraPos represents the state-of-the-art in software technology for precision processing, both for kinematic platforms and in post-processing mode. Dual-antenna processing is enabled.

Solutions for loose coupling (LC) from existing GNSS trajectories, as well as other combinations, are also available.

TerraPos are available both for Windows and Linux, and can either be used with a GUI or be controlled from the command line. It is typically developed for kinematic applications, valid for projects both on land, in the air, or at sea.

1.4 Research Objectives

The aim and motivation of this research is to further investigate alternatives to land-surveyed adjustment points, as aiding of the navigation solution in GNSS denied environments. GNSS is the preferred external aid when outside, as long as satellite signals are available.

Other aiding alternatives are preferred if they turn out either more efficient, less time demanding in terms of surveying, and to a lower cost as opposed to adjustment points. At the same time, the aiding needs to ensure the required accuracy.

1.5 Thesis Outline

The thesis is structured into seven distinct chapters, as summarized below.

Introduction The introduction is provided in this chapter, shorter sections containing of notation and abbreviation follow.

[5]URL: *http : //www.terratec.no/filarkiv/File/TP2brochureoct2013.pdf* [Downloaded 2015-05-02]

Theory The consecutive two chapters derives the basic theoretic framework and overview of GNSS and INS, and the linear dynamics of navigation and Kalman Filtering.

Three sequential chapters follow, involving all the research conducted, further field work descriptions and accompanying analyses. Additional theory specifically related to the respective parts of research is provided at the beginning of each chapter.
The research chapters naturally follow the subdivision given as Part I, II and III.

Part I concern the use of relative tie point (RTP) measurements. RTP can be utilized as external aiding for generating the accurate position solution while being without GNSS observations inside a tunnel.
The dataset provided for analysis is the Lapplia tunnel.

Part II will consider a second tunnel, comprising the Innfjorden dataset. An additional set of gyros and accelerometers are mounted on the MM vehicle, providing a total of two sampled datasets.
The research will focus on the navigation solution being related to the performance of the inertial navigation sensors of higher and lower grade.

Part III provide a further treatment of the Innfjorden dataset. This part seek to distinguish and model significant errors in the data. Due to the properties of increased precision and accuracy of the higher grade IMU, it will be utilized to detect unmodeled external error sources affecting the data, an further investigate what effect the possible errors will have on the position state estimate.

Summary and outlook , provided eventually, will gather the results from the three parts of research and conclude on their relations. This chapter winds up the underlying object of research in terms of Part I–III.

Chapter 2

Systems Overview

2.1 Global Navigation Satellite Systems (GNSS)

GNSS is normally used for Global Navigation Satellite Systems, implying there are more than one system [Hofmann-Wellenhof and Wasle, 2008]. Four such systems are GPS, GLONASS, BEIDOU and GALILEO.

The Global Positioning System (GPS) is operated by the United States, GLONASS by the Russian Federation, BEIDOU by the Chinese government, and GALILEO being a project of the European Union and European Space Agency (ESA) [Seeber, 2003]. BEIDOU and GALILEO are still developing and expanding their constellation, and not fully operative as of now. Only observations by GPS and GLONASS are hence utilized by general GNSS receivers today.

GPS and GLONASS will be reviewed in more depth, with greatest emphasis on the GPS.

Much of the material outlined for GPS in the following section are valid for the other GNSS systems also [Seeber, 2003]. They vary in constellation design, e.g. the total number of satellites, the defined orbits, and their coverage of the Earth. The fundamentals of satellite positioning are more or less equal.

2.1.1 Global Positioning System (GPS)

GPS is short for Global Positioning System, a satellite-based radio navigation system. The development of GPS was started in 1973, by the US military. The

system reached full constellation of 24 satellites in 1995. [Seeber, 2003, Ch.7] Three-dimensional time-tagged position and navigation data provided by the system satellites are today available for anyone with a GPS receiver.

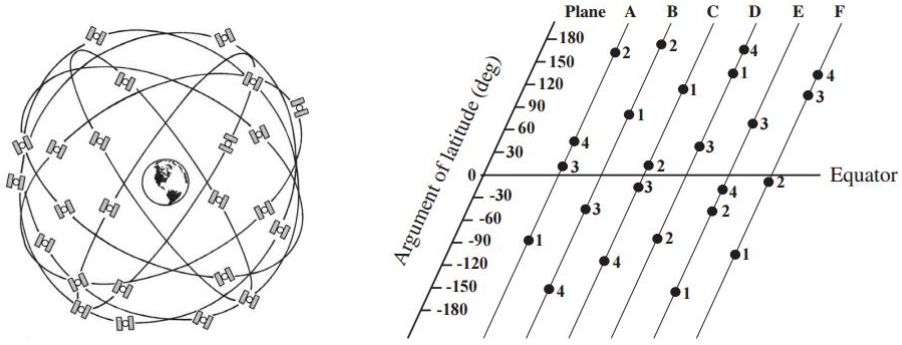

Figure 2.1: *GPS orbits (right) and baseline configuration (left).[Seeber, 2003, Fig.7.4]*

GPS fundamentals

The GPS system is divided into the following three segments:

1. Space segment
2. Control segment
3. User segment

The space segment involves the constellation of 24 active GPS satellites.

The control segment corresponds to a network of ground stations on Earth, continuously keeping control over the GPS system and time, including the respective orbit predictions and corrections.

All the GPS receivers and its users on Earth together constitute the user segment.

GPS measurements

GPS is a one-way system, as it was originally developed with military applications in mind only. The military way of thinking entails not revealing any information of the receiver location. Hence the signal transfers only from the satellite in space and to the receiver at some point on Earth.

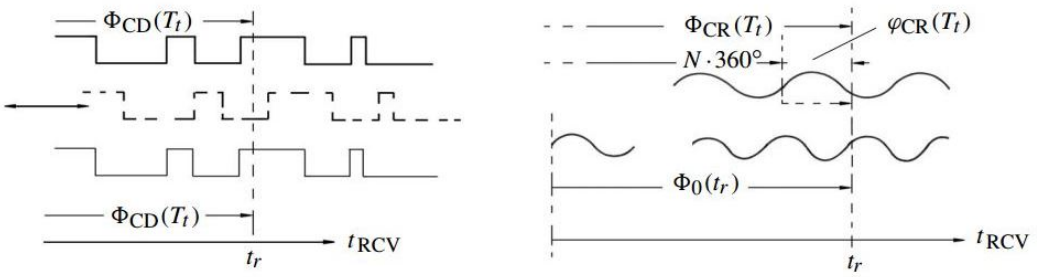

Figure 2.2: *Illustration of signal code (left) and carrier phase measurements (right). [Seeber, 2003, Fig.7.33 and 7.34]*

The coordinates of the satellite are considered known, determined by derived orbit parameters relative to a global reference frame. By measurements from three GPS satellites, the exact location of the user antenna is calculated.

The GPS observations equal range measurements, corresponding to the distance measured between satellite and user antenna. Further calculations are based on the relations between distance, velocity and time. The ranges are observed when combining the knowledge of the speed of light and measuring the time difference representing the signals time of travel between the satellite clock and the receiver clock.

To detect a time difference, the time must be clocked. Since the system is one-way it follows that two clocks must be involved. A problem arise once the clocks providing the time tags are not the same, and not of equal quality. Though corrected and calibrated, the two clocks will never be perfectly synchronized with each other. Hence the clock offset is an unknown parameter to be estimated alongside with the other unknown states. By introducing the clock offset estimate in the state vector, an additional observation from a fourth satellite is necessary to satisfy the degrees of freedom.

Due to this time offset, the GPS observations are regarded as *pseudoranges*.

The pseudorange-observations can be derived in two ways, either by reading information from the coded signal directly or by direct measures of the phase of the carrier. [Hofmann-Wellenhof and Wasle, 2008, p.221]

1. Code (C/A and P code)

2. Carrier phase (L1 and L2 frequencies)

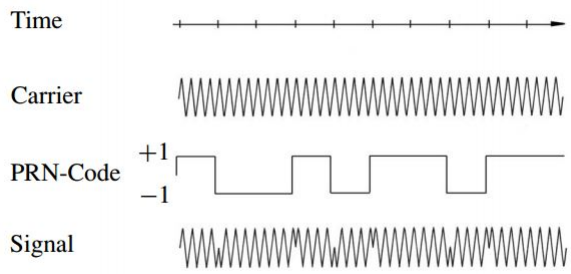

Figure 2.3: *The GPS signal structure and further relation to GPS time tagging, carrier phase and code respectively. [Seeber, 2003, Fig.7.10]*

1. Code measurements

Code pseudorange measurements $R_r^s(t)$ are derived in [Hofmann-Wellenhof and Wasle, 2008, p.161] for epoch t

$$R_r^s(t) \;=\; \rho_r^s(t) + c\Delta\delta_r^s(t) \tag{2.1}$$

for the receiver r and satellite s.
$\delta_r^s(t)$ are the geometric distance and c representing the speed of light.

The last term $\Delta\delta_r^s(t)$ can be separated in terms of the clock bias, such that the known observations and unknown quantities may be divided in terms of the left and right side of the equation respectively. This results in Equation 2.2.

$$\begin{aligned}
\rho_r^s(t) &= \sqrt{(X^s(t) - X_r)^2 + (Y^s(t) - Y_r)^2 + (Z^s(t) - Z_r)^2} \\
\delta_r^s(t) &= a_0 + a_1(t - t_c) + a_2(t - t_c)^2 + \rho^{rel} \\
\Delta\delta_r^s(t) &= \delta_r(t) - \delta^s(t)
\end{aligned}$$

$$R_r^s(t) \;+\; c\delta^s(t) \;=\; \rho_r^s(t) \;+\; c\delta_r(t) \tag{2.2}$$

2. Carrier phase measurements

The mathematical model for carrier phase measurements is

$$\Phi_r^s(t) \;=\; \frac{1}{\lambda^s}\rho_r^s(t) + N_r^s + \frac{c}{\lambda^s}\Delta\delta_r^s(t) \tag{2.3}$$

$$\Phi_r^s(t) + f^s\delta^s(t) \;=\; \frac{1}{\lambda^s}\rho_r^s(t) + N_r^s + f^s\delta_r(t) \tag{2.4}$$

for $\Phi_r^s(t)$ expressed in number of cycles. λ^s is wavelength, $\rho_r^s(t)$ the geometrical distance and N is the integer ambiguity. $\Delta\delta_r^s(t)$ is still the combined receiver and satellite clock bias.
A similar shifting of equation terms is performed, by means of substitution by satellite carrier frequency $f^s = c/\lambda^s$, resulting in Equation 2.4.
For more, please be referred to [Hofmann-Wellenhof and Wasle, 2008, Ch.6].

Code range and carrier phase accuracy Code range measured position provide meter level in terms of obtained accuracy. Correspondingly, positions provided by carrier phase observations have an accuracy at the millimetre level at best.
The accuracy of the code range positioning may however be enhanced by smoothing techniques or improved receiver technology.

Doppler shift A raw Doppler shift is important in navigation application, which allow for velocity determination. For the range rate, the equation for the Doppler shift is given in [Hofmann-Wellenhof and Wasle, 2008, p.108] as

$$D = \lambda\dot{\Phi} = \dot{\rho} + c\Delta\delta. \tag{2.5}$$

The achievable accuracy is about 0.001 Hz. [Hofmann-Wellenhof and Wasle, 2008, 108-109]

Error sources of GPS

Satellite signals of GPS are weak and objects to several sources of errors during the travel between the satellite in space and the receiver at Earth's surface. A selection of error sources for the observation is listed below.

- Ionosphere and troposphere disturbance
- Multipath
- Ambiguity resolution
- Antenna phase centre

Multipath is a critical source of error in terms of attitude determination in INS applications. The multipath effect for GPS signals is illustrated in Figure 2.4.

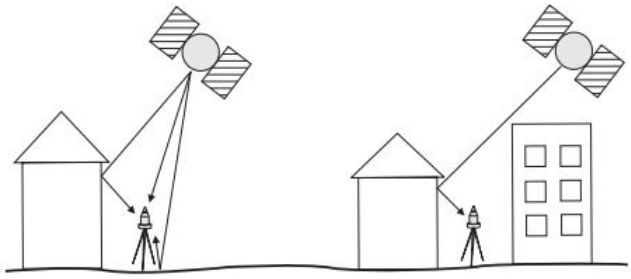

Figure 2.4: *Illustration of multipath error. [Seeber, 2003, Fig.7.53]*

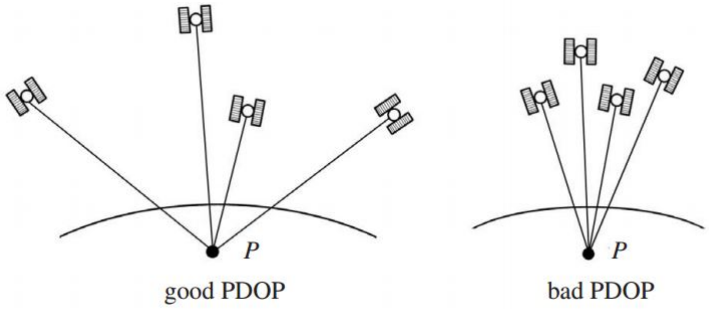

Figure 2.5: *Illustration PDOP geometry. [Seeber, 2003, Fig.7.49]*

GPS augmentation systems

Established in some regions are separate augmentation systems meant to accompany the satellite systems, such as the GPS. Examples of augmentation systems are EGNOS (European Geostationary Navigation Overlay System) in Europe or WAAS (Wide Area Augmentation System) in the US [Seeber, 2003, p.392-393]

Augmentation systems can contribute to higher accuracy in many applications.

2.1.2 Methods in GPS

Principle of GNSS satellite positioning A GPS navigation computer, such as in a vehicle, constantly computes vectors between the GPS satellites and the vehicle. The GPS receiver needs four or more satellites to provide a three-dimensional position, relative to the global reference coordinate system. Each satellite sends out a signal containing information about its identification, orbit parameters, and

time tag for the signal. Identification are for instance a unique PRN number per satellite in terms of GPS. Ground stations on Earth provide corrections for the orbits and the satellite clock.

For code observations, the GPS antenna receive the signal and algorithms further compare the time tag provided by the satellite clock with the time tag from the GPS receiver clock. The time difference is converted into a range measurement between the satellite and receiver's position by multiplying with the speed of light. By using the ranges to a minimum of four satellites, the three coordinates for the receiver and its clock error can be calculated.

The positioning method referred to are known as *trilateration*. The satellites' positions are known. The location of an unknown point can therefore be calculated by the length and direction from points of known locations and to the unknown point. The ranges to the known satellite positions all intersect in the unknown point, and a system of equations unfolds.

Two important GNSS methods used for accurate positioning: DGNSS and PPP, are emphasised below.
Both methods are of relevance to the GNSS/INS integration in terms of navigation.

Precise Point Positioning (PPP)

Precise Point Positioning use a model that utilize accurate orbital and satellite clock data, in addition to dual-frequency code range or carrier phase observations [Hofmann-Wellenhof and Wasle, 2008, p.166].
The unknowns in the combinations [Hofmann-Wellenhof and Wasle, 2008, p.167] are the ρ_{trop} point positioning, receiver clock error $\Delta\delta$, tropospheric delay Δ^{trop}, and the phase ambiguities.
The unknowns can be solved by use of e.g. a sequential least-square adjustment, or an extended Kalman filter [Hofmann-Wellenhof and Wasle, 2008, p.167].

The equations for code pseudorange and carrier phase by ionosphere-free combinations are given in Equations 2.6 and 2.7 respectively

$$\frac{R_1 f_1^2}{f_1^2 - f_2^2} - \frac{R_2 f_2^2}{f_1^2 - f_2^2} = \rho + c\Delta\delta + \Delta^{Trop} \tag{2.6}$$

$$\frac{\lambda_1 \Phi_1 f_1^2}{f_1^2 - f_2^2} - \frac{\lambda_2 \Phi_2 f_2^2}{f_1^2 - f_2^2} = \rho + c\Delta\delta + \Delta^{Trop} + \frac{\lambda_1 N_1 f_1^2}{f_1^2 - f_2^2} - \frac{\lambda_2 N_2 f_2^2}{f_1^2 - f_2^2} \tag{2.7}$$

PPP may be used in both static and kinematic mode. [Hofmann-Wellenhof and

Wasle, 2008, Ch.6.1.4] for more.
Centimetre level accuracy are possible in both static and kinematic applications, are argued in [Hofmann-Wellenhof and Wasle, 2008, p.168].

DGNSS

Differential GNSS utilize two or more receivers. The basic principal of DGNSS is illustrated in Figure 2.6.

As shown, a reference stations provides corrections, which again are transmitted to the remote receiver [Hofmann-Wellenhof and Wasle, 2008, p.169]. The receiver apply the corrections to the measurements of code range.
Corrected pseudoranges will further improve the accuracy with reference to the basestation.

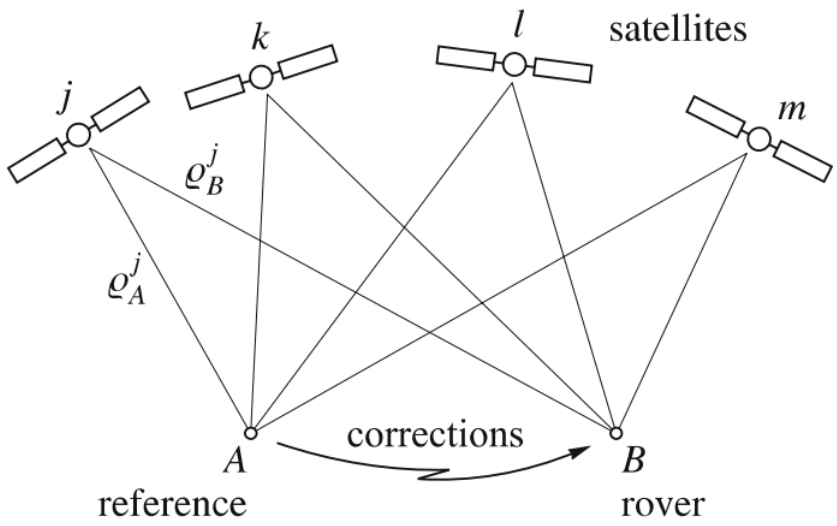

Figure 2.6: *Basic concept of differential positioning with GPS [Hofmann-Wellenhof and Wasle, 2008, Fig.6.1]*

[Hofmann-Wellenhof and Wasle, 2008, p.172] emphasize that DGNSS with phase ranges are used in the most precise kinematic equations.

The observation equations for DGNSS for code ranges and phase ranges respectively, are given in [Hofmann-Wellenhof and Wasle, 2008, pp.170-172]

2.1.3 Overview of GLONASS

GLONASS[1] is the Russian equivalent version of the GPS. The design is quite similar to GPS. GLONASS is a military system developed, in the 1970s, and additionally offered for civil use [Seeber, 2003, Ch.7].

Parameter	GLONASS	GPS
Number of satellites (spares)	21 (3)	21 (3)
Number of orbital planes	3	6
Inclination	64.8°	55.0°
Orbital altitude	19 100 km	20 180 km
Orbital period(sidereal time)	11 h 15 min	12 h
Repeated ground tracks	every sidereal day	every 8 sidereal day
Ephemerides	9 parameter $\ddot{r}$, $\dot{r}$, r (in ECEF system)	Kepler elements and interpolation coefficients
Geodetic datum	PZ-90	WGS 84
Satellite signal	Frequency division	Code division
L1 frequency band	1.602-1.615 MHz	1.575 MHz
L2 frequency band	1.246-1.256 MHz	1.228 MHz
C/A-code frequency	0.511 MHz	1.023 MHz
P-code frequency	5.11 MHz	10.23 MHz

Table 2.1: *GPS and GLONASS comparison. [Seeber, 2003, Table 7.26 (extract)]*

Comparison of GPS and GLONASS Table 2.1 summarizes fundamental GNSS parameters for GLONASS and GPS respectively.

Though the GPS and GLONASS systems have similarities [Seeber, 2003, Ch.7], there are some differences. While signals from GPS satellites are distinguished by a unique PRN-code, all GLONASS satellites use an equal code. Instead, GLONASS satellites utilize different frequencies for the transfer of carrier signals. This approach is known as FDMA (Frequency Division Multiple Access).

The GPS system use CDMA (Code Division Multiple Access). Consequently, the signal handling for the two systems will be different [Seeber, 2003, p.385].

Combination of GPS and GLONASS The main advantage of combining satellite observations from the two systems is due to the number of satellites available. The ranges of frequency bands of L1 and L2, as seen in Table 2.1, are not

[1]GLObal NAvigation Satellite System

very different for the two systems. This further allow the development of combined GLONASS and GPS receivers, since they can both make use of the same antenna.

Since the code frequency values being nearly half of GPS values, GLONASS signals have a slightly lower range resolution than GPS. A clock offset must also be accounted for when combining both GPS and GLONASS observations, due to the different time systems as given in Table 2.1.

For the combined solution, a coordinate transformation between the geodetic datums is also needed. Details are found in [Seeber, 2003].

2.2 Inertial Navigation Systems (INS)

An Inertial Navigation System (INS) includes an Inertial Measurement Unit (IMU), a platform for the mounting and stabilizing mechanization, together with a computation unit for deriving the sensed navigation states. [Jekeli, 2001, p.101]

Inertial Measurement Unit (IMU) A typical IMU consists of an accelerometer and a gyro sensor in combination. Both sensors have three aligned, orthogonal axes. Outputs are measured in the sensor frame (s-frame).
The following notation and definitions presented in this chapter are consistent with [Kjørsvik, 2010].

The accelerometer measure the specific force $\tilde{f}^s$, while the accelerometer outputs are velocity increments $\Delta\tilde{v}^s$. The superscript s denotes the sensor frame. The output equals the integrated specific force measurement for the IMU data interval δt. As measurement are inevitably affected by errors δf^s, the velocity increment output equals

$$\Delta\tilde{v}^s \;=\; \int_{\delta t} \tilde{f}^s(t)\; dt = \int_{\delta t} f^s(t) \;+\; \delta f^s(t) dt \tag{2.8}$$

All the variables are time-dependent. The IMU data rate is typically 100 – 400 Hz.

The measurements of the gyro are angular rates $\tilde{\omega}^s_{is}$, measured in the sensor frame relative to the inertial frame. When integrated over an IMU sampling interval δt the output returns the angular increments

$$\Delta\tilde{\theta}^s \;=\; \int_{\delta t} \tilde{\omega}^s_{is}(t)\; dt = \int_{\delta t} \omega^s_{is}(t) \;+\; \delta\omega^s_{is}(t) dt, \tag{2.9}$$

where $\delta\omega^s_{is}$ corresponds to the gyro error in the sensor frame relative to the inertial frame.

2.2.1 Development of INS

The development of INS are outlined among others in [Jekeli, 2001, p.101]. Inertial navigation systems was originally invented for ship navigation, and later for land applications. The earliest development are dated to before and after World War II in the twentieth century.

Aircraft navigation applications followed in parallel to the increase in vehicle speed. In the 60s and 70s it spread to other industries, such as missile guidance, space navigation and lunar missions.

Today, satellite positioning systems (GNSS) have overtaken much of INS previous role as a main positioning system in many applications.

2.2.2 Mechanization equations in Inertial Navigation

The actual mounting of sensor instruments on the vehicle and their relative connection to the respective reference frames, are the *mechanization* of the navigation system [Jekeli, 2001, 104]. The mechanization design will have an effect in the error propagation in the sensors.

Strapdown INS For a strapdown system, all instruments of the IMU are contained in an isolated box, physically attached to a platform mounted on the vehicle [Jekeli, 2001, p.105]. The sensors will therefore follow the range of dynamics caused by the vehicle's movements.

Lab calibration partly compensates for the errors induced by the dynamics. Strapdown systems are usually smaller in size and weight, as opposed to stabilized platforms, and available at a lower cost. Stabilized platforms initially have a higher accuracy, though development in technology makes strapdown systems competitive. [Jekeli, 2001, pp.105-106]

The mechanization equations are derived in [Jekeli, 2001, pp.112-123].

2.2.3 Error Propagation

Error propagation in inertial positioning is of great importance, and represents the weakness of such systems [Torge and Müller, 2012, p.213]. For indirect measurements, the quantities desired are determined by their mathematical relations

to the direct measurements. The indirectly derived observations causes the errors present in the original direct observations to be distributed into the indirect values. This is the termed error propagation [Ghilani, 2010, p.2].

The time stability of the bias and the scale factor of the gyro an the accelerometer measurements, are the two major sources of INS error characterization. Due to the nature of integration, the errors increase rapidly. [Torge and Müller, 2012, p.213].

2.2.4 Principals of Inertial Navigation

An INS is based upon principles derived from Newton's second law of motion in addition to effects due to gravitational forces [Torge and Müller, 2012, p.212].

Specific force

Unless otherwise stated, the theory below is found in [Torge and Müller, 2012, p.191].
The acceleration caused by one or more applied forces, causing an object to move or a change in its initial velocity, is defined as the *specific force*. More explicitly, force per unit mass. The specific force is most often denoted with the letter f^i.

According to the law of motion by Newton, the kinematic acceleration $\ddot{x}^i$ of a body in an inertial system is defined, when realized in the i-frame, as

$$\ddot{x}^i = f^i + g^i_{att} \ , \tag{2.10}$$

and rewritten in terms of specific force as

$$f^i = \ddot{x}^i - g^i_{att} \tag{2.11}$$

The letter g denotes the gravitational vector, due to the mass attraction only. It follows from the relations in Equation 2.11, that an accelerometer at rest will measure the gravitational acceleration g^i_{att} alone. Due to this fact the kinematic acceleration $\ddot{x}^i$ will be zero and the specific force f^i will equal g^i_{att}, defined in the opposite direction.

$$f^i = \ddot{x}^i - g^i_{att} = 0 \ - \ g^i_{att} \qquad \rightarrow \qquad f^i = -g^i_{att} \quad when\, \ddot{x}^i = 0. \tag{2.12}$$

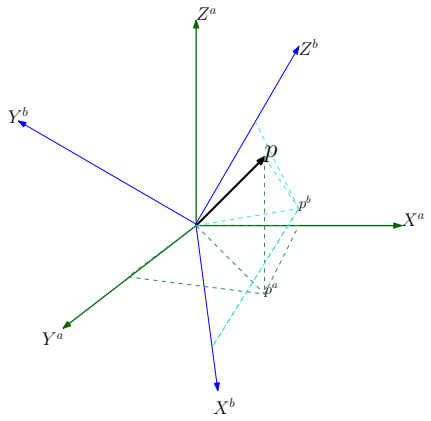

Figure 2.7: *Transformation of coordinates of a point p relative to the a and b reference frames.*

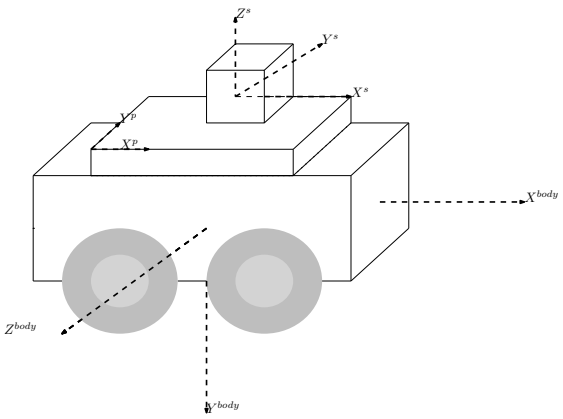

Figure 2.8: *Relation between the body, platform and sensor (IMU) frames-of-reference.*

2.2.5 Reference Frames in Inertial Navigation

Navigation systems require transformations between several reference frames. Each sensor provides measurements w.r.t some reference frame [Farrell, 2008, pp.27-28]. The sensor-defined reference frame need to be rotated into the navigation frame to relate to the system state. Hence measurements are only comparable if referred to equal reference frames.

More about reference frames are found in [Farrell, 2008, pp.19-22].

The relations between the body, platform and sensor frames-of-reference are provided in Figure 2.8. A transformation between two frames a and b is depicted in Figure 2.7. Further descriptions of the various frames of consideration are given below.

Inertial frame (i-frame) The inertial sensors measure quantities relative to the inertial frame. An inertial frame is not accelerated, hence Newton's laws of motion apply.
An Earth Centred Inertial (ECI) frame is defined with an origin coinciding with the Earth's centre of mass. The axes of the i-frame are fixed in a celestial system. The ECI-system's rotation about the Sun is negligible.

Further definitions are given in [Farrell, 2008, p.23] and [Terrapos-manual, 2015, p.23].

Earth frame (e-frame) Corresponds to the ECEF coordinate frame. The origin is in the centre of Earth's mass. Axes are pointing through the north pole(z-axis), x-axis through the reference meridian at Greenwich, and y orthogonal to the xz-plane. The system is right-handed, with its main rotation positively defined about the z-axis. [Terrapos-manual, 2015, p.23]
Defined parameters for both the ellipsoid and geoid model needs to be consistent for the choice of e-frame reference. Due to the Earth's rotational spin about its own axis, the e-frame is not an inertial system. [Farrell, 2008, p.24]

Local Level Geodetic frame (g-frame) The g-frame, or navigation frame, follows the location of the user referred to the ellipsoid. The downward pointing axis follows the ellipsoid normal. [Terrapos-manual, 2015, p.23]
The axes constitute a NED-system.

Mapping frame (m-frame) The m-frame is nearly similar to the g-frame. The primary and a secondary axes refers to the applied map projection. The third axis follow the ellipsoid normal, positive upwards. [Terrapos-manual, 2015, p.23]

Sensor frame (s-frame) The sensor's sensitive axes, such as for an IMU, constitute the right-handed sensor frame reference. [Terrapos-manual, 2015, p.23]

Platform frame (p-frame) For strapdown systems, the platform frame containing the IMU and other on-board instruments is rigidly attached to the vehicle. [Terrapos-manual, 2015, p.23]
This frame is used to align the sensor outputs to the nominal motion, with the X-axis directed forward, Y at starboard and Z downwards.

Body frame (b-frame) The p-frame is further referred to the body frame of the vehicle. A rotation define the relations between the two. [Terrapos-manual, 2015, p.23] The needed rotation compensated for the offset or relative rotation of the p-frame axes and the b-frame axes respectively [Farrell, 2008, p.27]
The body frame is used to relate all the instruments together with the navigation sensors. If all sensors of interest are in the sensors frame, the s-frame and b-frame are considered equal [Kjørsvik, 2010]. To clarify the purpose of the body frame, the example of aircraft can be considered. The aircraft represents the body, and to it a gyro-stabilized camera containing an IMU is attached. Hence the IMU rotate relative to its own sensor axis, since not rigidly attached to the body of the

plane (strapdown). A GNSS receiver is also mounted on the aircraft. To relate the IMU orientation of the camera images to the GNSS observations, the body of the aircraft become the common reference frame.

Output frame (o-frame) The output frame is related to the platform by a rotation in two steps: cardinal and (boresight-)calibrated rotation.
[Terrapos-manual, 2015, p.23]
E.g. the image coordinate system for a camera is an example of a output frame.

2.2.6 Transformation and rotation of reference frames

Position x^e, velocity $\dot{x}^e$ and attitude DCM C_s^erepresents the three basic navigation states. The superscript e here denotes e-frame realisation. The attitude is defined as the orientation of a reference frame attached to a specific body [Hofmann-Wellenhof and Wasle, 2008, Ch.1], w.r.t. some external reference frame.

Euler angles

The attitude parameters in navigation applications [Terrapos-manual, 2015, p.25] are Euler angles *roll, pitch* and *heading*. Roll ϕ is the rotation about the x-axis (direction forward), pitch θ rotate about the starboard axis and heading α rotate about the third vertical downward-facing axis z. [Farrell, 2008, p.46]

For a strapdown system, the computation of attitude is crucial [Titterton and Weston, 2004], and needs to be defined in the correct frame-of-reference. A Direction Cosine Matrix (DCM) is among the most commonly used in terms of orientation between reference frames.

Direction Cosine Matrix (DCM)

The problem at hand is how to compute the features referred to one coordinate frame, with respect to another frame of reference [Farrell, 2008, p.36]. This requires the operations of *translation* and *rotation* of points. A derived framework of Direction Cosines are provided in [Jekeli, 2001, pp.10-13].

As given in Farrell (2008), a DCM is unique and known if the relative orientation of two frames-of-reference is known. The reference frame's axes are assumed

orthogonal and right-handed positive.

In Equation 2.13 the DCM is decomposed into three rotations. Each rotation refers to one of the reference frame's axes. The sequence of these rotations is not arbitrary, and is depending on the order of rotation and on whether the axes are static or rotating. More about rotation sequences is given in [Terrapos-manual, 2015, p.25].

$$C_a^b = R_1(\alpha_1)R_2(\alpha_2)R_3(\alpha_3) \tag{2.13}$$

$$C_b^a = [C_a^b]^{-1} \tag{2.14}$$

The derivative of a DCM, as provided in [Farrell, 2008, p.51]. For coordinate systems rotating relative to each other, the derivative need to be calculated. A rotation between frame a and b is given by definition as

$$\dot{C}_a^b(t) = \lim_{\delta t \to \infty} \frac{C_a^b(t - \delta t) - C_a^b(t)}{\delta t} \tag{2.15}$$

The resulting expression for the derivative equal

$$\dot{C}_a^b = C_a^b \Omega_{ba}^a \tag{2.16}$$

for $\Omega_{ba}^a \equiv [\omega_{ab}^b \times]$.

See [Farrell, 2008, Sect.2.6] for more.

Quaternions

Alternatively to DCM is the *quaternion* approach. Quaternions are an effective and numerical stable representation of a 3-dimensional rotation, and preferable in terms of attitude integration [Kjørsvik, 2010].
More on quaternions can be found in the references, among others [Kjørsvik, 2010] or [Jekeli, 2001, pp.13-18].

In terms of the INS, the gyroscopes continuously provide the orientation of the accelerometers [Torge and Müller, 2012, p.212]. When rigidly attached to the vehicle, the gyro measures angular rates in the sensor frame w.r.t. the inertial frame.
When realized in the Earth frame, e-frame, the measured gyro angular increments $\Delta\tilde{\theta}^s$, provide the sensor orientation by the DCM C_s^e. The C_s^e is necessary to transform the measured accelerometer velocity increments $\Delta\tilde{v}^s$, from the sensor frame to the earth frame.
A time update of the system states is computed by numerical integration of the gyro and accelerometer data.

Chapter 3

Linear Dynamic Systems and State Estimation

3.1 Linear Dynamic Systems

The following relations are equivalent with the equations found in [Jekeli, 2001, pp.221-222].

The linear first order differential equation describe the change of the state-space system as a linear function of the random variable x(t) and the variable u(t), as

$$\dot{x}(t) = F(t)x(t) + G(t)u(t) \tag{3.1}$$

F(t) and G(t) are known matrices containing the necessary linearised relationship between the prior and current state of x per time t. The variable u(t) are assumed having normally distributed properties of zero mean and covariance described as Gaussian white noise. The solution to Equation 3.1 is given as

$$x(t) = \Phi(t, t_0)x(t_0) \; + \; \int_{t_0}^{t} \Phi(t, t')G(t')u(t')dt' \; . \tag{3.2}$$

$\Phi(t, t_0)$ is known as the state *transition* matrix, which transfers the state $x(t)$ from the initial time t_0 to the current epoch t.

For integration over a very short time interval $\delta t \; = \; t' \; - \; t$ the system dynamics matrix F, in Equation 3.1, can be assumed constant over the entire interval δt, the transition matrix for the that time interval is given as

$$\Phi(t, \; t') \; = \; e^{F(t \; - \; t')} \tag{3.3}$$

A Taylor series expansion results in the following linearised expression, as given in Equation 3.3

$$\Phi(t,\ t') \ = \ I + F(t\ -\ t') + \frac{1}{2!}(F(t\ -\ t'))^2 + \frac{1}{3!}(F(t\ -\ t'))^3 + \ldots$$
$$\ldots \ + \ \frac{1}{n!}(F(t\ -\ t'))^n,\ for\ n = 0, 1, 2,\ \ldots \qquad (3.4)$$

Equivalently, a sampled version of Equation 3.2, at discrete time t_k, is

$$x_k = \Phi(t_k,\ t_{k-1)})x_{(k-1)} \ + \ \omega_k \ , \qquad (3.5)$$

with

$$\omega_k = \int_{t_{k-1}}^{t_k} \Phi(t,\ t')G(t')u(t')dt'. \qquad (3.6)$$

The covariance matrix of ω_k is

$$Q_k = \int_{t_{k-1}}^{t_k} \Phi(t,\ \eta)G(\eta)WG^T(\eta)\Phi^T(t,\ \eta)d\eta. \qquad (3.7)$$

For practical use, the following numerical integrated of the process noise Q_k can be

$$Q_k \approx GWG^T\delta t + (FGWG^T + GWG^TF^T)\frac{(\delta t)^2}{2} \qquad (3.8)$$
$$+ (F^2GWG^T + 2FGWG^TF^T + GWG^T(F^T)^2)\frac{(\delta t)^3}{6} + \ldots$$

For the error covariance of the time propagated state x_k is

$$P_k \equiv E\{x_k x_k^T\} \qquad (3.9)$$
$$P_k = \Phi(t_k,\ t_{k-1})P_{k-1}\Phi^T(t_k,\ t_{k-1}) \ + \ Q_k \qquad (3.10)$$

For numerical evaluation of Φ, the time interval $(t_k\ -\ t_0)$ can be subdivided in terms of the transitive properties of the state transition matrix. This subdivision supports the assumption of a constant design matrix F. The property of Φ is written

$$\Phi(t_k,\ t_0) \ = \ \Phi(t_k,\ t_{k-1})\Phi(t_{k-1}, t_{k-2}) \ \ldots \ \Phi(t_1,\ t_0) \qquad (3.11)$$

A subdivision strategy may also be used for a numerical approximation of the process noise covariance Q, which in turn results in a sum of integrals. The matrices F and G are both assumed constant for integrals i over small subdivided intervals $\delta t = t_k - t_{k-1}$. The resulting approximation is equal to the summation of computations of Q_k by Equation 3.7.

See [Farrell, 2008, pp.140-144] for more of Φ and Q_k.

3.1.1 Stochastic modeling and random variables

Uncertainties arise from noise and imperfections in the sensors [Farrell, 2008, p.105]. A navigation system utilizes the uncertain information in the estimation of the navigation system's.

The degree of certainty is either related to the process being observed or the measurements from it. Probability theory and stochastic processes enables quantitative analyses of a system. [Farrell, 2008, p.106]

Autocorrelation and Power Spectral Densities

Farrell (2008) describes how a stationary random processes may be defined by a time-independent probability distribution, or of the mean and variance of the process alone.

The last definition corresponds to the less restrictive wide sense stationary (WSS) random process. For WSS the mean is assumed constant, and the correlation and corresponding covariance $\Re_{ww}(\tau)$ are dependent on time differences between the random variables only [Farrell, 2008, p.122]. Such that

$$E[w(t_1), w(t_2)] \;=\; cor(w(t_1), w(t_2)) \;=\; \Re_{ww}(\tau)$$

for $\tau = t_1 - t_2$, and $\Re_w(\tau)$ equal to the *autocorrelation*. A Fourier transformation for the WSS random process is equivalent to the *Power Spectral Density* (PSD)

$$S_w(j\omega) \;=\; \int_{-\infty}^{\infty} \Re_{ww}(\tau) e^{(-j\omega\tau)} d\tau \ .$$

If $S_w(j\omega)$ is known, the correlation function $\Re_w(\tau)$ equal the inverse Fourier transform of the PSD [Farrell, 2008, p.123].

Gauss-Markov Processes

Gauss Markov processes, as defined in [Gelb, 1974, p.42–43], are a special class of random processes. For the first-order Markov continuous process *x(t)*, the following differential equation apply

$$\frac{dx}{dt} + \beta_1(t)x = w \tag{3.12}$$

for w equal to white noise.
If the probability distributions of both w and x are Gaussian, it follows that *x(t)*

is a Gauss-Markov process. The probability distribution for $x(t_k)$ only depend on the immediately preceding point $x(t_{k-1})$. A stationary Gauss-Markov process is then completely described by the autocorrelation. [Gelb, 1974, p.43]

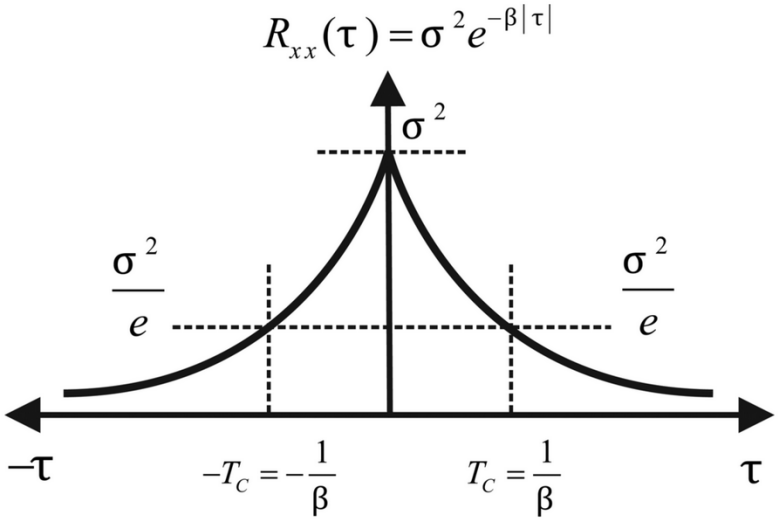

Figure 3.1: *Autocorrelation of Gauss-Markov processes*

The autocorrelation is showed in Figure 3.1[1] The correlation time is given as $1/\beta$.

Gauss-Markov processes are useful in terms of error modeling in navigation systems [Farrell, 2008, p.130].

Random Walk Processes

The random walk parameter is the quantified rate of growth of a sensor output integrated as a function of time.

The definition of a random walk process $x(t)$ below is given in [Farrell, 2008, 134-6].

$$x(t) = \int_0^t \omega(q)dq \tag{3.13}$$

The random walk process in Equation 3.13 describes a Gauss-Markov process, with covariance $P_x(0) = 0$ and autocorrelation $R_\omega(t) = \sigma_\omega^2 \delta(t)$, while the mean $\mu_x(t) = 0$ of x corresponds to the expected value of the state variable *x(t)*. The

[1] *http : //www.mdpi.com/sensors/sensors−13−09549/article_deploy/html/images/sensors−13 − 09549f4 − 1024.png* [Downloaded 2015-05-11]

variance is the second defining parameter of the normal distribution, equal to $var_x(t) = \sigma_\omega^2 t$ in terms of random walk.
The state space model for the same process is $\dot{x} = \nu$, with corresponding PSD for the frequency domain equal to

$$S_x(j\omega) = \frac{\sigma_\nu^2}{\omega^2}$$

White and Coloured Noise

White noise is a stochastic process with constant power at all frequencies [Farrell, 2008, 123]. Unequal distribution of powers per frequency interval indicates *coloured* noise. A continuous-time white noise process often assume a probability distribution represented as Gaussian, and denoted as $\omega \sim N(0, \sigma^2)$ [Farrell, 2008, 124].

For discrete-time, a white noise process v_k for the defined finite range $\omega \in [-\pi, \pi]$, involve the argument of the Kronecker delta function δ_κ

$$\delta_\kappa = \begin{cases} 1 & \text{if } \kappa = 0 \\ 0 & \text{otherwise} \end{cases} \tag{3.14}$$

such that the correlation and corresponding covariance $R_v(\kappa)$, as derived in [Farrell, 2008, 125], is realized by

$$cor(v(t_k), v(t_{k+\kappa})) = R_v(\kappa) \ , \tag{3.15}$$

3.1.2 Linear Kalman Filtering (KF)

The Kalman filter (KF) is a linear state estimation algorithm using a recursive gain sequence for optimizing a system's performance [Farrell, 2008, Ch.5].

System state estimation

Since measurements are sampled at discrete time events, the KF algorithms are also discretely derived. Written as a state-space model, the linear Kalman Filter equals

$$x_k = \Phi_k x_{k-1} + \omega_k \tag{3.16}$$
$$z_k = H_k x_k + \nu_k \tag{3.17}$$

for x_k representing the current state with process noise ω_k. Equation 3.16 show the output z_k as the result of a H_k transform of the current state x_k, along with the additive measurement noiseν_k. [Farrell, 2008, p.170] [Kjørsvik, 2010]

Among the unknown parameters to be estimated are the navigation states of position, velocity and attitude. The navigation states are only indirectly observable, as the navigation system only sense the instrument outputs, for instance the numerically integrated angle and velocity increments of the gyros and accelerometers respectively.

To provide an optimal estimate of the navigation state vector, it must be assumed that the state is observable from the output signal, hence it needs to be modelled. In general, this resembles a kind of "black box" problem, where the actual state of a system is unknown and the observables are signals from the system sensors. The errors contained in the indirect measurements corresponds to functions of the original errors, known as the error propagation [Ghilani, 2010, 2].

For the measurement noise ν_k and system ω_k noise signals at time k respectively, the mean and covariance are defined as follows. [Farrell, 2008, p.171]

$$\begin{aligned} E\langle \nu_k \rangle &= 0 \\ var(\nu_k, \nu_l) &= R_k \delta_{kl} \end{aligned} \tag{3.18}$$

$$\begin{aligned} E\langle \omega_k \rangle &= 0 \\ var(\omega_k, \omega_l) &= Q d_k \delta_{kl} \end{aligned} \tag{3.19}$$

where δ_{kl} is the Kronecker delta function.

The Kalman Filter equations

The objective of KF is achieved by a two-step sequence, consisting of a time prediction and a measurement correction update. The a priori state $\tilde{x}_k$ and corresponding covariance $\tilde{P}_k$ for the time-update are given as

$$\tilde{x}_k = \Phi_{k-1}\hat{x}_{k-1} + G\omega_{k-1} \tag{3.20}$$

$$\tilde{P}_k = \Phi_{k-1}\hat{P}_{k-1}\Phi_{k-1}^T + Qd_{k-1} \tag{3.21}$$

where Φ is the state-transition matrix and G is a constant matrix.
A computed $\tilde{z}_k$ measurement is provided at time k. Given an actual observation z_k, the measurement corrections for the state $\hat{x}$ and covariance $\hat{P}_k$ update at time

k are obtained by the following set of equations:

$$\begin{aligned} \tilde{z}_k &= H_k \tilde{x}_k \\ K_k &= \tilde{P} H_k^T R_k^{-1} \\ \hat{x} &= \tilde{x} + K_k[z_k - \tilde{z}_k] \qquad (3.22) \\ \hat{P}_k &= \tilde{P}_k + [H_k^T R_k^{-1} H_k] \qquad (3.23) \end{aligned}$$

In order to be an optimal estimator in terms of minimum variance, the KF is based on stochastic assumptions. Process noise ω and measurement noise ν parameters are modelled as white, and Gaussian distributed, with zero-mean assumption [Farrell, 2008, p.190] [Jekeli, 2001, p.211].

3.2 Extended Kalman Filtering (EKF)

The trajectory provided in free-inertial by the INS will after some time depart from the true trajectory due to sensor errors [Jekeli, 2001, p.225]. If the INS are allowed to proceed without corrections, the provided position will continue to drift further away from the actual position.

EKF algorithms

The EKF algorithms attempt to satisfy the linear approximation, applied to a time varying process or to non-linear system observations [Jekeli, 2001, p.227].
The extended Kalman Filtering (EKF) is also known as the closed-loop estimation. "Closing-the-loop" means that the sensed indicated quantities are adjusted.

The following set of equations is derived in [Kjørsvik, 2010, p.4].
An initial error estimate at t_0 is assumed

$$\delta x(0) = \tilde{x}(0) - \hat{x}(0) = 0 \qquad (3.24)$$

The true state x_k equal the sum of the a priori state $\tilde{x}_k$ and true error correction δx_k. An observation z_k is further assumed measured.

$$\begin{aligned} x_k &= \tilde{x}_k + \delta x_k \qquad (3.25) \\ z_k &= h_k(x_k) + v_k \qquad (3.26) \end{aligned}$$

for h being a non-linear function, relating the observations z_k to the true state x_k. By utilizing a Jacobian matrix H_k of partial derivatives, for the a priori state $\tilde{x}_k$, the following linear approximation of the error observation δz_k is obtained

$$\delta z_k = z_k - h(\tilde{x}_k) \approx H_k \delta x_k + v_k \tag{3.27}$$

for

$$H_k = \left.\frac{\partial h}{\partial x}\right|_{x=\tilde{x}_k} \tag{3.28}$$

Unlike for the linear version, the time update of the *state* for the extended KF is *trivial*, due to the definition $\delta\tilde{x}_k \equiv 0$.

The optimized state and covariance matrices are further summarized in [Kjørsvik, 2010].

$$\begin{aligned}
\tilde{P}_k &= \Phi_{k-1}\hat{P}_{k-1}\Phi_{k-1}^T + Q_k && (3.29)\\
K_k &= \tilde{P}_k H_k^T [H_k \tilde{P}_k H_k^T + R_k]^{-1} \\
\delta\hat{x}_k &= K_k \delta z_k && (3.30)\\
\hat{P}_k &= (I - K_k H_k)\tilde{P}_k && (3.31)
\end{aligned}$$

For the final corrected navigation state vector update

$$\hat{x}_k = \tilde{x}_k + \delta\hat{x}_k \ . \tag{3.32}$$

Equivalent derivation is found in [Jekeli, 2001, p.226].

Innovation matrix The difference $\delta z = z_k - h_k\tilde{x}_k$ between observed and expected value, is known as the innovation.

Kalman gain K_k equal the Kalman gain matrix, corresponding to the relation between already implemented prior information and the new information.
The gain decides the amount of weight imposed on the innovation, that is how much of the new information is to be added to the estimated a priori state [Jekeli, 2001, p.214]. Since the gain is a function of a stochastic process, it follows that the gain itself will also be a stochastic process [Farrell, 2008, p.207].

3.3 Characteristics of Inertial Navigation Errors

3.3.1 Navigation equations in the e-frame

To form the solution to the differential relations for the navigation state-space model, a set of navigation equations is needed. The primary navigation states are position, velocity and attitude.

The states derived in the i-frame is needed to derive the final navigation states relative to the e-frame. The e-frame derived states further provide the first order differential equations necessary to form the linearised error equations, by means of the EKF state vector.

The following framework presented herein is provided [Kjørsvik, 2010]. The navigation equations are also derived for the various frames-of-reference in [Jekeli, 2001, Sect.4.3].

The position state is the result of the second-order time-derivative of the sensed accelerations realized in the inertial frame. Relative to the inertial frame, the *position* in e-frame equal

$$x^i = C_e^i x^e \tag{3.33}$$

The DCM transform the position in e-frame C_e^i into its corresponding coordinates realized in the i-frame.

The *velocity* is obtained by differentiating the position in Equation 3.33. Velocity corresponds to the first order time-derivative of sensed acceleration. Recall from

$$\dot{x}^i = \dot{C}_e^i x^e + C_e^i \dot{x}^e \tag{3.34}$$

$$= C_e^i \Omega_{ie}^e x^e + C_e^i \dot{x}^e \tag{3.35}$$

For the expression in Equation 3.35, the definition of DCM derivatives is used, as provided in Equation 2.16 of previous chapter.

The derived *acceleration*, that is the second time-differentiation of position, return

$$\ddot{x}^i = C_e^i(\Omega_{ie}^e \Omega_{ie}^e + \dot{\Omega_{ie}^e})x^e + 2C_e^i \Omega_{ie}^e \dot{x}^e + C_e^i \ddot{x}^e \tag{3.36}$$

To obtain the final states realized in e-frame, Equation 3.36 is rewritten in terms of the acceleration in e-frame $\ddot{x}^e$. $\ddot{x}^i$ is substituted in terms of the defined specific force, as given in Equation 2.10. Earth's rotation is assumed constant, to preserve the defining initial frame. The resulting acceleration provided in e-frame is

$$\ddot{x}^e = f^e + g^e - 2\Omega_{ie}^e \dot{x}^e \tag{3.37}$$

for $g^e = g_{att}^e - \Omega_{ie}^e \Omega_{ie}^e x^e$ representing the gravity in e-frame.

Position and velocity in e-frame

$$\frac{d}{dt}\dot{x}^e = f^e + g^e - 2\Omega^e_{ie}\dot{x}^e \tag{3.38}$$

$$\frac{d}{dt}x^e = \dot{x}^e \tag{3.39}$$

The position x^e and velocity $\dot{x}^e$ can further be solved by numerical integration, provided an initial state and known quantities for the forcing functions (i.e. the specific force and gravitational acceleration).

Attitude in e-frame

$$\dot{C}^e_s = C^e_s \Omega^s_{es} \tag{3.40}$$

The sensor orientation C^e_s obtained from the IMU outputs, is utilized for the necessary transformation of accelerations, provided in the s-frame.
The sensed angular rates ω^s_{es} of the IMU's gyro measured in the sensor frame relative to the e-frame equal

$$\Omega^s_{es} = [\omega^s_{es}\times] \tag{3.41}$$

As previously stated in previous chapter 2.2.6, quaternions are usually preferred for the integration of attitude state [Kjørsvik, 2010, p.6].

3.3.2 Linearised error equations

The navigation state error equations for the first order differential equation from Equation 3.1

$$\dot{x}(t) = F(t)x(t) + G(t)u(t) \tag{3.42}$$

is represented by a set of linearly perturbed variables, also known as the linearised error equations. As derived in [Kjørsvik, 2010]

$$\tilde{x}^e = x^e - \delta x^e \tag{3.43}$$

$$\tilde{\dot{x}}^e = \dot{x}^e - \delta \dot{x}^e \tag{3.44}$$

$$\tilde{f}^s = f^s + \delta f^s \tag{3.45}$$

$$\tilde{\omega}^s = \omega^s + \delta \omega^s \tag{3.46}$$

$$\tilde{C}^e_s = (I - \Psi^e)C^e_s \tag{3.47}$$

$$\tilde{g}^e = g^e - \delta g^e \tag{3.48}$$

For a situation of non-linear measurements and time-varying navigation states, the estimation of the *error states* preserves the linear requirement in terms of the filtering. For the linearised error model in Equation 3.49 the three primary navigation states, additional bias terms and error estimate for the gravity correction, are included in the state vector.

Equation 3.49 is equivalent to Equation 3.1, and the matrices can be used to derive the Kalman filter time update. The matrix form in Equation 3.49 provide the necessary framework for the optimal estimation of the error states and biases, found by the linearly perturbed set of equations based on the relations to previously given navigation equations for position, velocy and attitude.

$$\frac{d}{dt}\begin{bmatrix}\delta x^e \\ \delta \dot{x}^e \\ \psi^e\end{bmatrix} = \begin{bmatrix} 0 & I & 0 \\ (\Gamma^e - \Omega^e_{ie}\Omega^e_{ie}) & -2\Omega^e_{ie} & [-f^e\times] \\ 0 & 0 & -\Omega^e_{ie}\end{bmatrix}\begin{bmatrix}\delta x^e \\ \delta \dot{x}^e \\ \psi^e\end{bmatrix} + \begin{bmatrix} 0 & 0 & 0 \\ 0 & -C^e_s & I \\ -C^e_s & 0 & 0\end{bmatrix}\begin{bmatrix}\delta\omega^s_{is} \\ \delta f^s \\ \delta g^e_\epsilon\end{bmatrix} \tag{3.49}$$

The perturbed equations of the position error, velocity error and attitude error are reprodused in Equation 3.52. For the complete derivation, see [Kjørsvik, 2010, p.6-7].

$$\frac{d}{dt}\delta x^e = \delta \dot{x}^e \tag{3.50}$$

$$\frac{d}{dt}\delta \dot{x}^e = -2\Omega^e_{ie}\delta\dot{x}^e + (\Gamma^e - \Omega^e_{ie}\Omega^e_{ie})\delta x^e - [f^e\times]\psi^e - C^e_s\delta f^s + \delta g^e_\epsilon \tag{3.51}$$

$$\frac{d}{dt}\,\psi^e = -\Omega^e_{ie}\psi^e - C^e_s\delta\omega^s_{is} \tag{3.52}$$

The bias terms for the gyro and accelerometer are given as $\delta\omega^s = b^s_\omega - \tilde{b}^s_\omega$ and $\delta f^s = b^s_f - \tilde{b}^s_f$ respectively. The gravity gradient is denoted Γ^e and given as $\partial g^e_{att}/\partial x^e$, in terms of the above definitions. See also [Jekeli, 2001, p.152] for more.

3.4 Aided Inertial Navigation

3.4.1 Integrated GNSS/INS

GNSS is considered a low rate sensor, as opposed to high rate sensors like gyroscopes or accelerometers, which constitutes an IMU. In navigation systems, low

rate sensors can be utilized to further correct the integrated navigation outputs of the combined INS [Farrell, 2008, p.6].

For instance, absolute positioning systems such as GPS, can provide correction of the drift in the INS [Woodman, 2007, p.33].

Integrated navigation systems with satellite positioning benefits from the short term stability of the INS measurements and complimentary measurements from the long term stability of the GNSS observations.
Predicted navigation states of position and velocity from the INS helps to detect cycle slips in the GPS receiver and in general helps to smooth out the observation noise of the GNSS observations. In return, the GNSS observations will compensate for the INS error effects [Cramer, 1997, p.6].

The combination with GNSS provides among other, control of the INS error propagation. For calculation of a trajectory, coordinates can be calculated in nearly real-time by using a Kalman filtering technique [Torge and Müller, 2012, pp.213-214].

Satellite positioning by a GNSS, have today become indispensable in terms of utilizing positioning systems in most geodetic applications. It is relatively low-cost and easily available [Torge and Müller, 2012, p.214].

The flowchart in Figure 3.2 illustrates the outline of an aided INS system.

3.5 Review of aided INS

A review of an aided Inertial Navigation System with Extended Kalman Filtering (EKF), is presented by the flowchart in Figure 3.2.

The filter design corresponds to a *complimentary filter*, as the EKF input data is given as the differences representing the discrepancies between the INS states and the aiding system states provided by the external sensor. Hence, only the dynamics of the errors in the platform actually enter the system, as opposed to the dynamics of the navigation states. This approach will preserve the linear requirement, hence avoiding further filter tuning, as emphasized in [Kjørsvik, 2010].

Errors occur due to the imperfect initial state and noise related to the inertial sensors, hence the integrated state provided by the INS will diverge from the true state. Aiding sensors providing external information can be included in order to smooth out the sensors noise and correct the estimates.

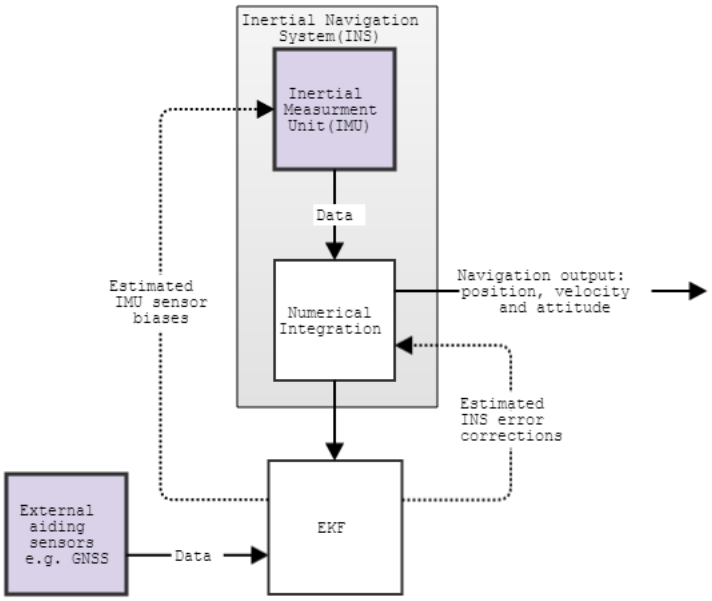

Figure 3.2: *Flowchart for an aided Inertial Navigation System*

The EKF is an optimal estimator, as defined by minimum variance. Filter algorithms entails the estimation of the time updated error covariance, and the measurement update and correction of system states. Time update of the state is obtained by numerically integrating the navigation state in the INS, by using the sensed IMU outputs. Hence the time update of the state, though not the covariance, is said to be trivial.
Numerically integrated time updated and corrected state is denoted as navigation *output*, in the chart above. Estimated error terms for the gyro and accelerometer biases, as denoted by the second dashed arrow emerging left from the EKF, are also provided along with the INS state corrections.

Aiding observations from a GNSS are the most commonly used in outdoor navigation applications.

The derived theory, as reviewed in short herein, is found among other in [Jekeli, 2001, Ch.7], [Farrell, 2008, Ch.4] and [Kjørsvik, 2010].

Chapter 4

Part I: Relative tie points (RTP) aiding in tunnel surveying

4.1 Introduction

The overarching motivation of this study is to reduce cost and time consuming processes related to position aiding by using land surveyed adjustment points for tunnel projects. Establishing the landmark points may even cause the tunnel to be closed while surveying, which in turn is highly expensive. If a closure can be avoided parallel to preserving the required accuracy, it would increase the efficiency and lower the costs significantly.

Adjustment points are used to generate the reference trajectory needed in order to obtain the required accuracy for mobile mapping applications. This part concerns the use of relative tie points (RTP) only, that is without the use of land surveying inside the tunnel. The definition of adjustment points, as opposed to tie point and control points, is provided in the beginning.

The analysis is based on an empirical research of a sampled dataset. Further description of the field work is provided in the following section.

Though not originally intended, it turns out that the resulting problem herein corresponds to some of the so called "full SLAM" problem [Thrun and Fox, 2006]. To explain the research's application to SLAM problematic, some background knowledge related to full SLAM is provided in the theory section.

A framework for the relative tie points is derived at first. Research and field work descriptions, post-processing of data and further treatment of observations follow the theory section.

Multirun solutions with relative tie points will cause constraints in the sampled lidar data. Hence RTP introduce additional information about the dataset by the relative relations between the tie points. The constrain caused by the RTPs maintain the consistency in the dataset.

4.2 Relative tie point (RTP) aiding

A minimum of two measurements of the same defined feature defines a tie point. Without an absolute reference to a distinct reference frame, the points are only observed relative to each other. This defines a local relative net of observations.

Figure 4.1 illustrates the principle of utilizing relative observations of tie points for positioning of the trajectory.

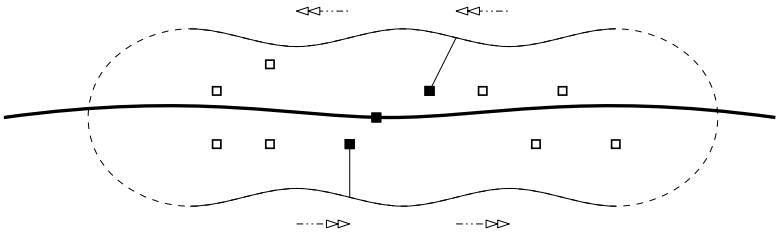

Figure 4.1: *Navigation aid by observation of relative tie points (RTP). A feature is observed once for a run going from left to right in the figure. The same feature is observed once from another run going the opposite way, from right to left. Only the observing vehicle has moved during the time of the observations of the feature. The feature's position is constant, and the observations are vectors of length and direction between the vehicles reference point and the feature.*
The emphasized line in the middle represent the resulting trajectory when using the observed feature as a common reference, hence linking the vehicles observations together. The observed feature functions as a tie point.

The feature need necessarily not only be observed in separate runs, as in the illustration. Observations of the same feature may also arise more than once for the same run.

The observations are vectors, measured by the lidar scanner, between the vehicle and the feature. An observation l has therefore the property of both length and direction. Assuming two vector measurements for the same observed feature, i.e.

tie point, a baseline between the vector are indirectly known. The baseline corresponds to a computed straight line between the vehicle's location at the time of the observations.

Observations are relatively defined in the sensor frame (s-frame). To be referred to the global reference frame (e-frame), the transformation from sensor frame to earth frame is necessary. This will be explained later in this section.

Information from sensors providing relative measurements between it and observed features can be used to improve the knowledge about locations referred to the global reference frame [Smith and Cheeseman, 1987]. As a vehicle moves unaided away from a known initial position, uncertainties in the vehicle's location emerge. Position estimates based on inaccurate information will in turn result in errors. Errors will be allowed to accumulate and increase the uncertainty of the position, until new information enter the system to correct the navigation state.

For a moving vehicle sampling at discrete events, the relation between it and its environment will also be discretely known. The vehicle's location is known by its last state and the relative change in state since last system update. The vehicle's current position, at any time, corresponds to a recursive state update. For discrete system state updates the position is defined by

$$X_{k+1} = X_k \ + \ \Delta X \ , \tag{4.1}$$

describing the way a relative change in position ΔX will vary from a state k to the next, at *k+1*. All observations added to the system will further increase the amount of information included in the system.

Observations here represents the defined vector between the vehicle and the measured feature, as observed by the lidar scanner.

A defined lever-arm l^p_{lidar} between the IMU and the lidar, is assumed known and included in the mounting specifications. The C^p_{lidar} rotation is assumed known and constant. The rotation matrix C^e_p is the result of the numerical integration of the IMU sensor outputs.

The $l^{lidar}_{X_{tie}}$ is the *measured* vector, between the lidar and the tie point feature, relative to the platform frame. The vector l^e corresponds to the *computed* mathematical relation between the vehicle and the tie point, relative to the global reference (e-frame).

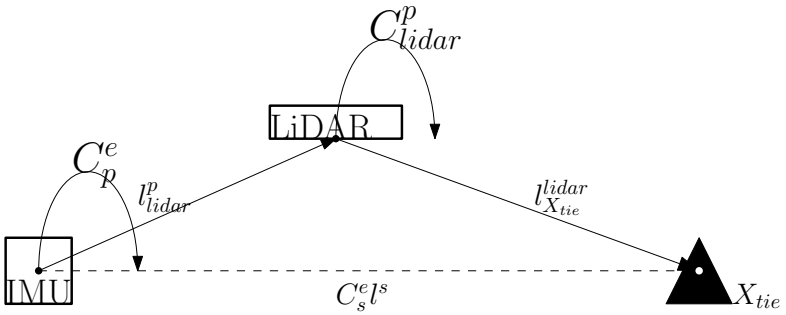

Figure 4.2: *Mechanics of the relative tie point (RTP) aided positioning system.*

The system of vectors and transformations from Figure 4.2 are equal to the system in Equation **??**, as derived in the e-frame below

$$l^e \;=\; x^e_{tie} - x^e \;=\; C^e_s l^s$$

Position x^e refer to the vehicle's reference point located in the IMU. The position of the (RTP) measurements is denoted x^e_{tie}. The quantity l^e is the vector observation, measured by the lidar scanners and later transformed into the e-frame by the rotation matrix C^e_s, from s-frame to e-frame.

4.3 Theory of SLAM

When utilizing relative tie points (RTP) for position aiding in tunnel surveys, both the tie points and the vehicle's trajectory are unknown. By this definition, it turns out that the problem actually corresponds to a version of a Simultaneously Localization and Mapping problem, known as the *full SLAM* problem.

SLAM problems originally arise from the field of robotics, and involve the estimation of the position of the robot itself and the mapping of its surroundings, while moving about. The mapping and robot estimates in the robotics literature corresponds to the tunnel environment and the mobile mapping vehicle.

The literature by [Thrun and Fox, 2006] thoroughly derives the basics of theory in terms of the robotics approach to the problem.

Though the application to the tunnel positioning by RTP results in full SLAM, it was initially not intended as such. Compared to the actual full SLAM defined issues, not all are present in the RTP aiding problem of this research. Hence

the SLAM problem in terms of this research are to some extent simplified. For instance, the SLAM problem related to the feature detection are not applicable in this case, as the tie points are assumed unambiguous.
As a result, the SLAM issue at hand in the RTP position aiding narrows down to the simultaneous estimation of the vehicle's own position and the tie points of interest only.

Full SLAM According to [Thrun and Fox, 2006, Ch.10], the a posteriori is defined as the probability function p of the entire trajectory $x_{1:t}$ and the mapping m of the environment, given the measurements z and controls u.

$$p(x_{1:t},\ m \mid z_{1:t},\ u_{1:t}) \tag{4.2}$$

The SLAM defined in Equation 4.2 is not perfectly applicable to the RTP study herein. The designs differ in terms of u, which does not apply to the mechanized problem design of the RTPs.
The state updates of the system can be performed by use of e.g. the EKF algorithms.

The same measurements are used for estimation of both the vehicle's position as well as its environment. As a result, the estimates are correlated. Uncertainties of the vehicle's position hence affects the uncertainty of tie point position estimates, and vice versa.

This is further illustrated by the covariance matrix in Figure 4.3. The elements outside the diagonal denotes the coefficients of correlation. The diagonal are the variances of the estimated elements of the system state.

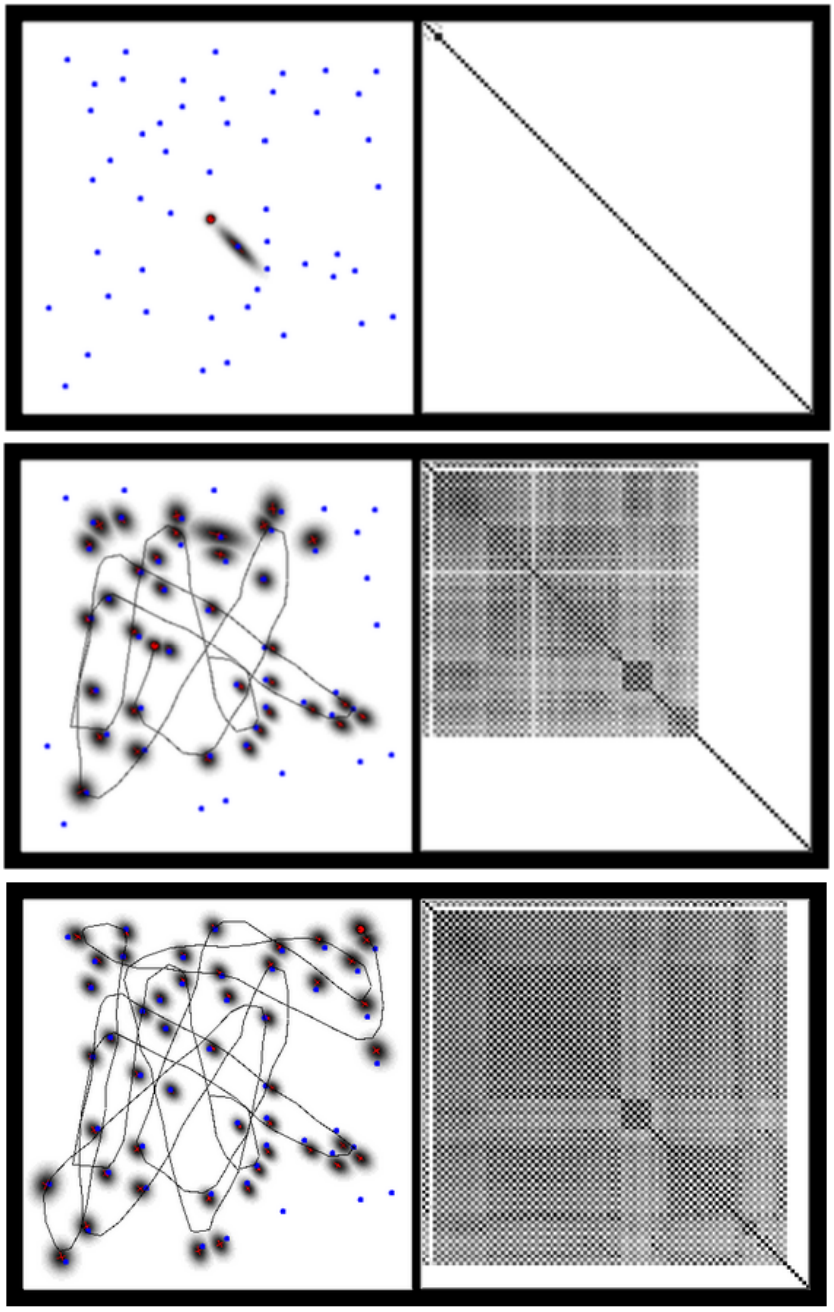

Figure 4.3: *Illustrated association between uncertainty of estimated position (left row in figures) and its corresponding correlation matrix (to the right) along with the vehicle movements in time. [Thrun and Fox, 2006, p.325]*

4.4 Field work and processing of RTP solution

Tunnels define the research problem herein. As no satellite signals are available in tunnels, the system cannot utilize GNSS. Apart from the independent INS state estimation, only odometer outputs are present. The INS and odometer sensor do not rely on any external sources of signals.

The last GNSS generated observation of position before the tunnel represents the initial position estimate for the navigation integration. GNSS/INS combined solution provides an accurate trajectory when outside the tunnel. When GNSS observations are unavailable inside the tunnel, position errors are allowed to accumulate. The drifting in position is due to the integration of the noisy and biased IMU data. The odometer measurements also contain errors, and are only sensitive to along-track motion.

The post-processing in TerraPos reduces the accumulated errors by calibration parameters and smoothing algorithms, to obtain the resulting trajectory. The implemented smoother equal the fixed-interval *Rauch-Tung-Striebel* two-pass smoother, applied to the Kalman filter estimates. A first forward-pass saves the intermediate estimates, sequentially followed by a second pass running backwards in time, hence smoothing the first estimates. More about smoother algorithms is found in [Grewal and Andrews, 2001, pp.160-164].

In order to reach the required accuracy, absolute reference by measured GCPs are usually included in the post-processing. The process of GCP aiding is both time consuming and costly. The following research investigates the necessity of GCP aiding, without having to challenge the required accuracy. Either by excluding adjustment points entirely, or by identifying a possible threshold of a significant amount of points needed.

This chapter raises four hypotheses concerning external aiding of the navigation solution based upon relative tie point (RTP) observations. The tie points represent relative constraints for the positioning inside the tunnel.

The field work is presented in the following section, accompanied by the further description and post-processing of the dataset. Analysis and further discussion are given last.

4.4.1 Field work

Lapplia tunnel The tunnel lies along the E6 main road, and is piercing the steep west side of the river valley, named Lapplia. For the purpose of this research, it is hereby referred to as the Lapplia tunnel. The data collection for this research was conducted in November 2014. An overview map with accompanying detail of the tunnel is given in Figure 4.4.

This particular tunnel is found in the northernmost end of the dataset, given in Figure 4.5. The open space alongside the trajectory, approximately parallel to longitude 14.4 degrees, implies the tunnel's location. The gap is due to missing GNSS data. The length of the tunnel is relatively short, only about a kilometre long. For an average velocity of 11 m/s, the GNSS outage due to the tunnel lasts for about one minute.

Figure 4.4: *Overview and detail of the Lapplia tunnel. Screenshot from www.norgeskart.no (left) and Google Earth (right) [Downloaded 2015-04-03]. KML overlay of post-processed trajectory exported from the TerraPos solution.*

4.4.2 Data sampling and equipment

For the Lapplia tunnel there are a total of six runs, of which three are in the direction heading from the *south end to north* and from the *north end to south*. The grey fields in Figure 4.6 below show the respective six outage periods representing the six runs through the tunnel. The width of the grey fields implies the duration in time inside the tunnel. A wider grey field denotes a longer blockage of GNSS signals and a lower average velocity. The graphs in the same figure denote the speed of each run. Throughout the tunnel, the velocity is attempted kept constant. As given in the plot, the first two runs are samples with an average speed of about 11 m/s, with the last four at 20 m/s.

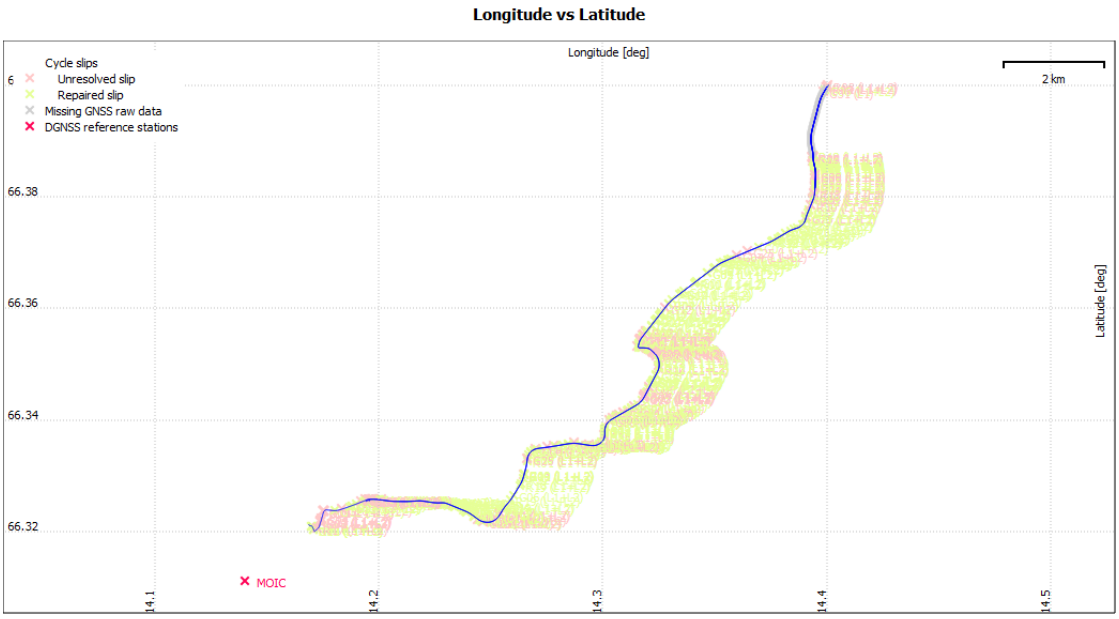

Figure 4.5: *Trajectory processed in TerraPos, including the Lapplia tunnel in the northernmost end.*

Equipment Referring to previous sections, the instrument mounting of positioning sensors includes two GNSS antennas on the roof, a DMI on the wheel, and one IMU of type LN-200. A stationary permanent GNSS reference station[1] is depicted as MOIC in Figure 4.5 above. The positioning system utilizes DGNSS measurements, incorporated GNSS/INS integration by the use an Extended Kalman filter (EKF), together with the odometer measurements.

Lidar lever-arm observations The other sensors in the vehicle mounting equal two lidar scanners, four cameras and one video recording device. All of the mentioned are originally utilized as mapping sensors. For the application of the relative tie point observations, lidar measurements are also exploited for positioning purposes.

The lidar measure vectors of range and direction. An observed vector between the lidar scanner and a tie point feature equal one relative tie point observation. The relative principals based on mathematical relations were derived in the former section.

[1]CPOS. URL: *http* : *//kartverket.no/posisjonstjenester/cpos/* [Downloaded 2015-05-11]

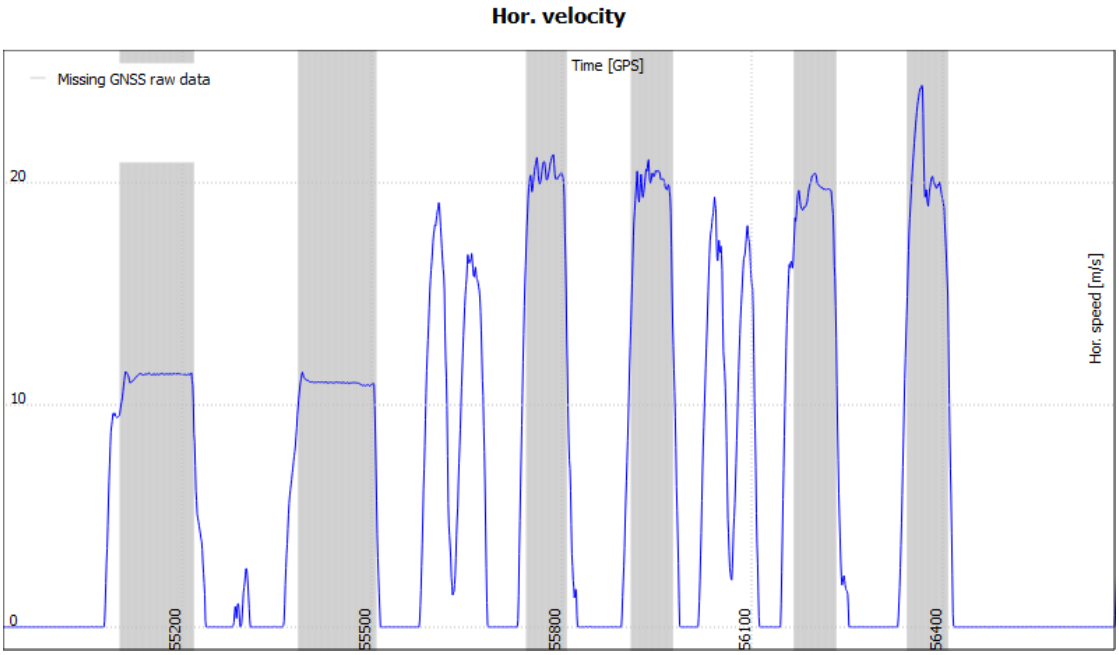

Figure 4.6: *Horizontal velocity of the six runs through the Lapplia tunnel. Roughly 11 m/s and 20 m/s respectively, in terms of the two first and the four last runs.*

Raw data and measurement structure The raw data of the observed lidar vector measurements are provided in XML-format. The original measured adjustment points are provided in the same XML files. The adjustment points are given with reference coordinates. Recall that the tie points are only relative, and only contain the lidar vector measurements. Hence they have no coordinate data attached. The adjustment points are given as points defined in either one-, two- or three dimensions. They are used in the post-processed reference solution, which is needed to compute true errors of the final trajectory. True error is a measure for the absolute accuracy.

Description of tie point XML data For every hypothesis involving a different amount of tie points, a separate copy of the original XML-file of observation data was made and edited to fit the individual research designs.
For the further analysis of the tie points only solutions, all the coordinates of the adjustment points from the original XML file were deleted, hence only observed tie points remained. Without coordinates, the adjustment points are still implemented in the dataset, though functioning as additional tie points with a related lidar vector observation.

4.5 Data processing

TerraPos is utilized for post-processing of the navigation solution. The processed solutions are then exported as a text file (ASCII-format) and imported in MATLAB for further analysis.

4.5.1 Generating XML files of various amount of tie points

An efficient selection of tie points involved reducing the dataset by half its size, recursively, until an interval by a certain amount of points was detected. The aim is to locate the least amount of tie points necessary to preserve the required accuracy.

In large datasets, such as this, it is necessary to utilize an efficient time-saving method for the detection of a significant amount of points, without having to search through the entire dataset. Searching through every possible combination would be unnecessary and time-consuming.

The halving method used corresponds to a bi-sectioning procedure, and would much faster located the interval of interest. Every combination are hence not evaluated, but as later argued, would be of no use either.

The selection of edited XML-files was post-processed in TerraPos to locate the minimum amount of tie points needed. Calculation of the 95 percentile of the position errors was used to detect the significant threshold. This is further explained in the following RTP analysis section.

Findings from this procedure are plotted in Figure 4.9 and 4.10, presented in the subsequent section.

4.5.2 Post-processing in TerraPos

The necessary processed solutions for the analysis include the reference trajectory, the non-aided trajectory and several versions of RTP aided trajectories, for the purpose of the hypotheses testing.

Generating the reference trajectory To assess the absolute accuracy, expressed by true errors, a reference is necessary. The reference trajectory is based upon all possible information available, including all the available adjustment

points and tie points, the base station reference, in addition to the INS and odometer data. The accuracy of the adjustment points is about 2 centimetres, and the points are evenly spread apart by a distance of 10 or 20 meter throughout the tunnel.
As previously emphasized, the DGNSS aiding only contribute with information outside the tunnel. Still, GNSS data are used to derived the estimate of the complete trajectory. The reference solution will therefore have the best available position aiding, and will involve the least amount of accumulated error for each tunnel run.

It is to be expected that the quality of the reference trajectory is dominated by the accuracy of the adjustment points, and therefore be at the level of a few cm.

Minimal-aided solution The non-aided solution only include the inertial navigation sensor and the odometer measurements. Hence this solution is based on nearly free-inertial properties. The generated solution represents the absolute worst case scenario, due to inclusion of the minimum amount of information. Since the positioning solution based on the IMU will tend do drift over time, when lacking proper positioning aid, this solution will have the largest accumulation of errors for each tunnel run. The drift in position is due to the error propagation in the integration of the IMU sensor outputs, noise in the odometer data, and imperfect knowledge of the navigation states at each end of the outage.

RTP aided solutions In addition to RTP solutions including all available tie points or no tie points at all, solutions are also generated for various amounts of tie points. The applied bi-sectioning method for editing XML-files explained previously is used to process the corresponding RTP aided processed solutions in TerraPos. The solutions will serve as the basis of the hypotheses testing and analysis in the following section.

Export from TerraPos For the export, a predefined format file was first generated. This simplifies the process of export, as every export will turn out exactly the same. Since the object of research are the tunnels, the export include the use of a so called "event file" containing the 1 Hz rate time events in GPS time for the tunnels only. The event files where generated in MATLAB, corresponding to a simple vector n-dimensions saved as a text-file output in ASCII format. By utilizing these event files in the export from TerraPos, the result is data only for the tunnels of interest. This is how the various solutions in terms of speed and number of runs are generated.

Number of tie points The table below states how many tie points the various XML-files used for the RTP position aided in the post-processing.

	1d points	**2d points**	**Tie points total**
Solution for 11 m/s	26	73	99
Solution* for 20 m/s	26	61	87
Solution** for 20 m/s	30	57	87
Both * and ** for 20 m/s	41	81	122
For all six solution	47	85	132

Table 4.1: *Number of tie points in the respective XML-files used in post-processing.*

The notation * and ** denotes two distinct combinations of runs sampled by speed of 20 m/s. In total there are four runs sampled at this velocity, and the first two and the last two of these four are implied by the asterisk notations. Hence it only implies two different combinations of runs, not containing the same processed solutions.

MATLAB computation

MATLAB is used for the purpose of generating the statistics from the TerraPos exported solutions, resulting in plots and tables for further analysis. The results are given in the analysis and discussion section that follows.

4.6 Analysis and discussion of RTP hypotheses

The topic of research in Part I is concentrated on the use of external aiding when the satellite signals are blocked. This occur for instance when the vehicle enters a tunnel. The aim of this part is to conclude with some final guide lines concerning the RTP aiding. The conclusion will based on the analysis of the four defined hypothesis in this section.

The computations conducted in MATLAB are presented as plots and tables for statistical data in this section. The analyses are given sequentially in terms of the hypotheses of consideration, and defined in the local level frame (g-frame).

The MATLAB generated plots represents the true errors. Event files for the GPS time[2] for each tunnel passing are used for the export from TerraPos. Recall that true errors are the difference between the test data of interest and the reference trajectory. By using the reference, the quality is measured as an absolute accuracy in meter.

95 percentile The statistical measure of error acceptance is represented as the 95 percentile error of the vector made from sorted ascending absolute error quantities. This means that 95 percent of the errors are expected to fit inside this interval. The errors represented by this measure are assumed to occur when the system is at its worse.
A probable candidate of the largest error is therefore most likely to be found in the middle.

The largest errors are expected to be located in the middle of the tunnel and only for significantly short time interval. The remaining errors on each end of the small time interval containing the largest errors are expected much small, as the overall accuracy of the dataset is small.

The 95 percentile is chosen above the alternative quality measures, such as the standard deviation σ or RMS quantities. Due to the expected symmetrical distribution of errors and small errors for the majority of the measurements, the use of σ or RMS would not return a similar quality measure of the largest errors, which is the one of interest.
Since the largest errors only occur at a short period of time, the quality measures of the standard deviation σ or RMS quantities these large errors will disappear in the overall accuracy, which is relatively small.

[2]GPS time are given as Time Of Week (TOW), measured in seconds.

The representative 95 percentile is arbitrarily chosen to go with the expected amount of errors in the dataset, and used as the quality measure for distinguishing the threshold for error acceptance in the data.
Assume the maximum value from the range of errors of each navigation solution are provided together with the percentile. A significantly large discrepancy between the maximum error quantity and the 95 percentile may signalize outliers in the data. Large outliers are to be considered as possible non-representative values or blunders to be excluded from the actual dataset.

4.6.1 Research question 1.a: DIFFERENCE BETWEEN TIE POINTS AND NO TIE POINTS

The research in this section search to investigate if there is any difference in including relative tie points (RTP) for position aiding or not. As already stated initially, RTP adds constraints to the data, hence improves the consistency of the resulting solutions. For this purpose, the true errors are computed by subtracting the tie point aided solution from the reference. The definition of the Fisher-information matrix states that added information is always positive [Jekeli, 2001, p.207].

The expected answer to the question about tie points would be yes. The relative tie points are expected to link the different separate runs together, creating a corrected trajectory from the two relative solutions. For the opposite event with no relative information linking the separate solutions, each passing through the tunnel will result in independent trajectories of lesser accuracy than the combined solution by RTP linking.

If the research confirms the expected outcome and returns a significant difference, it follows a need to explore how large this difference actually is in quantifiable terms.

Figure 4.7 displays the true errors for the first two runs sampled by a speed of 11 m/s. The true errors of the solution including position aiding by RTP and the solution having no aiding by RTP, are represented by the continuous green line and stitched blue line respectively.
The second Figure 4.8 shows a similar plot, though instead for the processed solution based on the data sampled at a larger speed of 20 m/s.

As the estimated trajectory will be less accurate when processed without adjustment point coordinate information, both the unaided and the RTP solutions are expected to deviate from the adjustment point aided reference solution. As the Figure 4.7 show, the largest deviations from the reference are registered in the East

component, representing a third of the error as opposed to the North component. Considering only the size of the error, it is no significant difference between having RTP aid and having odometer aiding only.

Each subplot in Figure 4.7 show two graphs representing true error for two tunnel runs. Note that the two graphs originates from opposite directions in terms of the data sampling. The nature of relative tie point linkage causes the true errors of the RTP solution to always head in the same direction, as is evident in terms of the error plots. As a matter of course, this will not be a property contained in the solution without RTP. The stitched lines representing the true errors of the non-aided solution are hence more unstable and will point in different directions.

The error curves of the Down component for both Figure 4.7 and 4.8 are nearly coinciding. This implies that utilizing RTP aiding do not directly have an impact on the errors affecting the Down component. On the other hand, since the errors are dragging in the same direction, both for the aided and unaided case, it may imply some unmodeled systematic errors in the measurements caused by exterior effects. If such an error is evident, it is more prominent in the case of speed equal to 20 m/s. Based on the compared difference in true errors between Figure 4.7 and 4.8, the error in the Down component are doubtlessly dependent on the speed. The Down component and possible errors will be discussed in further depth in later sections.

Based on the results in Figure 4.7 and 4.8, RTP positional aiding does neither directly increase nor decrease the size of the absolute accuracy error size by a significant amount. Instead, RTP aiding does have an effect on the linking of the trajectories due to its relative nature that may be beneficial for the further error detections. Recall the initial comment concerning the constraints represented by the relative observations, causing a general consistency in the dataset.

4.6.2 Research question 1.b: RECOMMENDED DENSITY OF TIE POINTS FOR REQUIRED ACCURACY

While the former question concerned the difference of having tie points or not, this section attempt to quantify a minimum requirement of the amount of tie points needed for the highest achievable accuracy. For the generated XML-files with various amount of tie points included, the 95 percentile true errors are plotted for the respective solutions, given in Figure 4.9 and 4.10. The largest error is represented by the 95 percentile error threshold measure, as is previously defined.

The graph of the solutions sorted in ascending order are expected to close in on

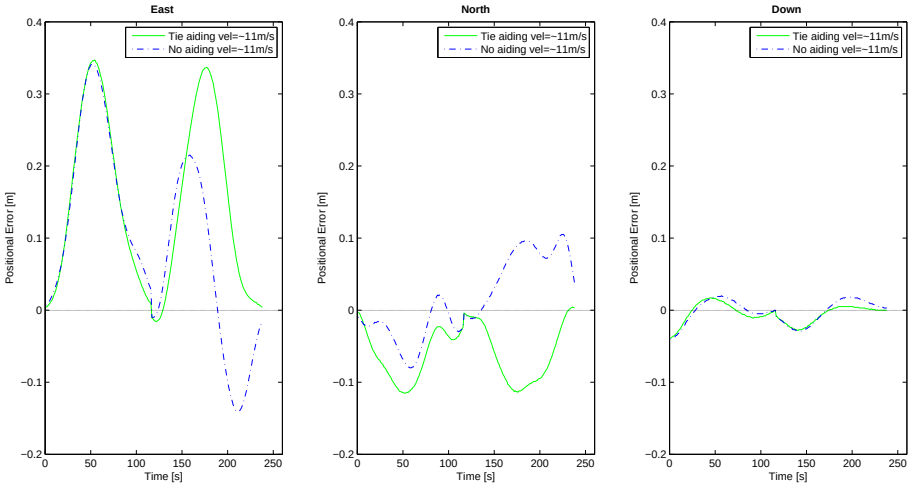

Figure 4.7: *Processed tie point aided solution collected at velocity 11 m/s*

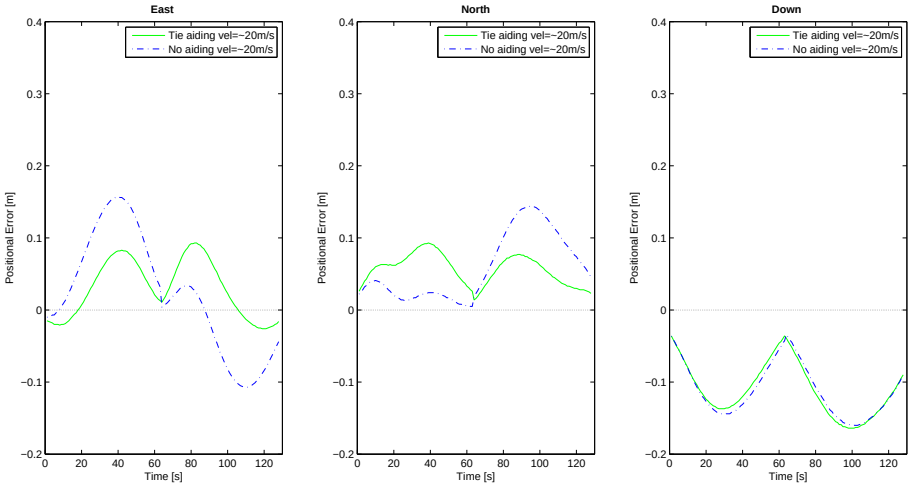

Figure 4.8: *Processed tie point aided solution collected at speed 20 m/s*

one constant value, representing the highest possible accuracy provided by the solution of that dataset.

The Fisher-information principle state that adding new measurement will not contribute to removing information from the dataset. Continuously adding data will always contain some level of information and will always be positive, i.e. larger than zero. [Jekeli, 2001, p.207] This fact may imply that there can exist a possible threshold for a dataset, such that for new measurements added provides a very small amount of additional information to the system. For the purpose of efficiency, detecting such a threshold are of interest.
If for instance 20 tie points return almost the same amount of information as 70 tie points, the workload of defining 70 tie points instead of 20 is significantly higher, when considering the amount of necessary RTPs for a survey project.

The plots in Figure 4.9 and 4.10 are generated in MATLAB. They represent the 95 percentile true errors for the solutions sampled with the speed of 11 m/s and 20 m/s respectively. The number of tie points for the solutions are given on the horizontal axis, with corresponding variable of positional error in absolute accuracy indicated on the vertical.

The 95 percentile computed for the non-aided solution, as is represented by the red line, is included in the figures for comparison. The difference in errors due to velocity is the object of research in the succeeding section.

Interpretation of the plots gives that the East component for speed 11 m/s is the last to converge. For the trajectory sampled at speed about 20 m/s the threshold represented by the 95 percentile positional error seems to converge between a RTP solution consisting of only 5 – 10 tie points, since the 95 percentile errors of solutions based on an increasing amounts of tie points is not resulting in a lower errors.

Sensitivity to outliers are verified by a further study of various amounts of tie points. If the statistics based on the 95 percentile are computed on a possibly skewed vector of true errors, the convergence may turn out ambiguous. This might be the case in the East component in Figure 4.9, as there might be some measurements of large uncertainties still left in the dataset, hence the convergence is harder to conclude. However, the variations in the positional errors are subdecimetre, and the threshold seems to be in the interval between 10 – 20 tie points.
For the North component 10 tie points may suffice. Despite that, the ambiguous positional errors in the East component will perhaps make it necessary to include more than the sufficient 10, since this component inhabits the largest uncertainty.

Still, needing only 10 – 20 RTPs is of a significant contrast to an amount of nearly 100 RTPs. Defining only 10 – 20 ties is notably less time-consuming and resource-demanding. For shorter tunnels like the Lapplia tunnel, i.e. about 1 – 2 km, the results indicate that this is a realistic estimate.
If the accuracy required for the application is covered by the accuracy possible by the RTP aiding, a number of tie points exceeding the tie point threshold will not contribute significantly to a higher accuracy.

A recommendation in terms of density will be defined by the length of the tunnel divided by the number of tie points. For instance, for the Lapplia tunnel of about 1 km and for an amount of 20 ties, the density between uniformly distributed tie points throughout the tunnel will equal the ratio 20/1000 m. This represents a distance of 50 meters between each defined tie point. The results presented in Figure 4.9 and 4.10 implies that 10 ties would probably be sufficient in most cases, in terms of the accuracy. The resulting density of tie points in such case then equal a distance of 100 m between each defined tie point.

4.6.3 Research question 2: THE EFFECT OF SPEED

The length of the tunnel affects the time interval without GNSS positioning aid. The speed is dependent on the time parameter. The amount of time spent inside the tunnel is thus an additional parameter in terms of error accumulation and high-precision positioning, since the IMU is operating in nearly free-inertial mode.

Because the nature of the variance of the errors tend to drift with time, hence the probability of increasing error quantities, speed is critical in the evaluation of obtained accuracy of RTP.

Figure 4.7 and 4.8 represents the absolute accuracy in terms of true errors for the navigation solutions acquired at a speed of 11 m/s and 20 m/s respectively. The plots confirm the fact that a higher speed results in a reduced accumulation of error. For the higher speed of 20 m/s, errors are generally smaller than for the corresponding 11 m/s. The time parameter is directly proportional to the uncertainty accumulation in the inertial navigation states. Hence an increase in speed ensures a shorter stay inside the tunnel, the following true errors will consequently be smaller.

The Down component represented by ellipsoidal height, is more susceptible to errors in the gravitational acceleration g and the errors behaves differently than the other two components in terms of the change in speed.

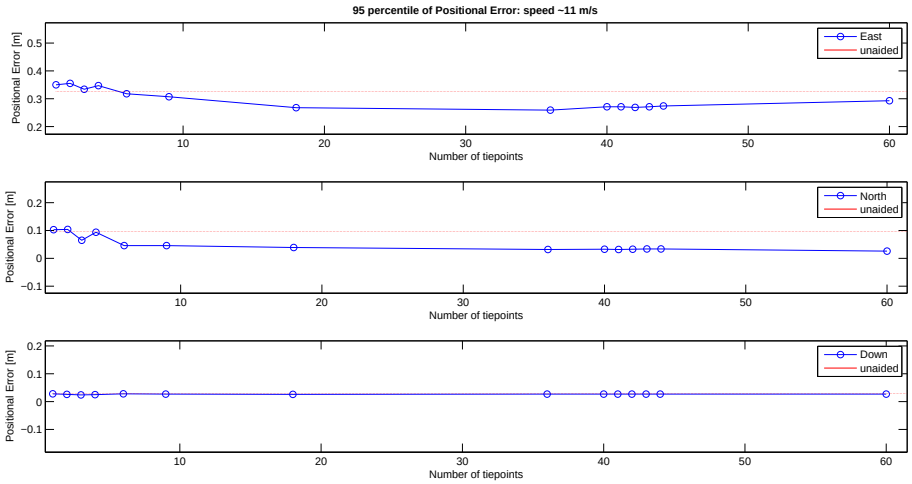

Figure 4.9: *95 percentile error in processed solutions based on various amount of tie points sampled at speed 11 m/s. Positional errors are approaching a constant.*

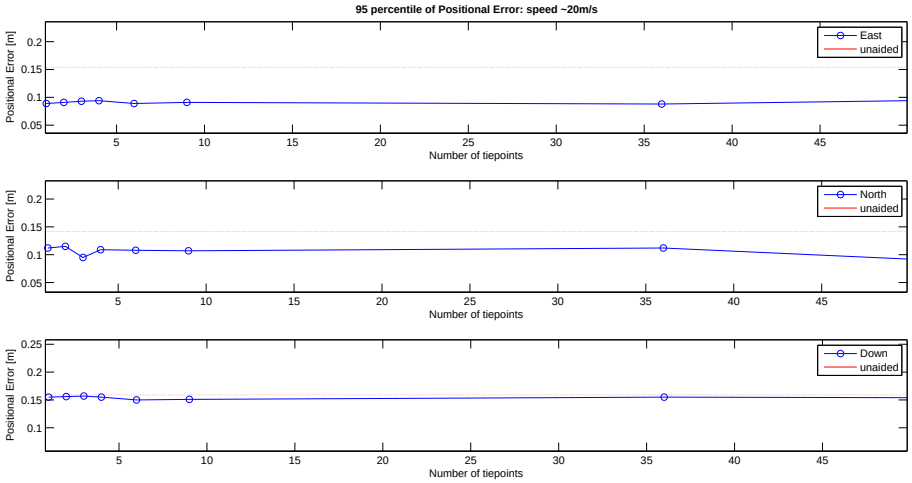

Figure 4.10: *95 percentile error in processed solutions based on various amount of tie points sampled at speed 20 m/s. Positional errors are approaching a constant.*

Table 4.3 further presents the quantities of the largest acceptable error in the observation sets observed at different speed. The largest errors are found in the East and Down components. The 95 percentile of the 20 m/s runs are generally larger than for 11 m/s. In terms of the East component, the 95 percentile for 11 m/s is roughly twice the size as the runs by speed of 20 m/s.

Based on the presented error statistics of absolute accuracy, the following conclusion is derived. In terms of the grid coordinates of East and North, the highest possible speed is the most beneficial option. For the Down component, an increase in speed alone will not provide a reduction in the true errors. As the RTP aiding and change in speed shows no evidence so far of any improvement in terms of the accuracy. Further investigation of other possible unmodeled exterior effects affecting the inertial navigation states must be performed to make any final conclusion.

By result, it is clearly an advantage to have as high speed as possible. Nevertheless, the highest possible speed is also limited by certain restrictive factors.

Traffic regulations, such as speed limits and traffic in general, are probably the main limiting factors. The sampling rate of the laser scanners is another candidate. The point density requirements must be fulfilled, which is often ensured by a lower speed. However, new technology in lidar sensors eliminates this obstacle, and inside of the other restrictions this is no longer a problem. Point density will be ensured by both 11 m/s and 20 m/s. Also, by the fact that for RTP measurement the tunnel needs to be passed through at least twice, the point density will improve by merging point clouds from more than one scan. The same tie points will also merge the scan data. The scanner rate is hence a limiting factor of little actual importance. Due to the sequential repetition of passings providing merged observations data, the point density will be good enough at all higher considered quantities of speed anyway.

Results presented show a difference in terms of absolute accuracy obtained by a speed of 11 m/s and 20 m/s. Hence, a short GNSS outage is a more important factor than high density of tie points. Limitations restricting the highest possible speed are mainly the traffic regulations, as the scanner rate is improved by new technology. A speed of 20 m/s is realistic and will provide a good enough absolute accuracy in many applications, without the need for land-surveyed adjustment points.
The research argues that this conclusion will be valid for shorter tunnels, of similar properties given for the Lapplia tunnel.

		95 percentile	Maximum value	Diff.
East				
	Run 11 m/s (2 x)	0.326	0.342	0.016
	Run 20 m/s (2 x)*	0.154	0.157	0.003
	Run 20 m/s (2 x)**	0.387	0.392	0.005
	Run 20 m/s (4 x)	0.373	0.392	0.019
	All runs (6 x)	0.247	0.295	0.048
North				
	Run 11 m/s (2 x)	0.096	0.105	0.009
	Run 20 m/s (2 x)*	0.142	0.144	0.002
	Run 20 m/s (2 x)**	0.305	0.310	0.005
	Run 20 m/s (4 x)	0.286	0.310	0.024
	All runs (6 x)	0.260	0.345	0.085
Down				
	Run 11 m/s (2 x)	0.029	0.040	0.011
	Run 20 m/s (2 x)*	0.159	0.160	0.001
	Run 20 m/s (2 x)**	0.131	0.133	0.002
	Run 20 m/s (4 x)	0.154	0.160	0.006
	All runs (6 x)	0.137	0.145	0.008

Table 4.2: *95 percentile positional error of without RTP aiding. The asterix notation * and ** indicate the two different combinations of runs sampled at a speed of 20 m/s.*

		95 percentile	Maximum value	Diff.
East				
	Run 11 m/s (2 x)	0.274	0.284	0.010
	Run 20 m/s (2 x)*	0.089	0.092	0.003
	Run 20 m/s (2 x)**	0.106	0.107	0.001
	Run 20 m/s (4 x)	0.095	0.098	0.003
	All runs (6 x)	0.108	0.111	0.003
North				
	Run 11 m/s (2 x)	0.030	0.033	0.003
	Run 20 m/s (2 x)*	0.090	0.092	0.002
	Run 20 m/s (2 x)**	0.073	0.075	0.002
	Run 20 m/s (4 x)	0.051	0.060	0.009
	All runs (6 x)	0.045	0.051	0.006
Down				
	Run 11 m/s (2 x)	0.028	0.039	0.011
	Run 20 m/s (2 x)*	0.163	0.164	0.001
	Run 20 m/s (2 x)**	0.124	0.125	0.001
	Run 20 m/s (4 x)	0.142	0.144	0.002
	All runs (6 x)	0.132	0.135	0.003

Table 4.3: *95 percentile positional error with applied RTP aiding. The asterix notation * and ** indicate the two different combinations of runs sampled at a speed of 20 m/s.*

4.6.4 Research question 3: BENEFITS OF EXCESSIVE PASSINGS

The last hypothesis assessed in this part includes a discussion concerning the number of runs necessary to obtain the best possible result by RTP aided positioning. Table 4.3 will be referred to in this section. Two are the minimum amount of runs necessary for utilizing the method of RTP. For a speed of 11 m/s only two runs are available for research, as opposed for 20 m/s, where four runs are sampled at this speed. A total of six distinct runs are available for further assessment. Odd number of runs have not been studied. According to the study from the even number of runs preformed, it is not expected that this would have an effect on the final conclusion.

The investigated benefits evident from Table 4.3 show that the North component shows an improvement in terms of a lower 95 percentile of true errors for a number of four and all six runs, as compared to the error of only two runs, for a speed of 20 m/s. For the North component anyway, a speed of 11 m/s provides an even lower error than the total of six runs provides. The same trend does not necessarily apply to the two other components. The differences between the 95 percentile are at the centimetre level.

Based on Table 4.3, the results provides no increased improvements of significance in terms of the absolute accuracy for the East and Down components. The time and cost of adding data will surpass the gain of adding more data above the located threshold.

As stated by the Fisher-information matrix, adding more measurements will always add information to the dataset. Hence including more information for excessive runs are expected to increase the accuracy, in terms of Fisher [Jekeli, 2001, 207]. However, the fact that additional data opposes the expected error behaviour further imply that the model of which it is based must be incorrect.

Supportive conclusions can be drawn by investigating the corresponding Table 4.2 for no RTP aiding.

The system model and errors will be treated in further depth in Part II and III.

4.6.5 Summary of Part I

The results of this chapter can be summarized by the following guide lines. The guide lines represent distinct recommendations based upon the results of the analysis of this chapter, and some further comments expressed below.

Guide Lines

- To preserve the highest possible quality estimate of the trajectory, time spent in the tunnel is confirmed to be of major importance. The less time the better due to shortening of GNSS outage. This would further imply a velocity as high as possible. No tie points or very few tie points are needed, when a high speed ensures a short duration through the tunnel. The highest possible speed is restricted by traffic limit regulations and possibly the lidar instrument specification.
  A speed of 20 m/s will work well.
- A high density of RTPs is not necessary for presumably shorter tunnels like the Lapplia tunnel, as long as a GNSS solution is available at each side of the tunnel. The amount of RTPs seems of less importance. In terms of projects similar to the Lapplia tunnel, a total of 10 – 20 evenly distributed tie points throughout the tunnel, depending on the tunnel length and the regulated speed limit, is seemingly adequate.
  The higher the allowed velocity, the fewer RTPs are needed. Note however, that the Down component reacts differently to an increase in speed as opposed to the North and East components.
- 20 or 10 tie points can easily be located and processed in a short amount of time, without the need of a costly production line.
- More than the minimum requirement of two runs does not increase the absolute accuracy when considering only aided by RTP, in addition to inertial sensor integration and odometer.
- Additionally, utilizing RTP may also capture sideways movements of the vehicle, in addition to odometer, but this has not been an object of research here.

Summary and future outline for RTP positional aiding The conclusions seem to state that the effect expected by utilizing of the position aiding by RTP might have been overrated in terms of the initial hypotheses, instead uncovering other parameters of higher importance.

The overarching motivation of this research is to study some alternatives to positional aiding not involving land surveying of adjustment point features, without the need of compromising on the accuracy level.

Being able to drive through a shorter tunnel at a speed of 20 m/s without the need of establishing a set of adjustment points inside the tunnel, is actually applicable to real projects. It may represent a real positive turnover in terms of surveys by the mobile mapping system (MMS). The accuracy obtained by a set-up similar to the research design of the Lapplia tunnel is passable for many smaller projects and will save valuable resources in terms of both time and financial costs. The relevance and importance of RTP in ensuring a consistent dataset still applies, as initially emphasized.

The original hypothesis may have been slightly overrated, but the results are by no means of any lesser importance. Having to survey adjustments points in every road project is both costly and ineffective. Reducing this factor is therefore desirable. This research show that this might be possible in some applications. A typical example is concerned with the cross-section calculations of the height and width of a tunnel, to confirm that large vehicles will be able to pass. This product can rely on accurate relative data referred to the tunnel interior only, hence not directly dependent on the global reference frame.

The research data in this study cannot answer for the achievable accuracy for longer tunnels, or ensure the application of these results to larger projects. In such cases, adjustments points may still be needed to provide the required accuracy of the trajectory estimates.

Chapter 5

Part II: Comparison of the Innfjorden navigation solutions

5.1 Introduction

A new tunnel is subject to research in this part. The dataset is sampled with an additional IMU also mounted to the Lynx MM vehicle. The Honeywell HG9900 is a higher grade IMU, kindly lent out to NMBU by the Norwegian Defence Research Establishment for the purpose of this thesis.

The different quality grade of the HG9900 and the LN200 would suggest that the resulting trajectory errors would be different also. HG9900 is characterized by high precision and accuracy. A sensor performance comparison of the HG9900 as opposed to LN200 is *not* of concern.

This part aims to investigate further the navigation solution, and possible errors affecting the measurements.

5.1.1 Error theory

Errors are always present in measurements [Ghilani, 2010, p.2]. True values of measurements are therefore never known, as they will never be perfectly exact. Since the true value is never known, the exact size of the errors is also unknown.

The accuracy is dependent on several factors [Ghilani, 2010, p.4]. Reliability, quality specification of equipment and environmental conditions are among the

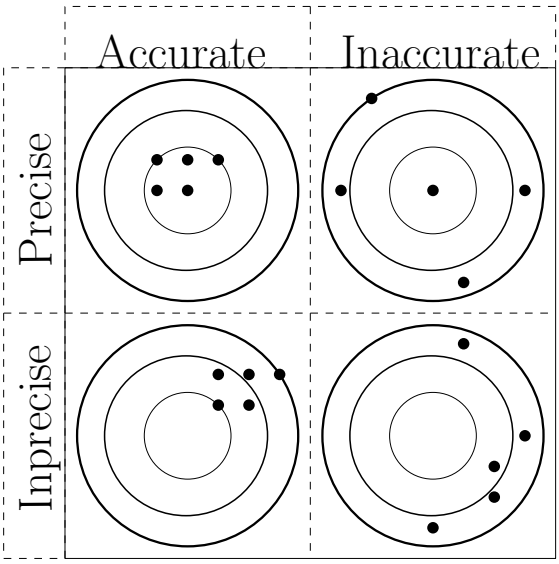

Figure 5.1: *Precision and accuracy.*

limitations worth considering. Definitions of precision and accuracy are given below.

Repeatability and precision Repeated measurements for the same studied object will, due to the presence of errors, result in inevitable discrepancies between the observed quantities [Ghilani, 2010, p.4]. Small discrepancies between the observations indicates small errors in the observing sensor, and vice versa. Such datasets are defined as precise, and are likely to be given higher credibility. [Ghilani, 2010] apply the following definition of precision:

> " Precision is the degree of consistency between observations and is based on the sizes of discrepancies in the data set. "

However, precise values are not necessarily accurate. Precision only verify the repeatability of observations. Hence repeatability is a property of the sensor, characterizing its quality.

Accuracy Accuracy on the other hand, implies how far the observation are located from the its true value [Ghilani, 2010, p.4]. As opposed to precision, the accuracy is never known explicitly. Since the true value is unknown, accuracy is also unknown.

5.2 Research design and field work

The tunnel being the object for research is located in Innfjorden, near the west-coast of Norway. The tunnel is roughly 6.5 km in length.
Four runs through the tunnel are performed. A reference trajectory based on land-surveyed adjustment points is only available for one out of the four tunnels.
The equipment is the same as for the Lapplia tunnel, though an extra IMU is added to the mounting. Specifications in terms of the IMU sensors are given in the subsection below.

The four respective runs for the Innfjorden tunnel correspond to the first and three last grey fields in Figure 5.2, as highlighted by the numbers 1 – 4. The grey areas represent missing GNSS observations. The average speed throughout the tunnel is 11 m/s. Corresponding GPS time for each run 1 – 4 equal the intervals [380820 – 381420], [387910 – 388470], [389650 – 390230] and [390780 – 391350]. GPS time is given as Time Of Week (TOW), in units of seconds.

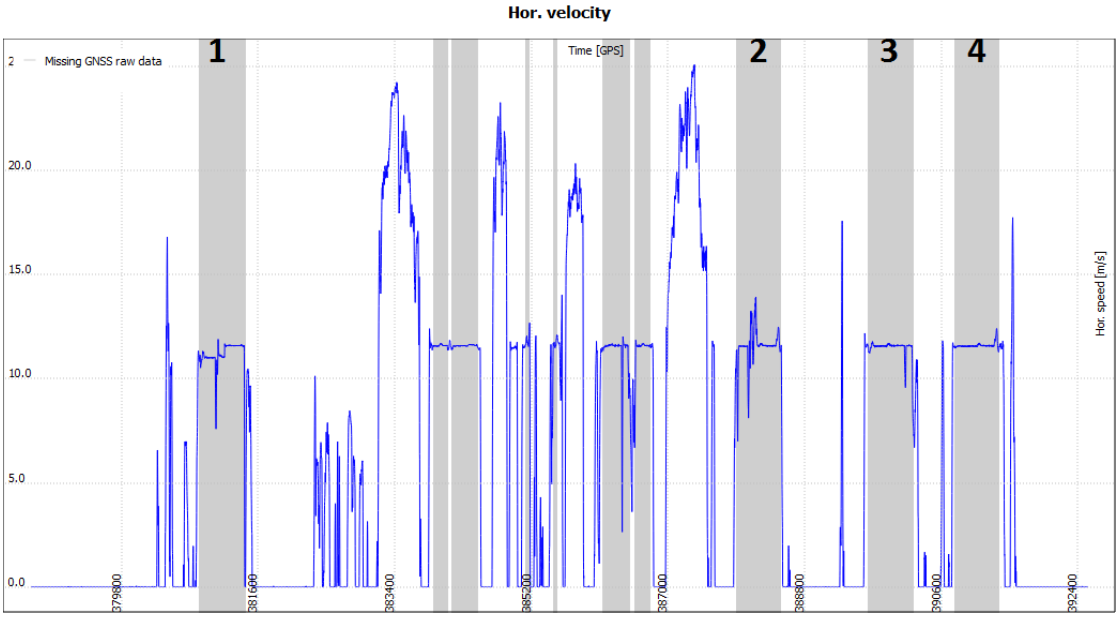

Figure 5.2: *The horizontal speed for data of the Innfjorden tunnel. The speed, corresponding to 11 m/s, is attempted kept constant throughout each run in tunnel.*

	Acc. bias ϵ [m-g]	Acc. misalign. [m-g]	Acc. scale [ppm]	Gyro A.R.W. [deg/$\sqrt{h}$]	Gyro misalign. [deg]	Gyro scale [deg]
Navigation Grade	0.025	0.05 deg	100	0.002	0.0018	0.0018
Tactical Grade	0.3	0.1 deg	350	0.07	0.0360	0.0360

Table 5.1: *Sensor quality parameter comparison given by Vectornav Technologies.*

5.2.1 Equipment

The original equipment mounted on the Lynx MM, is described in the initial introduction. An additional IMU, the Honeywell HG9900, has been mounted on to the platform for the sampling of the following dataset. Other than the vehicle and its platform mounted sensors, observations from a GNSS base station data are also used.

Mounting of IMU sensors: LN-200 and HG9900

The HG9900 is a higher grade IMU than the LN200. Due to the large difference in performance between the two IMUs, the navigation solution for the HG9900 is expected to be of better quality than the resulting solution with the LN200, naturally.

IMU classification Difference in price and performance usually distinguish between higher and lower grade inertial sensors on the marked, yet there exists no absolute standard for classifications of IMU sensors.

The grouping by performance grade of IMU sensors are given in Table 5.2. The classification follows the standard given by Vectornav Tecnologies[1].

Typical performance in terms of horizontal positioning provided by each group are given in more depth in the Vectornav reference.

The LN200 performance corresponds to the Tactical grade in Table 5.1, while the HG9900 to the higher Navigation grade.

[1]About IMU sensors, by Vectornav Technologies. Dallas, Texas (USA). URL: *http //www.vectornav.com/support/library/imu − and − ins* [Downloaded 2015-03-29]

Performance group	Description
Marine/Navigation Grade	Marine grade technology sensors are the highest possible commercial INS available, providing the best overall performance. Navigation grade, such as are used in commercial and military air-crafts, have a similar, though slightly lower performance.
Tactical Grade	Represents a quality defined between the Navigation and Industrial grade.
Industrial Grade	Industrial grade sensors are a calibrated Automotive system.
Automotive/Commercial Grade	Automotive grade represent the lowest grade. They provide good repeatability, but are not accurate enough for required navigation performance. Other applications.

Table 5.2: *IMU performance categories overview given by Vectornav Technologies.*

LN200

The LN200 IMU used in the Applanix POS LV 420 system is the original instrument used for the Lynx MMS platform mounting. Its resulting performance suggests a tactical grade quality IMU. Specifications for the sensors are given in the manual[2] provided by the manufacturer. A selection of defining parameters are summarized in Table 5.3.

[2]URL: *http* : *//www.northropgrumman.com/Capabilities/LN*200*FOG/Documents/ln*200*.pdf* [Downloaded 2015-03-03]

Sensor	Parameter	Value
Accelerometers		
	Bias Repeatability (1 σ)	300 μg - 3000 μg
	Scale Factor Accuracy (1 σ)	300 - 5000 PPM
Gyros		
	Bias Repeatability (1 σ)	1 - 3 deg/h
	Scale Factor Accuracy(1 σ)	100 - 500 PPM
	Angular Random Walk (PSD)	0.07 - 0.15 $deg/\sqrt{h}$

Table 5.3: *Specifications for the LN200 IMU.*

Sensor	Parameter	Value
Accelerometers		
	Bias Repeatability (1 σ)	< 25 μg
	Scale Factor Accuracy (1 σ)	< 100 PPM
Gyros		
	Bias Repeatability (1 σ)	< 0.003 deg/h
	Scale Factor Accuracy (1 σ)	< 5.0 PPM
	Angular Random Walk (PSD)	< 0.002 $deg/\sqrt{h}$

Table 5.4: *Specifications for the Honeywell HG9900 IMU.*

Honeywell HG-9900

The Honeywell HG9900 is an example of a navigation grade IMU. The HG9900 is considered a state-of-the art IMU sensor for inertial navigation, initially developed for aerospace applications. The gyro and accelerometer performance are provided by the manufacturer[3]. A table of system specifications is rendered below.

5.2.2 Static GNSS base station data

The ETPOS service provided by The Norwegian Mapping Authorities serves users in need of precise position data or corrections of GNSS measurements in retrospect. The service consists of a net of geodetic base stations distributed all over Norway, providing continuous series of static GNSS observation data.

ETPOS data for the date 2015-02-26 from the Innfjorden base station was ordered, at a 1 second data rate.

[3]URL: *http : //www51.honeywell.com/aero/common/documents/myaerospacecatalog − documents/MilitaryAC/HG9900_IMU.pdf* [Downloaded 2015-03-03]

Figure 5.3: *Map overview and coordinates of location for the Innfjorden base station. URL: http://gammel.norgeskart.no [Downloaded 2015-03-13]*

5.3 Field work for Innfjorden using HG9900 and LN200

Post-processing of the land-surveyed data is run in TerraPos. The navigation solution are processed in tightly coupled (TC) mode. Solutions are exported as text files, to be imported in MATLAB. The exported data contains three-dimensional coordinates of Easting, Northing and ellipsoidal height, at corresponding GPS time events. Time events are given as TOW in seconds. Standard deviation of position is included for the coordinates in the export data.

MATLAB is utilized for computation of height differences relative to the reference trajectory. Properties of the sampled Innfjorden dataset prevent straight forward computation of true errors.

The MATLAB computed outputs are subject to further analysis and discussion. An additional outlook to Part III rounds up this section.

Generating the reference trajectory

A reference trajectory is needed for computation of the true errors. Only the third run for TOW interval [389650 – 390230] contains dense land-surveyed adjustment points. For this run, an XML-file of land-surveyed adjustment points is included in the processing as external aiding to the INS.

Generally, an error is defined as the computed residual ϵ between a measured value y and its true value μ, given in [Ghilani, 2010, p.3] as

$$\epsilon \ = \ y - \mu \tag{5.1}$$

The true value is never known. But if assuming a significantly accurate solution, this can be regarded as a reasonable reference.

By including all aiding information available, the obtained uncertainty of the solution is only at a few centimetre. Compared to the non-aided solution, i.e. without external aiding by base station data and GCP positioning, the relative accuracy is significant enough to be regarded as the true reference.

Since the reference trajectory is assumed to be the truth, it must be free of errors. The discrepancy obtained by computing the difference between the reference and the test quantity represents the true error in the test.

Spatial comparison of the navigation solutions

A complete coverage of adjustments points for all four runs would provide the true errors for the entire trajectory. Since this is not available, the errors can not be compared as a function of time. The length of the tunnel is however equal for all four runs.

Strategy for MATLAB computation To come up with the plotted navigation solutions, as a function of displacement inside the tunnel, the following steps are performed. The steps are implemented in MATLAB.

Exported navigation solutions from TerraPos are imported in MATLAB. The three solutions are the reference trajectory containing the external adjustment point aiding, in addition to one solution for each IMU respectively, without GCP aiding.

A distance vector d is calculated, containing the relative distances of i number of points, from a starting point (i=0) at one end of the tunnel. This point is defined as the arbitrarily chosen initial point P_0. The (i-1) number of relative distances through the tunnel will refer to this point.
P_0 is defined by the plane coordinates in the navigation frame (g-frame): $E_0,\ N_0$.

$$d = \sqrt{(N_i \ - \ N_0)^2 \ + \ (E_i \ - \ E_0)^2} \tag{5.2}$$

The ellipsoidal height h will be plotted as a function of relative distance from P_0.

The heights and distances for the HG9900 and the LN200 trajectories must be interpolated with the heights and distances for the reference trajectory. For this, the in-built function of INTERP1.M in MATLAB is utilized. A linear interpolation is used. The following height difference Δh are generated

$$\Delta h = h \; - \; \tilde{h} \tag{5.3}$$

for the observed heights h and interpolated reference heights $\tilde{h}$.

The differences Δh are plotted as a function of d given in Figure 5.5 and 5.6 for each IMU, in the following section.

5.4 Analysis of results

The reference solution of heights in run no.3, plotted against the relative differences from P_0 is provided in Figure 5.4. The interpolated heights and distances for the HG9900 and LN200 navigation solutions are based on this reference. The interpolation is linear.

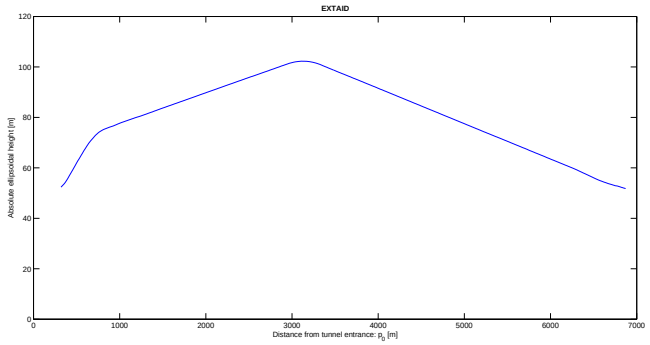

Figure 5.4: *Reference trajectory of third run as function of relative distance from* P_0.

The expected quality for the solution, given as true errors, is by an educated guess about a few decimetres.
For the navigation solution, the mounted odometer is aiding the along-track motion in. Throughout the tunnel, the height difference vary over the range of 50 – 100 m of ellipsoidal height over a distance of 6.5 km. As the tunnel passage follow a straight line through the topographic masses the dosage of the road through the tunnel is insignificant. Hence the error-sources affecting the along- and across-track components of the platform frame especially are more less and more limited.

5.4.1 Results

The results of the navigation solution, plotted for true error of height generated by the HG9900 and LN200 data, are provided in Figure 5.5 and 5.6.

Each graph in the two plots represent a run from the dataset. The total amount of runs provided are four. Each run is plotted by means of the relative distance from the tunnel entrance, defined by P_0. Hence every plotted point on the graph is referred to the same location relative to the tunnel regardless of which way the vehicle is heading. Note that it will not be the exact same location, as the points are interpolated using the common reference generated from the third run.

5.4.2 Analysis of navigation errors

True errors height for the LN200 navigation solution The graphs representing the true errors of height, relative to the four runs sampled by the LN200 are spread apart. There is no consistent agreement between the height errors for each run. Based on the plotted solutions, the LN200 can be said to provide a low degree of precision, as the repeatability is less consistent.

True errors height for the HG9900 navigation solution The graphs representing the true errors of height, relative to the four runs sampled by the HG9900 show a much higher degree of precision. The solutions lie relatively closer to each other, hence each run quite well repeat the same solution as the other runs.

Discussion

Both plots deviate from zero. Assuming no errors and perfectly synchronized datasets, the differences would be zero. No measurement is ever perfectly free of errors, and some deviation from zero is expected. The aim in every survey is to mitigate the errors as much as possible.

The largest height differences are registered in the middle of the tunnel, corresponding to the centre of the plots. The largest height error is roughly 2 meters for the LN200 solution, and correspondingly 3 meters for the HG9900 solution, in absolute terms.

The plot of HG9900 solutions shows a more consistent trend for the distribution of errors, as compared to the LN200 solution. The consistent systematic trend implies that an external error may not be compensated for in the model.

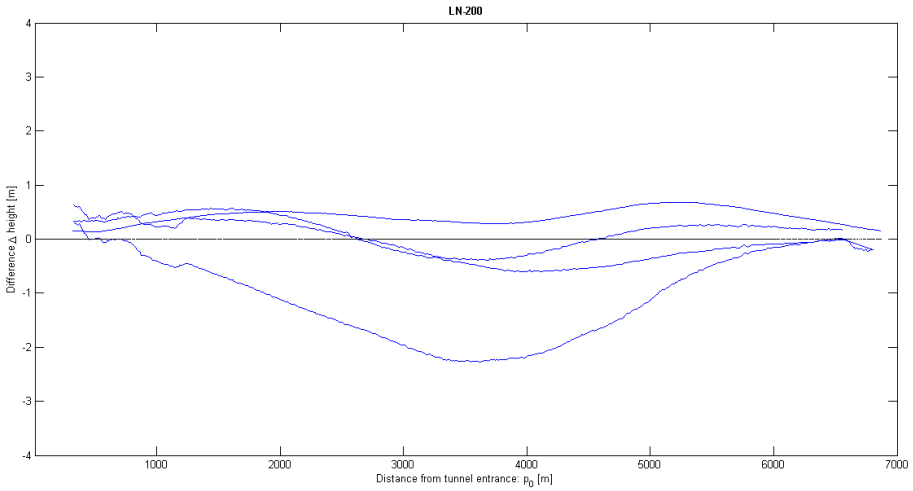

Figure 5.5: *True errors between measured height and interpolated height with ground truth trajectory for LN200, plotted as a function of distance from the tunnel entrance.*

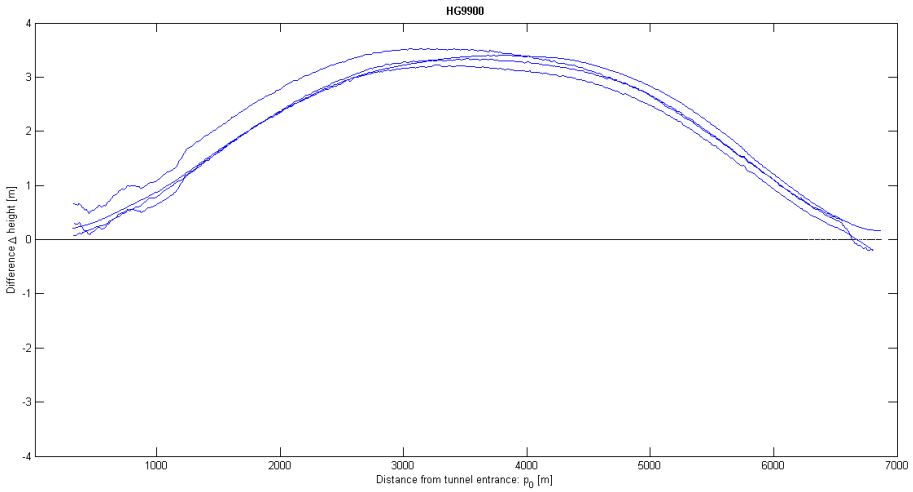

Figure 5.6: *True errors between measured height and interpolated height with ground truth trajectory for HG9900, plotted as a function of distance from the tunnel entrance.*

The solution by LN200 is not as one-sided as the HG9900 solution. The same systematic trend can be derived from the LN200 solution also, but the trend is not as evident here as it is in the HG9900 solution.

Systematic errors In the case of unmodeled systematic errors, a higher grade IMU will not provide better accuracy, as is evident from the results shown in Figure 5.5 and 5.6. The errors still affect the navigation solution so that the height from the solutions differs from the reference, i.e. actual trajectory of the vehicle.

5.4.3 Summary of Part II

The study in Part II has shown that there may be systematic errors caused by external effects not being compensated for in the error modeling. The HG9900 solution suggests this by high degree of precision and accuracy. The systematic errors are also evident in the LN200 solution, but the results show a low level of repeatability and has a more ambiguous trend. From the LN200 height errors alone, any designated clear source of error is not evident. The LN200 is not precise enough to nominate any systematic trends based on the results like the HG9900 is able to.

Outlook to Part III In Part III, the evident systematic trend uncovered above will be further investigated.
As stated, the error is largest in the middle of the tunnel. Considering the topography above the tunnel, the largest masses for the Innfjorden tunnel are also gathered in above the middle of the tunnel. Hence the gravitational attraction of the masses overhead can be further assumed to cause an effect on the measurement.

The free-air reduction of masses usually employed with the normal gravity compensation is typically assumed adequate. The topography in this data set seems to challenge this assumption.

Chapter 6

Part III: Studying systematic errors in the Innfjorden data

6.1 Introduction

Part III is based on the field work and dataset from the Innfjorden tunnel, similar to Part II. The research in Part II uncovered some unexpected trends implicating possible unmodeled systematic errors in the navigation solutions. This is investigated further in this part.

In Part II, the analysis of the navigation solution based in the LN200 IMU resulted in larger amount of random errors than for the solution by HG9900. The repeatability of HG9900 is very good. For the LN200, the opposite is true. Due to this, no significant trend caused by systematic errors could be derived from the LN200 plot in Figure 5.5. For the higher level HG9900 IMU, implications of unmodeled systematic effects affecting the vertical positioning were clearly visible in Figure 5.6. Recall that the HG9900 is both more precise and accurate, as compared to the LN200.

Tunnels are generally a result of large topographical masses representing an obstacle for logistics. This is especially true for the tunnels in the coastal landscape in the western part of Norway, with the deep fjords and the steep mountains. Tunnels can also protect passing traffic from events like landslides or avalanches in this hazardous landscape. That said, tunnels can be just as well on land as below sea level. For the purpose of this thesis, only on-land tunnels are considered.
Further relevant parameters for concern are the length of the tunnel and the size of the surrounding masses.

This part will calculate the approximate effect the topographic masses have on the vertical position and velocity for an arbitrarily point inside the tunnel.

The theory by Newton, concerning gravitational attraction between masses, and terrain reduction by Bouger plate are particularly of interest for this section.

The emphasized theory of this chapter is based primarily on the reference literature on physical geodesy provided by [Hofmann-Wellenhof and Moritz, 2006].

6.1.1 Gravity and gravitational force

Newtons's law of gravitation explain the attracting force F between two points of mass m_1 and m_2, separated by a distance l, given as

$$F = G\frac{m_1 m_2}{l^2}, \tag{6.1}$$

where G is Newton's gravitational constant given in SI units as

$$G = 6.6742 \cdot 10^{-11} m^3 kg^{-1} s^{-2}. \tag{6.2}$$

The geoid is the equipotential surface of the true gravity field [Hofmann-Wellenhof and Moritz, 2006, p.65], denoted W. The gravity vector g is given as the gradient vector of W, by direction downwards along the plumb line and magnitude defined as gravity. Gravity in relation to heights, become the negative vertical gradient, as given by

$$dW = -gdH \;\Leftrightarrow\; g = -\frac{\partial W}{\partial H} \tag{6.3}$$

The measured gravity g is an acceleration, referred to in units of gal or mgal. Gravity by [Hofmann-Wellenhof and Moritz, 2006, p.43], is the combined effect of gravitational and rotational force, acting on a unit of mass at rest at the Earth's surface.

The level ellipsoid is assumed to be the normal form of the geoid. The ellipsoid represents an equipotential surface of the normal gravity field, as if all masses of the earth were supposedly fitted inside the surface and no topography would deviate from the surrounding ellipsoidal surface.

The potential of the normal gravity field is denoted U. The distance between the geoid and the ellipsoid is known as the geoidal height [Hofmann-Wellenhof and Moritz, 2006, p.91].

Dirichlet's principle states that the gravitational potential on the outside of a surface is completely determined by its geometrical shape and potential value [Hofmann-Wellenhof and Moritz, 2006, p.65]. The potential U for the normal gravity field is defined only by its ellipsoidal shape, its mass, and its angular velocity due to its rotation.

6.1.2 Normal gravity

The normal gravity vector γ is given by definition as the gradient of the potential

$$\gamma = \text{grad U},$$

and represents the total gravity on the level ellipsoid [Hofmann-Wellenhof and Moritz, 2006, 69].

The normal gravity γ_h is the gravity with a ellipsoidal height h above the level ellipsoid of the normal gravity field with potential U, and is defined as follows

$$\gamma_h \;=\; \gamma \;+\frac{\partial\gamma}{\partial h}h+\frac{\partial^2\gamma}{\partial h^2}h^2 \;+\; \cdots - \tag{6.4}$$

At the ellipsoid $h = 0$. γ as well as the derivatives are referred to the ellipsoid. The first derivative $\partial\gamma/\partial h$ can be approximated by the use of Brun's formula [Hofmann-Wellenhof and Moritz, 2006, p.81].

Brun's formula relates the physical associated vertical gradient of gravity ∂g/∂H to the geometrically defined level surface of mean curvature, a concept of major importance in the field of geodesy [Hofmann-Wellenhof and Moritz, 2006, 51]. For the reference ellipsoid of the normal gravity field, the vertical gradient

$$\frac{\partial\gamma}{\partial h} \;=\; 2\gamma J \;-\; 2\omega^2 \tag{6.5}$$

for ellipsoidal height h, when assumed outside of the mass and density $\rho = 0$. The definition of mean curvature J of the ellipsoid is in [Hofmann-Wellenhof and Moritz, 2006, p.72] given as

$$J = \frac{1}{2}\,(\frac{1}{M}+\frac{1}{N})\;,$$

for M and N being the meridian and normal radius curvatures respectively, as defined in general ellipsoidal geometry.

Inserted, this gives [Hofmann-Wellenhof and Moritz, 2006, p.82]

$$\frac{\partial\gamma}{\partial h} \;=\; -\gamma\,(\frac{1}{M}+\frac{1}{N}) \;-\; 2\omega^2\;. \tag{6.6}$$

More about normal gravity definitions in [Hofmann-Wellenhof and Moritz, 2006].

Normal gravity vector

The earth ellipsoid deviates slightly from a sphere, and the normal gravity are assumed sufficient [Kjørsvik, 2010, p.13] in many applications. The following equations originate from [Hofmann-Wellenhof and Moritz, 2006, Sect.2.10], unless otherwise is stated.

The vertical component of gravity referred to the level ellipsoid [Hofmann-Wellenhof and Moritz, 2006, Eqn.(2-199), p.80] is given as

$$\gamma = \gamma_a(1 + f_2 sin^2\phi + f_4 sin^4\phi) \ , \tag{6.7}$$

for

$$f_2 = -f + \frac{5}{2}m + \frac{1}{2}f^2 - \frac{26}{7}fm + \frac{15}{4}m^2 \tag{6.8}$$

$$f_4 = -\frac{1}{2}f^2 + \frac{5}{2}fm \tag{6.9}$$

The normal gravity at ellipsoid height h is further given

$$\gamma(h) = \gamma\left[1 - \frac{2}{a}(1 + f + m - 2f sin^2\phi)h + \frac{3}{a^2}h^2\right] \tag{6.10}$$

γ_a, f and m are constant quantities for the ellipsoid, as derived in [Hofmann-Wellenhof and Moritz, 2006, Sect.2.10].
h further denote ellipsoidal height, while a is the semi-major axis of the ellipsoid.

For the reference ellipsoid model, the gravity γ along a equatorial parallel circle is constant. The normal gravity is therefore invariant in terms of longitude λ, and hence only dependent on the latitude ϕ [Farrell, 2008, pp.32–33]. The small effect due to the latitude can be studied as the North-South component γ_N, given as

$$\gamma_N = -\frac{f_2 + f_4}{R_e} h \sin 2\phi \tag{6.11}$$

in [Hofmann-Wellenhof and Moritz, 2006, p.233], for R_e being the radius of Earth.

The normal gravity vector expressed in the NED navigation frame (g-frame) is provided in [Jekeli, 2001, p.189]

$$\gamma = (\gamma_N + \gamma_D)^T \tag{6.12}$$

for the normal gravity of the Down component, when $\gamma(\phi, h)$ is given in Equation 6.10,

$$-\gamma_D \approx \gamma(\phi, h) \tag{6.13}$$

6.2 Gravity reduction methods

The concern of gravity reduction and gravity reduction methods are how to manage the masses between the topography of the actual earth and the corresponding reference surface of either gravity g or normal gravity γ. The method depends on the application or motivation for performing topographic reduction. The theory of gravity reductions is derived in [Hofmann-Wellenhof and Moritz, 2006, Ch.3].

For this, auxiliary geometrical shapes and formulas can assist the computation of the potential and vertical attraction of masses. The attraction is the negative derivative of the potential with respect to the height.

Knowledge of mass density above the geoid is necessary in all reduction methods [Hofmann-Wellenhof and Moritz, 2006, p.293]. Since measurements are sampled on the surface of the Earth, the standard density is considered a reasonable assumption. The standard density is given as

$$2.67 \ g \ cm^3 \quad .$$

Gravity g refers to the physical surface of the Earth, while the normal gravity γ refer to the mathematical ellipsoid [Hofmann-Wellenhof and Moritz, 2006, p.129]. For a gravity reduction to the geoid, the gradient $\partial g/\partial H$ is needed [Hofmann-Wellenhof and Moritz, 2006, p.134].

6.2.1 Free-air reduction

The free-air reduction to the geoid is given as [Hofmann-Wellenhof and Moritz, 2006, p.134]

$$F = -\frac{\partial g}{\partial H} H \tag{6.14}$$

By "free-air" it is assumed no masses between the height at P and the reference surface below. As there are actual masses above the geoid, the "free-air" assumption imply that this have been removed prior to the reduction [Hofmann-Wellenhof and Moritz, 2006, p.134].

For the free-air gravity gradient, the assumption that " the actual free-air reduction is assumed to be equal to the normal gradient. " [Hofmann-Wellenhof and Moritz, 2006, p.293].

$$\frac{\partial \gamma}{\partial h} \doteq -0.3086 \quad mgal \ m^{-1}. \tag{6.15}$$

Assumptions of free-air reduction of normal gravity

Figure 6.1 consider the consequences of the assumption of the free-air reduction, for the height above the ellipsoid in the two situations: A and B.

Position A have no topographic masses above its location. The quantity h denote the vertical A's height above the ellipsoid. The net gravitational attraction affecting A are therefore distributed between the ellipsoid and the vehicle. Since h is small, e.g. typically at ∼10-40 m, and the speed is low, a *free air reduction* is assumed an appropriate approximation to the gravity reduction.

The situation for B is different. B has the same speed and ellipsoidal height as A, but has entered a tunnel. Hence a large topographic mass is located above B, as opposed to no masses above in terms of A.

$$H_{top} >> h_{ell}$$

This means that the amount of overhanging masses have abruptly changed from zero to several hundred meters.

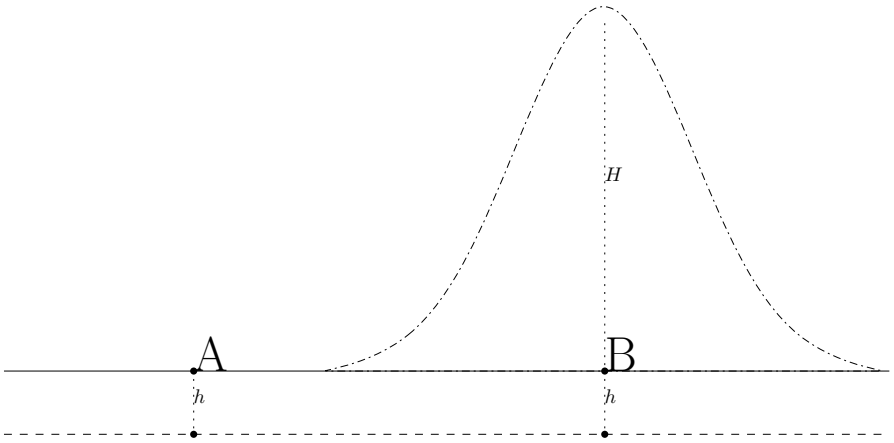

Figure 6.1: *Free-air assumption related to topographic mass distribution: A and B denotes the vehicle's position.*

As in the case of the Innfjorden tunnel, the maximum height H reaches 800 m. This is significantly larger than the quantity of h.

6.2.2 Bouger reduction

The Bouger reduction of gravity seeks an approach for complete removal of the masses above the geoid [Hofmann-Wellenhof and Moritz, 2006, p.135].

Bouger further assumes a completely flat area, and a mass of uniform, constant density ρ. When considering the horizontal extent approaches infinity (∞) the plate may be regarded as a cylinder, with an equal radius in all directions. The attraction for the Bouger plate is then derived

$$A_B \;=\; 2\pi g \rho H \;, \tag{6.16}$$

for H measured in meters. Subtracting this quantity from the observed gravity results in computation of the *incomplete Bouger reduction*. To obtain the complete Bouger reduction, a combined process of removing masses and applying the previously derived free-air reduction is necessary [Hofmann-Wellenhof and Moritz, 2006, p.135].

The Bouger gravity g_B refers to the geoid. The Bouger anomalies are obtained by subtracting the normal gravity γ

$$\Delta g_B \;=\; g_B - \gamma \;. \tag{6.17}$$

The Bouger plate reduction may be further refined by applying additional terrain corrections. See [Hofmann-Wellenhof and Moritz, 2006, Ch.3, 135-138] for more.

6.3 Computation and analysis of Bouger plate reduction of topographic masses

This section follows a step-wise approach. In the first step, a simplified model for an approximation of the terrain is derived. The model should represent the mass of the topography, but be explained by geometric relations in mathematical terms.

Secondly, an implementation of the model into MATLAB follows, enabling the calculations in numerical terms. The resulting quantity $\delta\tilde{g}$ equals the total contribution of the surrounding masses.

The third step derives a numerical calculation of position error for a point P located in the middle of the tunnel.

Lastly, TerraPos is used to uncover the accumulated position error, by processing the forward-only solution of the trajectory. This is performed by disabling

the smoothing of the final processed solution, which otherwise would mitigate the effect by this error. A second forward-only solution utilizes a Digital Elevation Model (DEM). The differences are given the main attention. The results from TerraPos are seen in relation to the approximated estimate by the former computation steps.

The first dataset from Part I for the Lapplia tunnel is also processed as a forward-only solution. This is done to check if any similar results are evident in the measurements of this area. Results for Lapplia are presented in the end of this section.

6.3.1 Model for approximation by Bouger plate

For the shape of the mass surrounding P, two cylinders of finite radius and height are assumed. In other words, one cylinder for the mass above P and one for the mass between P and the reference ellipsoid. The standard density $\rho = 2.67$ is used to compute the amount of mass for each of the two cylinder volumes. Recall that P is located at height h above the ellipsoid in the middle of the tunnel, with an amount of topographic mass of vertical height H above.
Combined, the masses of the two cylinder models are assumed to be representable for total net effect of the vertical component of gravitational acceleration at P. For the conducted quantitative computations in MATLAB, refer to the subsequent section.

Fitting the mass distribution model

The cylinder parameters are defined by means of encapsulating the mass of the actual surface topography inside its geometrical bounded surface. Put differently, the radius and height are scaled to approximate the topographic masses defined at the surface, as if they where shaped as cylinders.

Figure 6.2 shows the height profile for a cross-section of the surface topography variations strictly above the Innfjorden tunnel. The height profile is rendered in the web-application available on *www.norgeskart.no*.

Figure 6.3 shows the related Bouger cylinder model approach, as outlined above. The assumed vertical height for P to surface is given as H, while h corresponds to the ellipsoidal height.

Figure 6.4 and 6.5 attempt to visualize the cylinder approach as seen from above. The contours of the two cylinders of unequal radius are implied by black circles,

relative to the background map of the Innfjorden tunnel in Figure 6.4.

Figure 6.5 is included to clarify the relation between the contour circles. The outer cylinder, representing the topographic mass between P and the ellipsoid, has the largest radius. Hence the innermost contour circle represents the model of the topographic mass above P, having a smaller radius.

6.3.2 MATLAB computations of Bouger-approximation

MATLAB has been used to compute the gravity accelerations δg_B of the Bouger cylinder models. For the computations the following parameters for the cylinders are chosen. Recall point P as being defined in the middle of the tunnel, between the two cylinders.
Parameters used for each cylinder for the purpose of computation are summarized in Table 6.1 below.

	δg_B [mgal]	Symbol	Radius [m]	Symbol	Height [m]
Top cylinder	72.32335	r_t	2000	H	800
Lower cylinder	3.69583	r_e	3000	h	33
Combined net g_B	68.62750				

Table 6.1: *Table of quantities for computed net Bouger model contribution, as the subtracted sum of each contribution on top and below, given by their respective model parameters of radius and height.*

The ellipsoidal height of P is based on an arithmetic mean of the surveyed heights of all adjustment points inside the tunnel. The coordinates of the adjustment points are also used in the processing of the reference trajectory in TerraPos.

In addition to the mean value, the minimum and maximum values are also extracted from the height data. This is summarized in Table 6.2. The range of surveyed heights is about 50 m between the lowest and the highest. The mean value of δg_B from the MATLAB computations is considered representative for the arbitrary point P in the following analysis. P is located in the middle of the tunnel, consistent with the depicted cylinder models in Figure 6.3 – 6.5.

The final position error is found by double integration of the gravity acceleration as a function of total time of a run through the tunnel. The next section will derive the equations to compute the net accumulated position error caused by neglecting the attractions of surrounding topographic masses. For the final numerical computations, the net gravitational acceleration δg_B equal to 68.62750 mgal will be used. The quantity refers to Table 6.1.

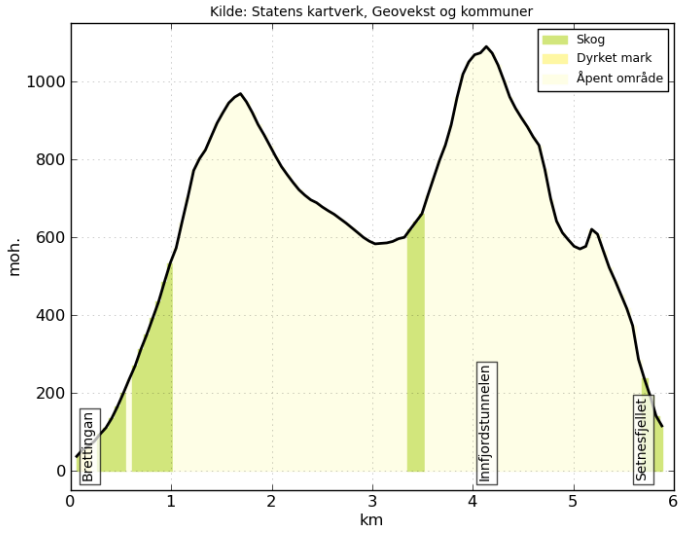

Figure 6.2: *Height profile of the Innfjorden tunnel (www.norgeskart.no).*

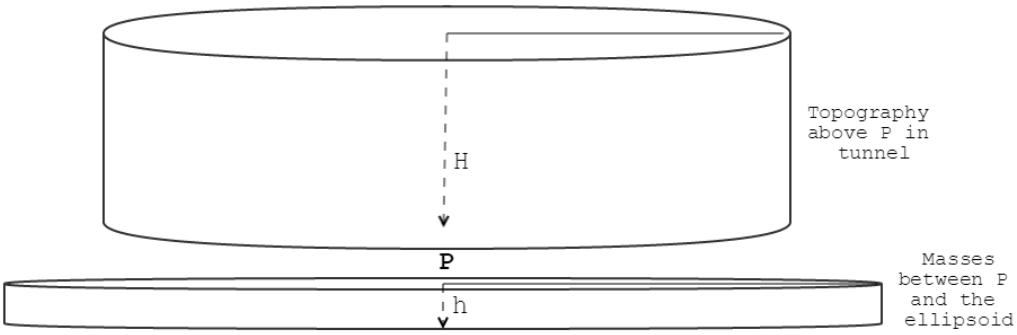

Figure 6.3: *Bouger cylinder models representing the topographic masses above and below P, with corresponding heights H and h, as viewed from the side.*

Figure 6.4: *Cylinder model fit to the surface topography.*

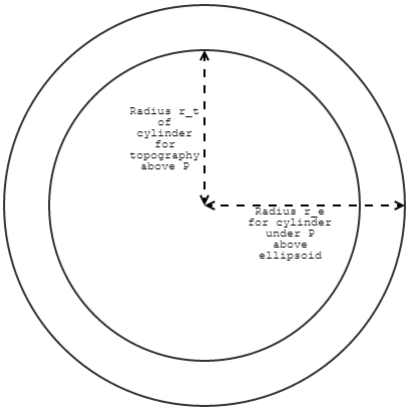

Figure 6.5: *Overlay of cylinder models with corresponding radii, as seen from top view.*

	δg_B [mgal]	Height [m]
P_{min}	0.45741	4
P_{max}	6.11438	55
P_{mean}	3.69583	33

Table 6.2: *Resulting gravity acceleration δg_B for different ellipsoidal heights h.*

6.3.3 Computation of position error by numerical integration

By exploiting the integrative relations between acceleration, velocity and position, an estimate of the total accumulated error can be quantified, i.e. double integration of acceleration return position.
The previous Bouger reduction computations in MATLAB resulted in a representative net gravity acceleration δg_B. This quantity is now renamed the gravitation acceleration error $\delta\tilde{g}$. It represents the error due to unmodeled masses of topography for P inside the tunnel. Additionally, the total time Δt for a run is known from the dataset. A run represents one passing through the tunnel, equal to the amount of time with missing GNSS data.
If a numerical equation for the kinematics can be found, expressed only by the known quantities $\delta\tilde{g}$ and Δt, an approximation of the position error can be derived numerically. The primary aim is an indication of the magnitude of the systematic error evident from the conclusions from Part II.

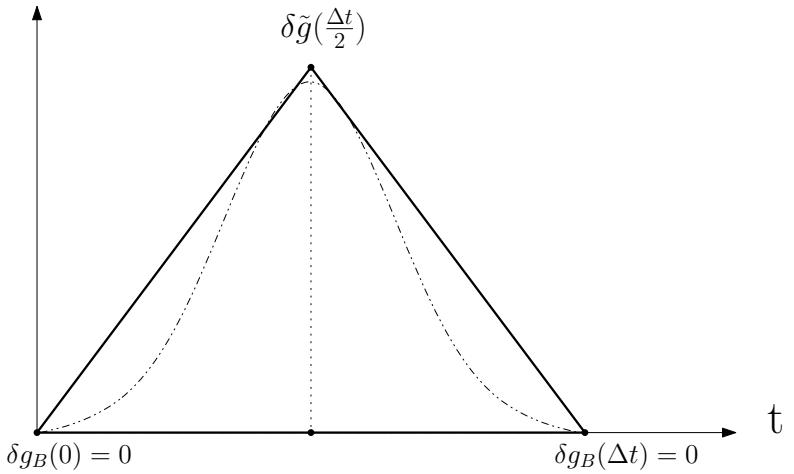

Figure 6.6: *An approximation for the terrain topography assumes a triangle model fit. A tunnel run lasts from t=0 to t=Δt. At these two events, the gravity perturbation $\delta\tilde{g}(t)$ equals 0. The largest position error are assumed in the middle of the tunnel, furthest away from each end of the tunnel, as represented by $\delta\tilde{g}$ at t=$\frac{\Delta t}{2}$.*
The midpoint $\delta(\tilde{g}\frac{\Delta t}{2})$ corresponds to the computed quantity of $\approx$ 68 mgal given in Table 6.1.

Figure 6.6 illustrates the triangle model representing the gravitational perturbing acceleration error $\delta\tilde{g}$ as a function of time. The largest value of $\delta\tilde{g}$ is located where the masses above P are largest. For the topography having the distributive shape similar to the indicated bell-shape in the illustration, this occur at t=$\Delta t/2$.
The quantity $\delta\tilde{g}(\Delta t/2)$ is integrated by the derived steps of integration given in Equations 6.18 – 6.20, providing the final accumulated position error estimate.

The single integrated acceleration error $\delta\tilde{g}(\Delta t/2)$ results in δv, representing the velocity error as a second order function of time *t*. The midpoint of this curve represents the velocity error accumulated for the largest acceleration error $\delta\tilde{g}$ at half the run time. If considering integration as a summation of trapezoids, a symmetry about the midpoint is observed. If approximated by a trapezoid, the total area under the second order curve to the left of the midpoint will tend to *overestimate* the integrated velocity error, while the interval on the right will *underestimate* by the same amount due to the symmetry. The summation based on the midpoint symmetry derives Equation 6.19 for the velocity error for t in range [0, Δt].

Further integration of the velocity error $\delta v(t)$ gives a function for the position error $\delta p(t)$, a third order function of time *t*. The final position error, accumulated for the total time span of one run is equal to $\delta p(\Delta t)$. The total position error by Equation 6.20 are expressed only in terms of the known quantities of $\delta\tilde{g}$ and

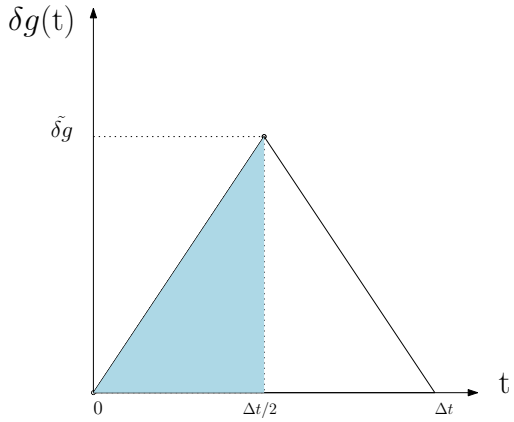

Figure 6.7: *Triangle model of largest gravitational acceleration error.*

$$\begin{aligned} \delta g\left(\frac{\Delta t}{2}\right) &= \delta\tilde{g} \\ \delta g(\Delta t) &= \frac{\delta\tilde{g}\cdot\Delta t}{2} \end{aligned} \tag{6.18}$$

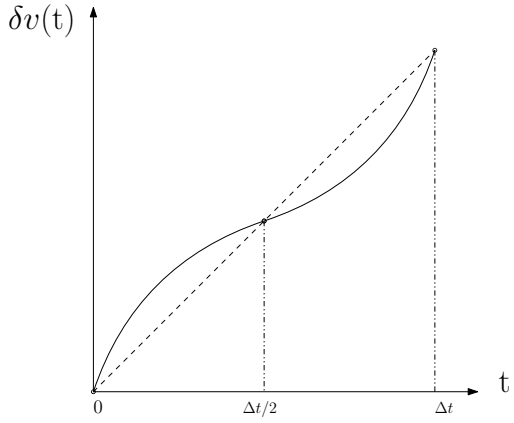

Figure 6.8: *Velocity error as the integrated gravitational acceleration error.*

$$\begin{aligned} \delta v\left(\frac{\Delta t}{2}\right) &= \frac{\delta\tilde{g}\ \cdot\left(\frac{\Delta t}{2}\right)}{2} \\ &= \frac{\delta\tilde{g}\Delta t}{4} \\ \delta v(\Delta t) &= 2\cdot\delta v\left(\frac{\Delta t}{2}\right) \\ &= \frac{\delta\tilde{g}\Delta t}{2} \end{aligned} \tag{6.19}$$

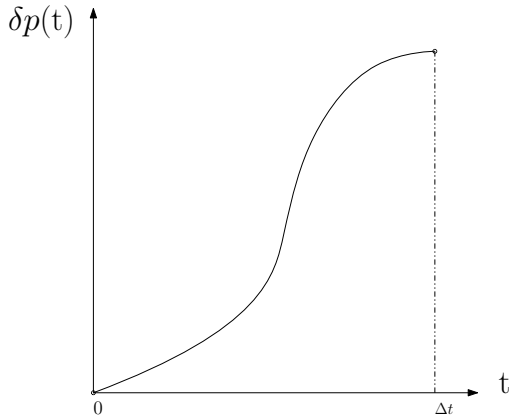

Figure 6.9: *Accumulated position error as the double integrated gravitational acceleration error.*

$$\begin{aligned} \delta p(\Delta t) &\approx \delta v\left(\frac{\Delta t}{2}\right)\cdot\Delta t \\ &= \left(\frac{\delta\tilde{g}\cdot\Delta t}{2}\right)\cdot\Delta t \end{aligned} \tag{6.20}$$

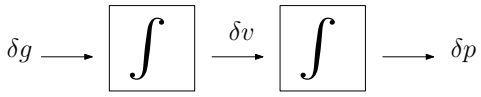

Figure 6.10: *Integration sequence for propagation of the navigation error states of position, velocity and gravitational acceleration.*

Δt, and therefore possible to be valued numerically. This quantity represents approximately the error of neglecting[1] the masses about P in the Innfjorden tunnel.

Final approximation of position error estimate Results from the computations in MATLAB returns the following approximation of the accumulated position error δp_B at Δt. due to the neglected surrounding masses above the reference ellipsoid

$$\delta p_B(\Delta t) \simeq 58\ m \pm 2m$$

The estimate is computed for the net effect of the masses about P of height 32 m above the ellipsoid, located in the middle of the Innfjorden tunnel. The $\pm 2m$ represents the range relative to maximum and minimum heights of P. Compared to the total height above P, equal to 800 m, the $\pm 2m$ is negligible. Assuming the mean height value as representative for the height of P is therefore unproblematic.

6.3.4 TerraPos: Position error

The plot in Figure 6.13 shows the accumulated position error during the GPS signal outages for each of the four runs through the Innfjorden tunnel. The green curves (spikes) represents the measured Down effects, that is those affected by the gravity attraction. It shows clear trends towards some systematic effect related to the accelerometer data, indicating errors in the gravity compensation.

The result for the accumulated position error for the down direction is computed by TerraPos and the plot shows a total of 70 m error. That is right before exiting the tunnel and GNSS signals are reintroduced in the computed trajectory, correcting the position.

[1] By assuming a model utilizing only *free-air* reduction of normal gravity is good enough. This research suggests it is not.

```
C:\Users\ingrij_\Documents\NMBU\Master\PROC\Innfjorden>terrapos --template M001_
20150226.tp_proj\innfjord.tp_subproj\innfjord.tpo --subproject HG9900_fwd --opti
mal-smoother disable
```

Figure 6.11: *Disabling smoother and generating new sub-project in TerraPos from the Windows command line, as this functionality is not available through the TerraPos GUI in Windows.*

Navigation solution with HG9900 Figure 6.13 and 6.14 represent the differences between the reference trajectory and the forward-only navigation solution. The reference trajectory is the smoothed solution, containing the minimum amount of possible errors. The generated differences for navigation solutions subtracted from the reference trajectory are therefore true errors.
The accumulated position error effect for each tunnel passing for the Down component is implied by the plotted green graph.

The resulting solution of true errors when no DEM is applied is given in Figure 6.13. The errors in the Down component are the variable of interest. The largest accumulated position error of the Down component is about 70 m on average, as shown in the plot.

It is previously suggested from the previous result in Part II, that a certain portion of the accumulated error is caused by unmodeled systematic errors. Due to the distribution in topography for the Innfjorden tunnel, mass attractions are a reasonable suspect. Free-air reduction and normal gravity are up to now assumed as a "good enough" approximation. However, in certain applications, this is not adequate in terms of achieved navigation performance. Errors caused by variations in mass distributions of topography represent an external error source.

If including a DEM grid in the processing the unmodeled effect caused by the mass distributions of topography are expected to be compensated. Hence the resulting navigation solution will be improved.

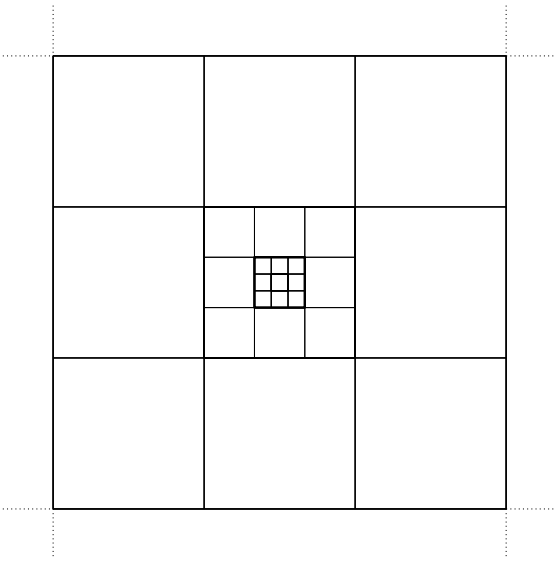

Figure 6.12: *Illustration of Digital Elevation Model (DEM)*

6.4 Digital Elevation Model (DEM)

The DEM consist of a net of squares. The contribution from each square reduces with increased distance from P.

Each cell in the elevation model represent a quantity for the mean terrain height h. The cells are further divided in vertical layers, to represent the topography. The calculations of surrounding mass attraction on a point P assume that every cell quantity can be considered as point masses. Summing up all the contributions from the point masses in all directions corresponds to the three-dimensional gravitational attraction δg.

The forward-only processed solution with applied DEM IS given in Figure 6.14. The true errors in terms of the Down component have shrunk and are by proportion significantly smaller than the error provided for the no DEM grid solution.
By implementing a DEM, the errors are comparable for all NED-components.

Navigation solution with LN-200 The results in Figure 6.15 and 6.16 also show a total of 70 m of accumulated vertical Down position error without the use of the DEM grid. Compared to the results for HG9900 aided solutions in Figure 6.13 and 6.14, the error components in East and North directions are generally larger. This is expected, since the HG9900 is both more precise and accurate, thus providing a higher repeatability and better positioning when unaided. The LN200

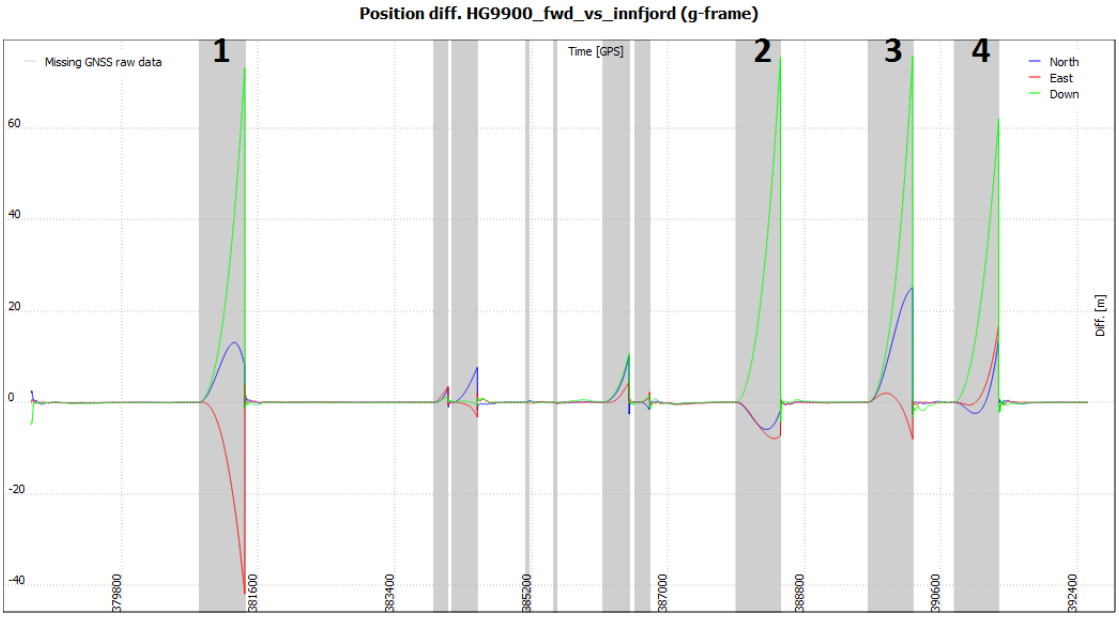

Figure 6.13: *Forward processed solution, for the Innfjorden project. Mounting valid for HG9900. The four runs are marked: 1 – 4.*

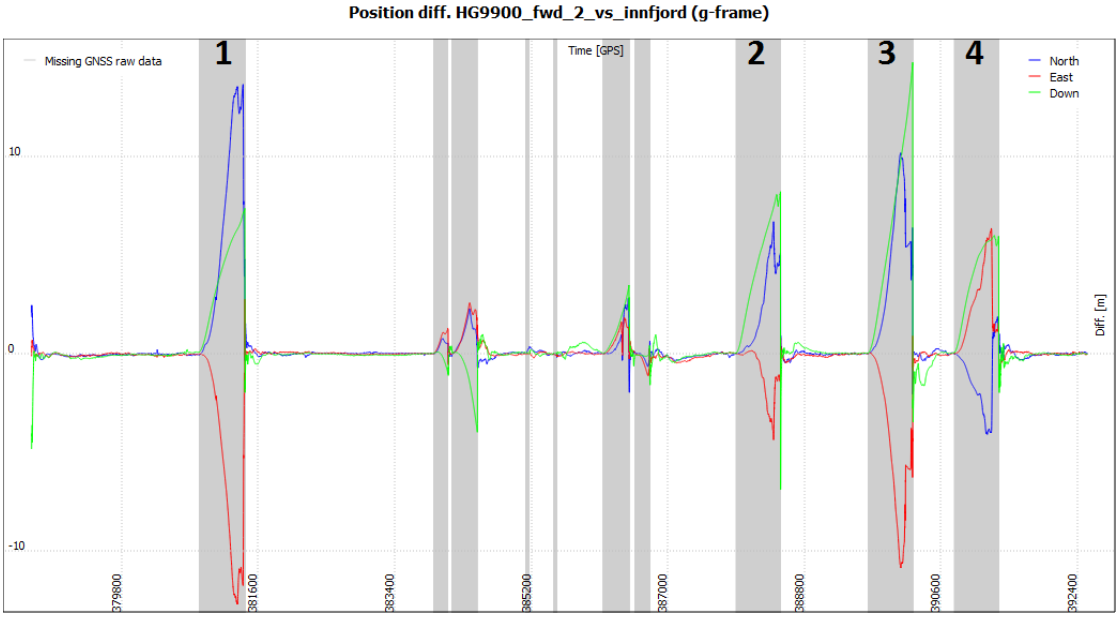

Figure 6.14: *Forward processed solution with applied DEM grid for the Innfjorden project. Mounting valid for HG9900. The four runs are marked: 1 – 4.*

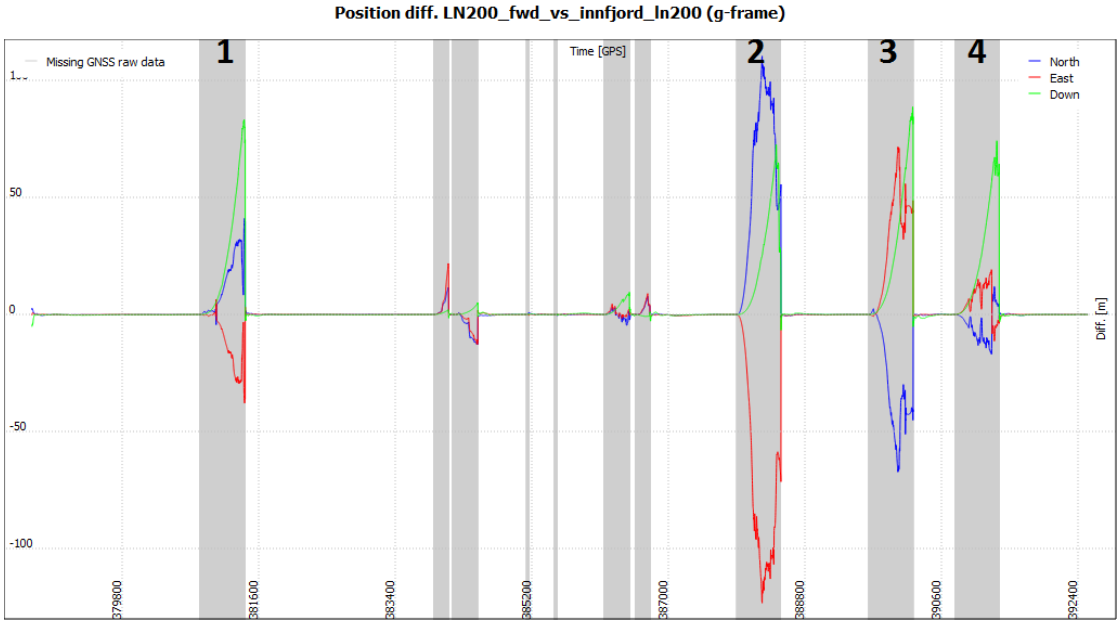

Figure 6.15: *Forward processed solution, for the Innfjorden project. Mounting valid for LN200. The four runs are marked: 1 – 4.*

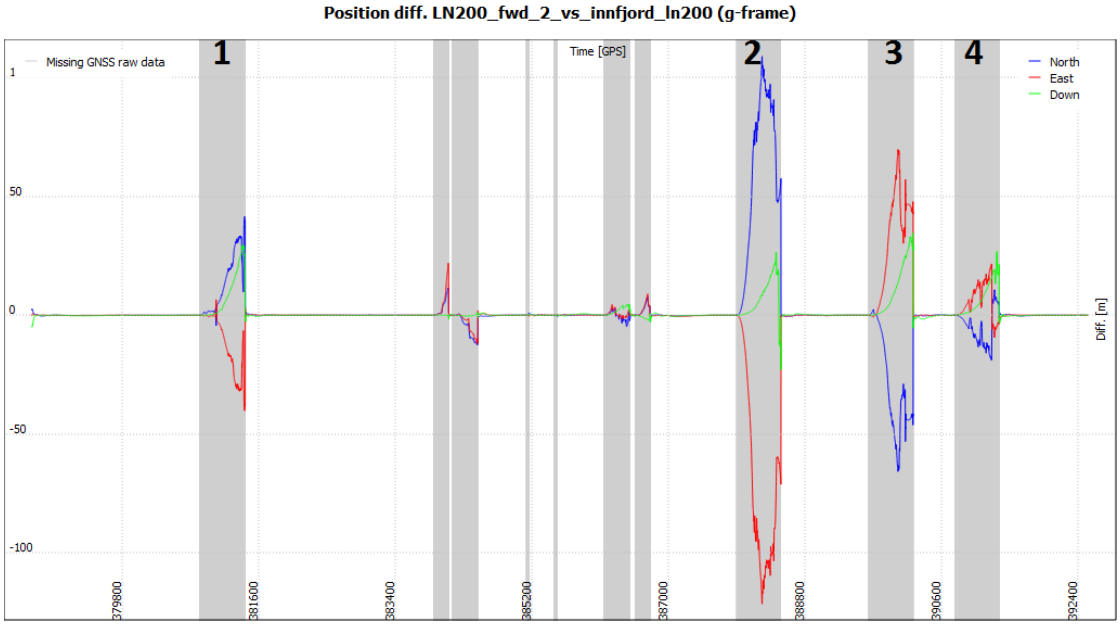

Figure 6.16: *Forward processed solution with applied DEM grid for the Innfjorden project. Mounting for LN200. The four runs are marked: 1 – 4.*

errors are usually reduced by backward-smoothing techniques.

For the processed navigation solution using the LN200 IMU, and including the DEM grid, the vertical error are reduced to about 30 m. The corresponding improvement when utilizing DEM for the HG9900 solution returned an error less than 10 m. Hence the HG9900 solution registered a larger reduction for the error.

Since the HG9900 belongs to a group of higher grade of IMU sensors than the LN200 its output is more precise and less affected by internal errors. Systematic, external errors represents a larger share of the total error observed for the HG9900. The LN200 has larger and less stable biases disturbing the outputs, and of the total error, a larger share of the total errors can not be explained by the systematic error due to the gravitational acceleration of mass distribution, which is the what the DEM grid corrects the data for.

The empirical observation of error in height corresponds to the approximated model results, in both cases.

Plotted position precision standard deviations in forward-only

Figure 6.17 show the position precision standard deviation for a forward-only processed solution, relative to the navigation frame (g-frame). Figure 6.18 show the position precision standard deviation for a forward-only processed solution, relative to the navigation frame (g-frame) when the 100 m grid DEM is applied.

Note that the standard deviation of the Down component is about 20 m in both precision estimates. It adds to the conviction that unmodeled systematic errors are affecting the vertical position. The system however, distribute the blame the errors on other parts of the system.

Plotted Z bias for the Innfjorden tunnel

The plots in Figure 6.19 and 6.11 show the accelerometer bias error of the Z component for the respective non-aided solution with and without applied DEM, for the Innfjorden tunnel.

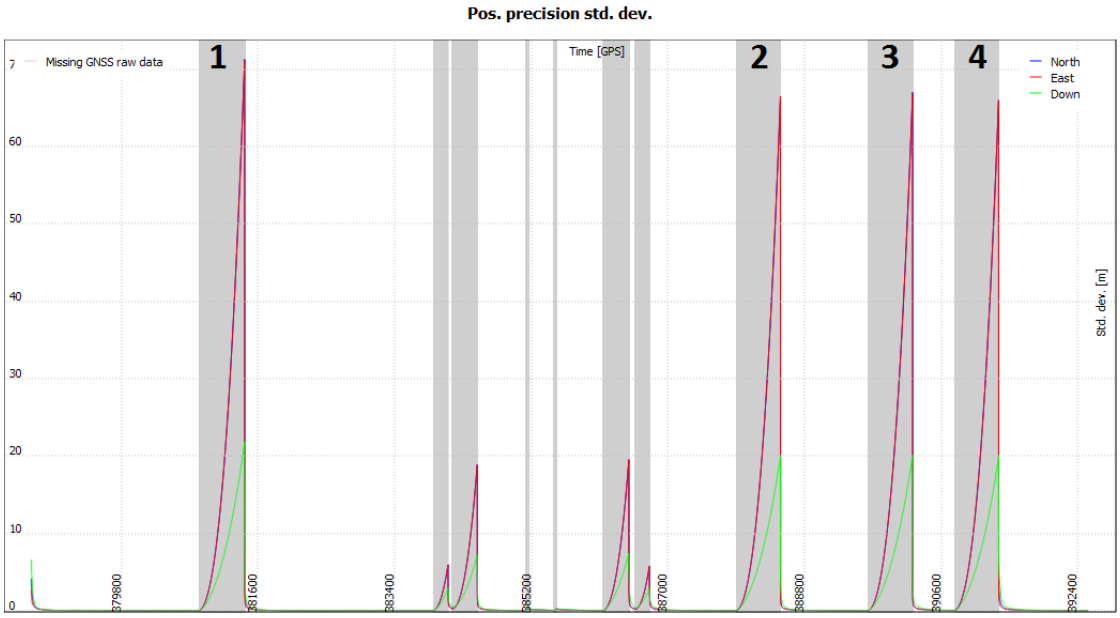

Figure 6.17: *Standard deviation of forward-only solution. HG9900 mounted. The four runs are marked: 1 – 4.*

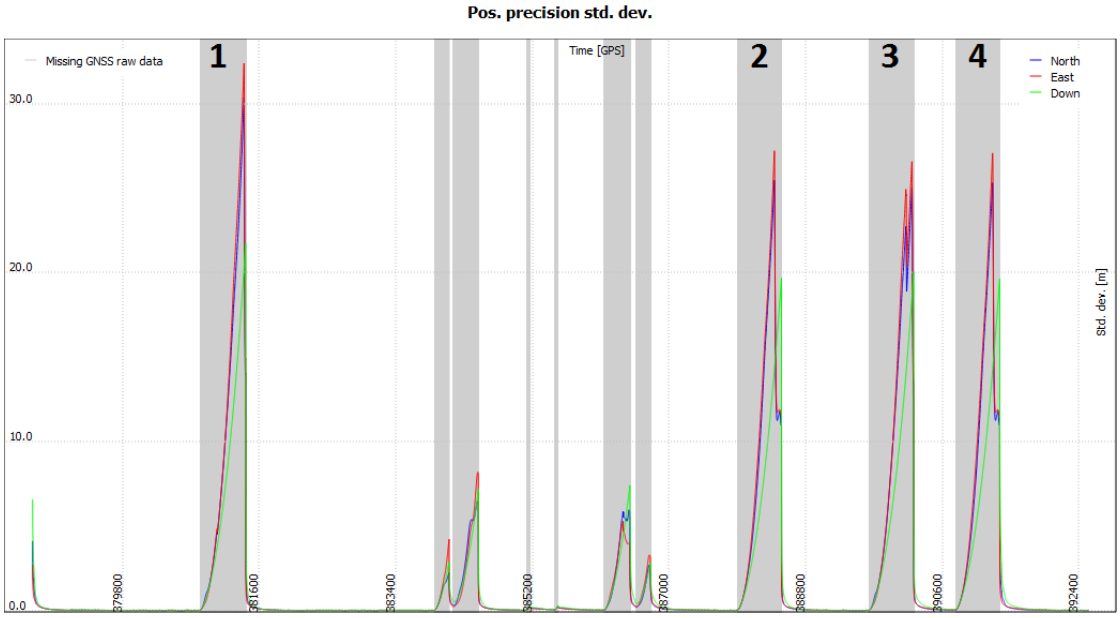

Figure 6.18: *Standard deviation of DEM aided forward-only solution. HG9900 mounted. The four runs are marked: 1 – 4.*

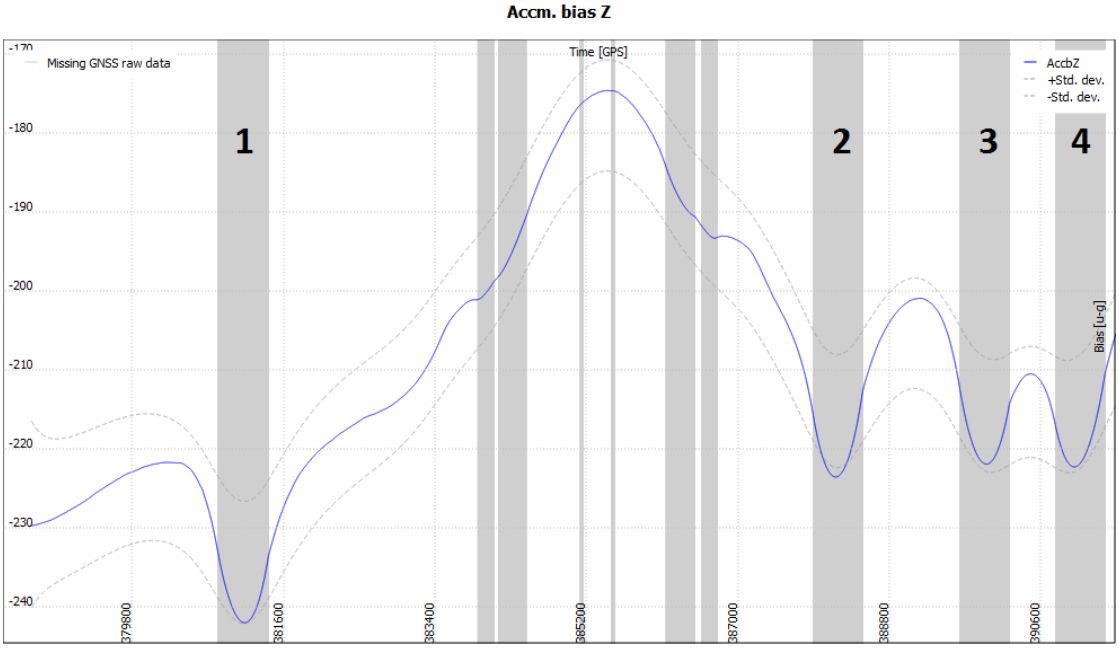

Figure 6.19: *Accelerometer bias Z of trajectory without any external aiding, for the Innfjorden tunnel. The four runs are marked: 1 – 4.*

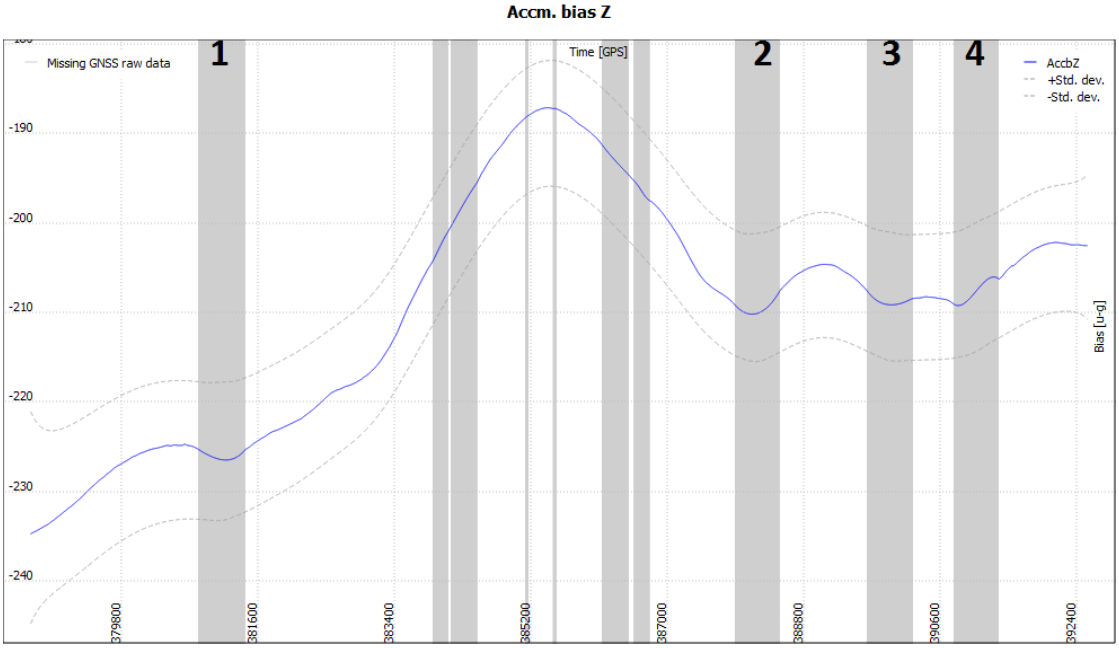

Figure 6.20: *Accelerometer bias Z of trajectory with applied corrections by DEM, for the Innfjorden tunnel. The four runs are marked: 1 – 4.*

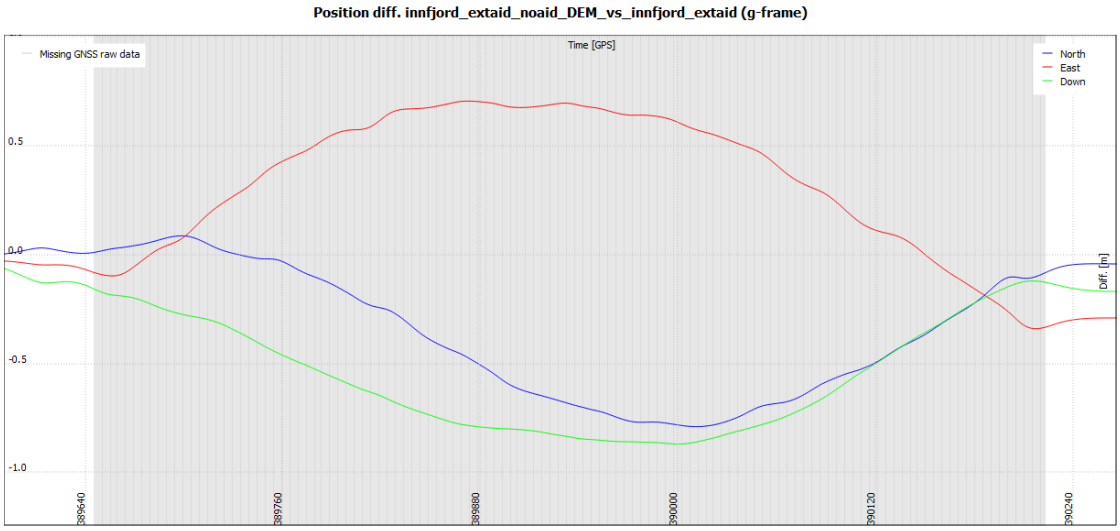

Figure 6.21: *Smoothed DEM implemented position solution for the 3rd run of the Innfjorden tunnel.*

Consideration of true errors of the smoothed solution with DEM implementation

The smoothed solution, hence both forward and backward processing are applied, with DEM is given in Figure 6.21. The result correspond to true errors for the third run, where land-surveyed adjustment points enable an obtained reference trajectory.

The plot of true error in figure 6.21 can be further seen in relation to the plotted true errors in Figure 5.6 for the HG9900 from Part II. In Part II the maximum errors were about 3 m, as compared to the result of sub-meter and decimetre level of errors in 6.21.

6.4.1 TerraPos results for application of DEM to the Lapplia project

The topography encapsulating the Lapplia tunnel is different as compared to the Innfjorden tunnel, when considering the terrain mass distributions. The HG9900 was not mounted on the vehicle for the Lapplia tunnel data sampling. A direct comparison by each IMU sensor dataset is therefore not possible. Only LN-200 IMU data is available.

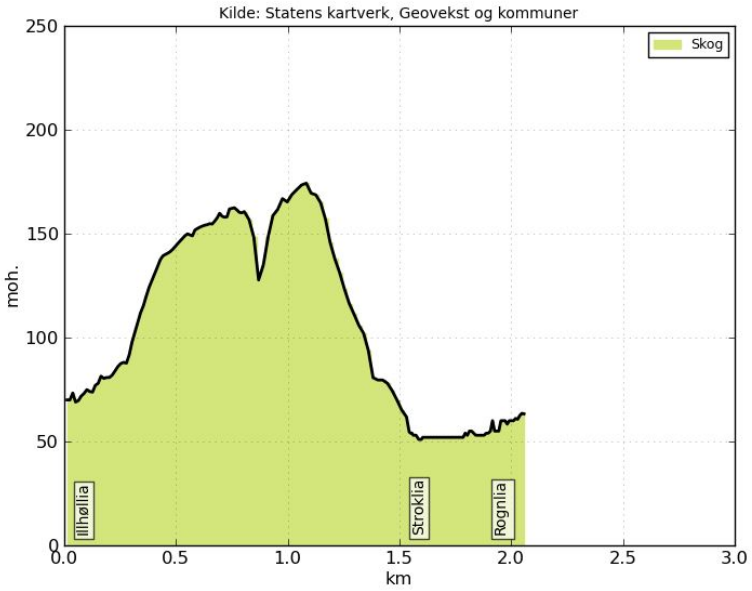

Figure 6.22: *Height profile of the Lapplia tunnel (www.norgeskart.no).*

There is also a significant difference in the length of the tunnel. The Innfjorden tunnel is about six times the length of the Lapplia tunnel. Recall that the time parameter is crucial in terms of error propagation.

The new results from the TerraPos processed Lapplia solution for the research of DEM applied effect are given in Figures 6.23 and Figure 6.24.

Since the tunnel is much shorter in length, the errors have less time to accumulate during the GNSS signal outage. The Innfjorden tunnel are about 6.5 km long as opposed to 1.2 km for the Lapplia tunnel. The same significant results as for the Innfjorden tunnel as not expected for Lapplia.

A grid containing a DEM of the Lapplia area is provided. The resulting effect by including the DEM in the forward-only processed solution is so small that it is hardly visible in Figure 6.24, when compared to Figure 6.23 without applied DEM grid. To depict the differences, the differences between the two solutions with and without DEM applied are generated. The result is presented in Figure 6.25.

Differences between the two solutions are at the centimetre level.

Computation of position error By using the integrative approach derived in previous sections, an estimate of the position error for the masses above an

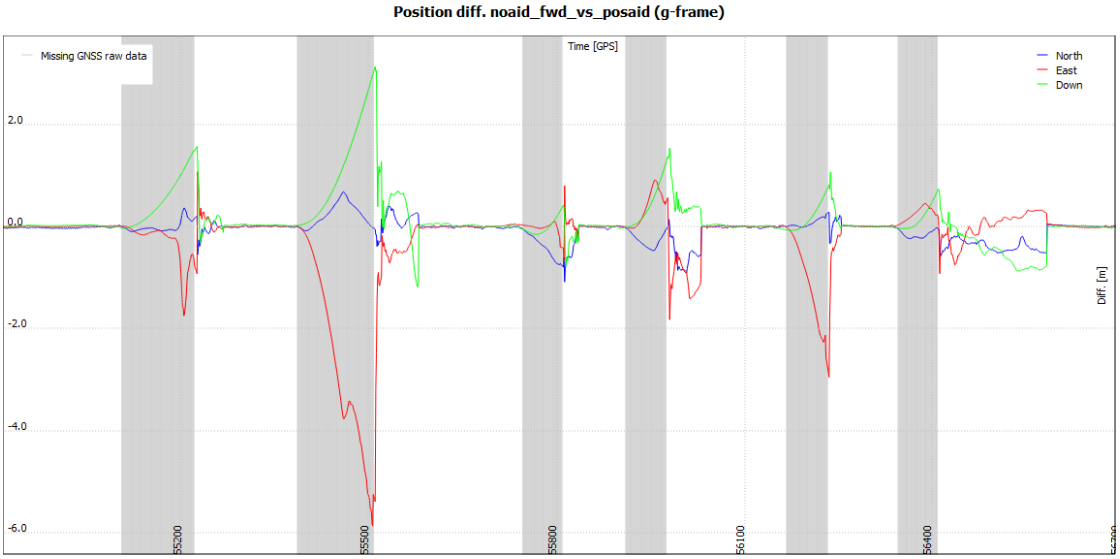

Figure 6.23: *Forward processed solution of the Lapplia project*

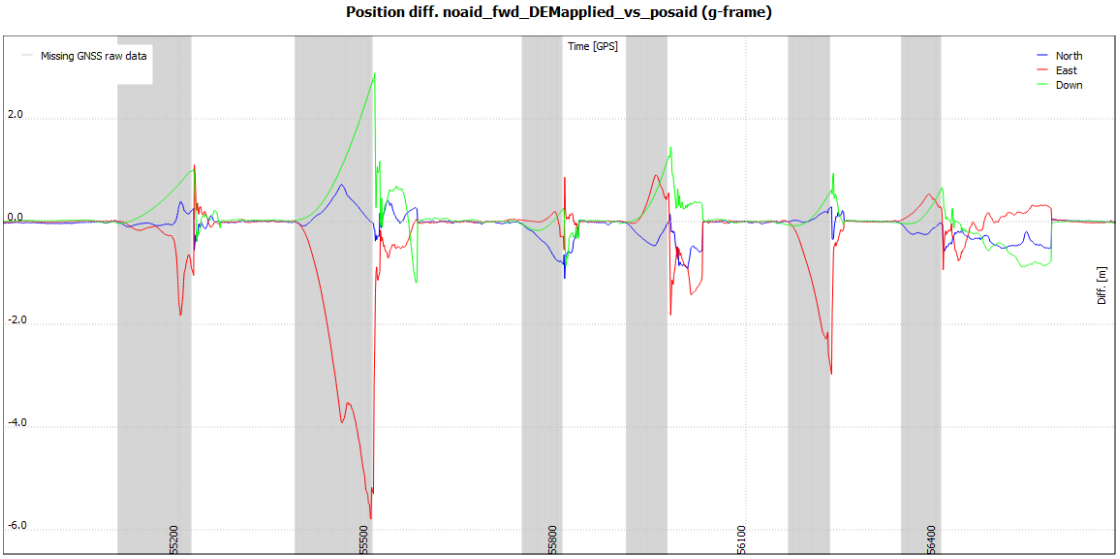

Figure 6.24: *Forward processed solution with applied DEM grid of the Lapplia project*

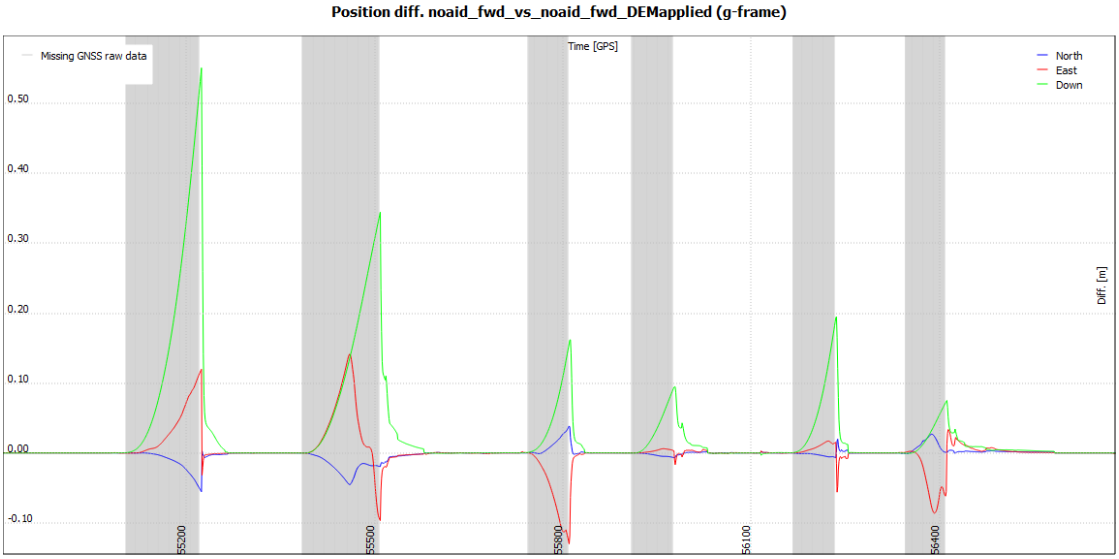

Figure 6.25: *Differences between forward solution with and without DEM grid, for the Lapplia project.*

arbitrary point in the middle of the Lapplia tunnel can be computed. The result can in turn be compared to the TerraPos estimate, to see how well they agree.

Based on the height profile in Figure 6.22, the parameters of the cylinder approximation suggest a radius of 600 meter and height equal to 100 m. For the Lapplia tunnel, as opposed to the Innfjorden tunnel, the masses above and below P are almost equal in terms of vertical height. This is illustrated in Figure 6.26. Only the mass attraction contribution of the top mass is calculated. Computations are performed in MATLAB.

The resulting vertical gravitational acceleration for the respective parameters are $\delta g_B \approx 10.270$ mgal.

The position errors due to the top Bouger mass approximation above P are given as

$$\delta p_B \simeq 0.37 \text{ m for } \Delta t = 120 \text{ s}$$

$$\delta p_B \simeq 0.09 \text{ m for } \Delta t = 60 \text{ s}$$

in terms of the average time duration Δt, by result of the two velocities of 11 m/s and 20 m/s respectively.

The results show minor effects of the masses above the tunnel. This is coherent with the conclusion drawn from the TerraPos computations provided. The

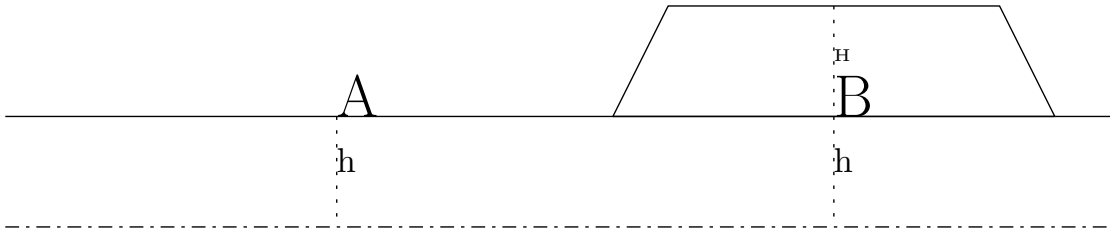

Figure 6.26: *Topographic distribution of masses surrounding position A and B. For A there are only masses below, separated by the height h over the ellipsoid. The ellipsoid is denoted by the lower dashed-dotted line. For B, there are masses both above and below, separated by the terrain height H and ellipsoidal height h.*
For the LN200, the error model compensates the biases for the masses below. Considering the Lapplia tunnel, only the masses above B may result in possible unmodeled systematic effects affecting the further position error.

topographic masses below and above P for the Lapplia tunnel are distributed in larger horizontal extent more than in the vertical extent. The vertical dimension has higher correlation with the gravitational acceleration. Errors are larger in the Innfjorden tunnel for this reason. For Innfjorden, the topography rise abrupt in the vertical dimension, resulting in a larger net error contribution.

The length of Lapplia also has an effect on the accumulation of error. Since the Lapplia tunnel is shorter in length as compared to the Innfjorden tunnel, the position errors have less time to accumulate between the GNSS observation updates.

The higher the velocity, the shorter the GNSS outage. This seems to work well for shorter tunnels, like the Lapplia tunnel.

Plotted Z bias for the Lapplia tunnel

The plots in Figure 6.27 and 6.28 shown below display the accelerometer bias error of the Z component for the respective non-aided solution with and without applied DEM. The non-aided solution only include odometer aiding in addition to the inertial navigation.

The behaviour of the Z component bias is relevant because the gravity acceleration affect the accelerometer observations.
Note that the two IMU sensor are mounted differently in terms of the direction of

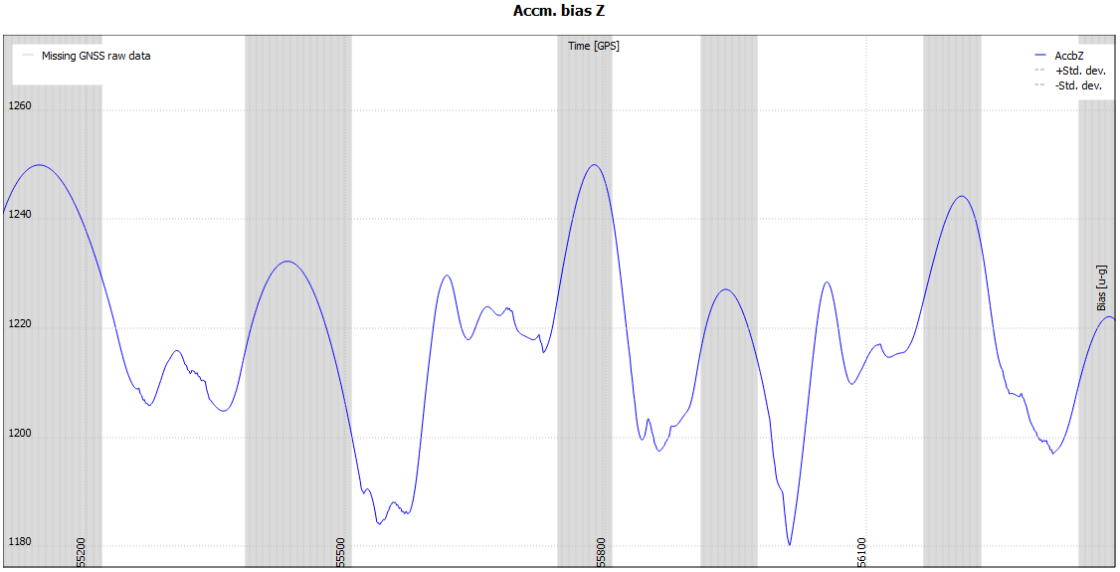

Figure 6.27: *Accelerometer bias Z of trajectory without any external aiding, for the Lapplia tunnel*

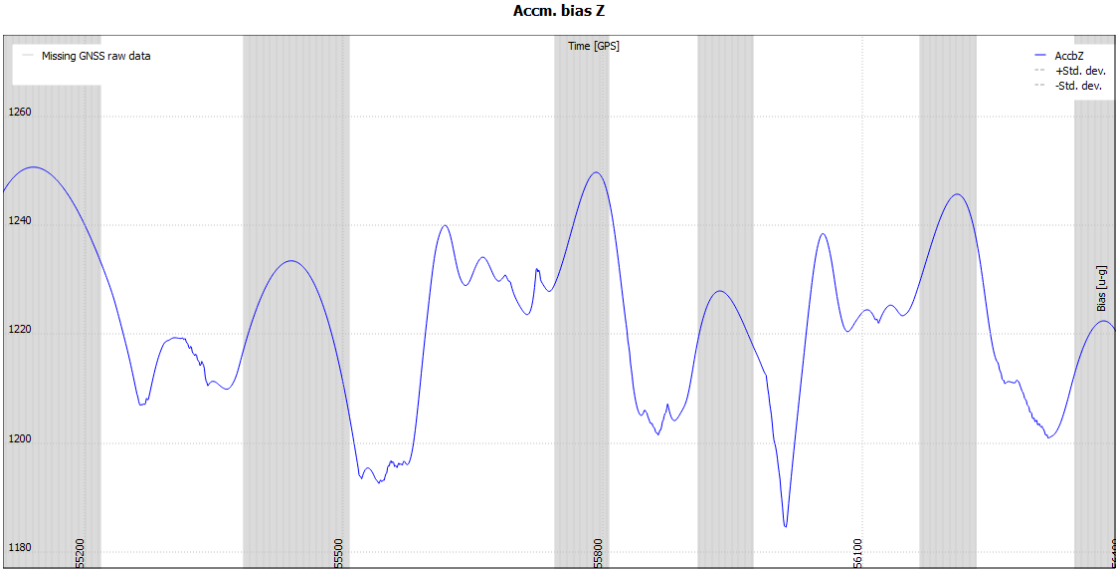

Figure 6.28: *Accelerometer bias Z of trajectory with applied corrections by DEM, for the Lapplia tunnel.*

the Z axis. The LN200 has the Z-axis in the downward direction.

Since no further external aids are applied in the processing in TerraPos, no relative relations are providing further constraints in the direction of the resulting solutions. The respective six runs sampled for the Lapplia tunnel equal the grey field in the plot, where GNSS data are missing. Note that for all GNSS outages, the accelerometer bias plots for Z are headed in the same upward direction.

6.4.2 Summary of Part III

The study of the navigation solutions provided by the higher grade HG9900 IMU concluded that free-air reduction of the normal gravity gradient is not a valid assumption for tunnels with significantly large overlaying topographic masses. Unmodeled terrain correction for these masses result in systematic errors in the navigation solution.

The effect of gravitational acceleration caused by these masses can be seen in the accelerometer bias plot for the Z component. The mounting of the HG9900 IMU defines the Z-axis as positive upwards.

The length of the tunnel, hence affecting the GNSS signal outage, and vertical distribution of masses overhead has the largest impacts on the accumulated error.

Chapter 7

Summary and outlook

An initial summary is first derived herein, to conclude upon the research and obtained results for each of the constituting previous parts I, II and III.

Each section has previously been separately summed up in short, and the aim here is therefore to further draw a red thread through the subsequent parts and emphasize their relation to one another.

A conclusive outlook in terms of further study is included at the end of this chapter.

Conclusive results of part I – III

The initial motivation for this research was to investigate alternatives for external aiding of the navigation solution in tunnels, which represent a GNSS-denied environment. As satellite positioning by GNSS is unavailable, other observations of the navigation states must be considered for the external measurement aiding of the integrated INS.
Among the aiding alternatives of relevance, the use of relative tie points was initially chosen as the object of research.

Results part I In the first research of the Lapplia tunnel, the analyses resulted in a list of practical guide lines. The research questions concerned the investigation of the general effect, amount and density of the RTPs in the tunnel, in addition to what preferred speed of the survey vehicle would yield the best results. As summarized by the guide lines, the study of external aid by RTP observations showed that only a few included features cause a positive effect on the solution. As implied, 10 – 20 tie points might provide a satisfying accuracy of the navigation

solution for some products, when applied to surveying of shorter tunnels like the Lapplia tunnel.
For longer tunnels, i.e. approximately > 2 km by an educated guess, the conclusion herein concerning the significant number of RTPs may not be transferable. The length of the tunnel divided by the number representing the significant amount of RTPs provides the density of features, that is, the uniformly distributed distances between the points throughout the tunnel.

To gain the required accuracy when utilizing the RTP observations, the most important factors turned out to be the speed of the vehicle. Higher speed ensures shorter duration of GNSS outage, due to less time in tunnel. Hence a precise trajectory provided by combined GNSS/INS navigation solution is of great importance. Based on the findings, a constant speed of 20 m/s throughout the tunnel seems sufficient.

The results do not imply that an excessive number of runs, more than the minimum two, is improving the accuracy.

As mentioned in the beginning, the RTPs are important for tying the runs together in a seamless and consistent trajectory. The relative tie points ensure this.
RTP aiding contributes with a relative control between the multiple runs constituting the final trajectory. For survey products that can rely only on the accuracy of the relative positioning inside the tunnel, RTP aid can provide enough information by itself, without the need of land-surveyed adjustment points.

Results part II The second survey included the additional mounting of the HG9900 IMU, and a new survey area was considered. Recall that the topography surrounding the Innfjorden tunnel had a different vertical distribution of mass as opposed to the Lapplia area. The HG9900 was not a part of the mounting in the case of Lapplia, which in turn made it necessary to include both datasets in the thesis' research design. The Innfjorden dataset was analysed in both Part II and III.

A comparison of resulting navigation solutions provided by two different grades of inertial sensors became possible due to the HG9900 IMU. Only one out of the four runs included a reference trajectory, and a performed interpolation of the other three runs was conducted to be able to compare the data. The interpolation enabled a comparison of height errors, as a function of relative distance from one defined end of the tunnel. The resulting plot depicted the accuracy and precision (repeatability) of the navigation solutions, as provided by high and lower grade IMU sensors respectively.

As seen in the plotted results in this part, systematic errors related to the height were detected. The plotted error represent the discrepancies between the navigation solutions and the reference, and was equal to $2 - 3$ meters at the most. The errors was as large for the highly accurate and precise HG9900 IMU, as for the less sophisticated LN200. It was this effect that implied that unmodeled external errors was present in the data.

The errors for the vertical dimension were plotted as relative distance from one end of the tunnel. As the maximum error showed itself located halfway in to the tunnel, the gravitational attraction of the surrounding masses was nominated as a probable cause. This causation was further investigated in the third part.

Results part III As outlined, the last part was dedicated to the systematic effect caused by the large amount of overhanging topographic mass for the Innfjorden tunnel. The theory of Bouger plate and normal gravity was derived and employed for this purpose. By approximating the topography above and below the tunnel passage by Bouger plates of finite extent, a quantified estimate of the net expected effect on the position was found by means of the residual gravitational acceleration.

The processed forward-only filtering solution, conducted in TerraPos, also showed the large deviation in the vertical component. The total accumulated Down-position error reached roughly 70 m at most for the true errors of the forward solution w.r.t. the reference solution. This accumulated error correspond the point at the end of the tunnel.

If seen in the light of the linearised error states, when the other defined biases and errors in the measurement is accurately determined residual gravitational acceleration is observable. The higher level HG9900 IMU detect this relation, as fewer errors disturb its measurements.
This result was confirmed by both processed datasets, each based on a different IMU, i.e. either HG9900 or the LN200. The largest effect correspond to the last discrete defined event of measurement before the vehicle exits the tunnel.

By including a 100 m grid Digital Elevation Model (DEM) of the respective area to the processing routine, the corresponding results returned significantly reduced. The DEM introduce corrections both for the horizontal and vertical gravitational mass attractions. Instead of 70 m, the true errors resulted in about 10 m and 30 m, for the HG9900 and LN200 processed forward-only navigation solutions respectively.
This result is coherent with the plotted position precision in Figure 6.17 and 6.18. The second plot 6.18 show that the errors in height, when compared to the Easting

and Northing components, are significantly more coherent after applying the DEM.

Hence it is fair to conclude that the error introduced by initially assuming a free-air reduction of normal height $\gamma(h, \phi)$ above the ellipsoid is not satisfactory for tunnels similar to Innfjorden. The abrupt rise in terrain masses *above* the survey vehicle at Innfjorden constitutes a significant source of error.

A DEM was further applied to the Lapplia dataset as well, utilizing the same forward-only approach resulting in true errors of the position. As the masses above and below is distributed differently for the Lapplia tunnel, the effect on the vertical component was not as significant. The largest masses in terms of the Lapplia tunnel is located to the East of the tunnel passage, hence is affecting the across-track position in the platform frame.
The research is not necessarily able to conclude for the general case, in terms of the effect of the DEM implementation. However, it shows that a significant effect is possible to obtain.

Conclusion The importance of GNSS observations for initialising and correction of the navigation states, further RTP constraints between defined features, and the implementation of a DEM in processing have been treated in this research.

Outlook and motivation for further research on this topic

Total blockage of satellite signals from GNSS in tunnels ensure the need of external aiding by other sensors or sources.

For the study herein, aiding the navigation solution by observations of RTP in tunnels was considered.
Other sources of position aiding, such as deriving features from stereo-imaging as enabled by photogrammetry, is also relevant for the tunnel application. Several cameras are already mounted on the vehicle, and the data is therefore available. In terms of further research on this topic, enabling implementations of this technique is of relevance.

Bibliography

[Bossler and Toth, 1996] Bossler, J. D. and Toth, C. K. (1996). Feature positioning accuracy in mobile mapping: Results obtained by the gpsvan(tm).

[Cramer, 1997] Cramer, M. (1997). Gps/ins integration. *Photogrammetric Week '97. Wichmann Verlag, Heidelberg, 1997.*

[El-Sheimy, 1996] El-Sheimy, N. (1996). *The Development of VISAT - A Mobile Survey System For GIS Applications.* Ph.d thesis.

[El-Sheimy and Hassan, 2007] El-Sheimy, N. and Hassan, T. (2007). Mobile mapping systems - the new trend in mapping and gis applications. Research report, The University of Calgary. Department of Geomatics Engineering.

[Farrell, 2008] Farrell, J. A. (2008). *Aided Navigation: GPS with High Rate Sensors.* ISBN 978-0-07-149329-1. McGraw Hill Education.

[Gelb, 1974] Gelb, A. e. (1974). *Applied Optimal Estimation.* ISBN 0-262-57048-3 (paper).

[Ghilani, 2010] Ghilani, C. D. (2010). *Adjustment Computations. Spatial Data Analysis. Fifth Edition.* ISBN 978-0-470-46491-5. John Wiley and Sons, Inc.

[Grewal and Andrews, 2001] Grewal, M. S. and Andrews, A. P. (2001). *Kalman Filtering: Theory and Practice Using MATLAB 2nd Edition.* ISBN 0-471-26638-8 (electronic). Wiley.

[Hofmann-Wellenhof and Moritz, 2006] Hofmann-Wellenhof, B. and Moritz, H. (2006). *Physical Geodesy (2nd edition).* ISBN 978-3-211-33544-4. Springer. Wien/New York.

[Hofmann-Wellenhof and Wasle, 2008] Hofmann-Wellenhof, B., L. H. and Wasle, E. (2008). *GNSS - Global Navigation Satellite Systems. GPS. GLONASS, Galileo and more.* ISBN 978-3-211-73012-6. Springer. Wien/New York.

[Jekeli, 2001] Jekeli, C. (2001). *Inertial Navigation Systems with Geodetic Applications*. ISBN 3-11-015903-1. Walter de Gruyter.

[Kjorsvik et al., 2010] Kjorsvik, N. S. et al. (2010). Tigthly coupled precise point positioning and inertial navigation systems. Technical report, TerraTec AS, Norwegian University of Life Sciences, and Norwegian Department of Defence.

[Kjørsvik, 2010] Kjørsvik, N. S. (2010). Introduction to inertial navigation. Technical report, Norwegian University of Life Sciences (NMBU).

[Seeber, 2003] Seeber, G. (2003). *Satellite Geodesy (2nd edition)*. ISBN 3-11-017549-5. Walter de Gruyter. New York.

[Smith and Cheeseman, 1987] Smith, R. C. and Cheeseman, P. (1987). On the representation and estimation of spatial uncertainly. *Int. J. Rob. Res.*, 5(4).

[Terrapos-manual, 2015] Terrapos-manual (2015). Terrapos manual version 2.4-dev. Technical report, TerraTec.

[Thrun and Fox, 2006] Thrun, S., B. W. and Fox, D. (2006). *Probabilistic Robotics*. ISBN 978-0-262-20162-9. The MIT press, Cambridge.

[Titterton and Weston, 2004] Titterton, D. and Weston, J. (2004). *Strapdown Inertial Navigation Technology, 2nd Edition*. ISBN 0-86341-358-7. IEE.

[Torge and Müller, 2012] Torge, W. and Müller, J. (2012). *Geodesy (4th edition)*. ISBN 978-3-11-020718-7. Walter de Gruyter. Berlin/Boston.

[Woodman, 2007] Woodman, O. J. (2007). An introduction to inertial navigation. Technical report, University of Cambridge.

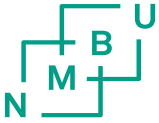

Norwegian University
of Life Sciences

Postboks 5003
NO-1432 Ås, Norway
+47 67 23 00 00
www.nmbu.no